MICROFLUIDIC TECHNIQUES FOR LYSING, PURIFICATION AND

BEAD-BASED DETECTION OF RNA FROM COMPLEX SAMPLES

A DISSERTATION

SUBMITTED TO THE DEPARTMENT

OF MECHANICAL ENGINEERING

AND THE COMMITTEE OF GRADUATE STUDIES

OF STANFORD UNIVERSITY

IN PARTIAL FULFILMENT OF THE REQUIREMENTS

FOR THE DEGREE OF

DOCTOR OF PHILOSOPHY

Anita Rogacs

September 2013

This dissertation is online at: http://purl.stanford.edu/wk525zg0251

I certify that I have read this dissertation and that, in my opinion, it is fully adequate in scope and quality as a dissertation for the degree of Doctor of Philosophy.

Juan Santiago, Primary Adviser

I certify that I have read this dissertation and that, in my opinion, it is fully adequate in scope and quality as a dissertation for the degree of Doctor of Philosophy.

Kenneth Goodson

I certify that I have read this dissertation and that, in my opinion, it is fully adequate in scope and quality as a dissertation for the degree of Doctor of Philosophy.

Thomas Kenny

Approved for the Stanford University Committee on Graduate Studies.

Patricia J. Gumport, Vice Provost for Graduate Education

This signature page was generated electronically upon submission of this dissertation in electronic format. An original signed hard copy of the signature page is on file in University Archives.

IV

Abstract

This dissertation describes three techniques aimed at automated, sensitive sample preparation and detection of RNA from complex samples. Microfluidic systems have advanced the state of the art for a wide number of chemical and biological assays, but robust and efficient sample preparation remains a major challenge. One of the most difficult processes is the lysing, purification, and detection of target RNA from whole blood samples. This dissertation addresses key challenges in each of these RNA workflow phases.

In the first part of the dissertation, we demonstrate a novel assay for lysing followed by physicochemical extraction and isotachophoresis-based purification of 16S ribosomal RNA from whole human blood infected with *Pseudomonas Putida*. This assay is unique in that the extraction can be automated on-chip using isotachophoresis in a simple device with no moving parts, it protects RNA from degradation when isolating from ribonuclease-rich matrices (like blood), and produces a purified total nucleic acid (NA) sample which is compatible with enzymatic amplification assays. We show that the purified RNA are compatible with reverse transcription-quantitative polymerase chain reaction (RT-qPCR), and demonstrate a clinically relevant sensitivity of 0.03 bacteria per nanoliter using RT-qPCR.

In the second part of the dissertation, we present a model to aid in design and optimization of a wide range of electrophoresis (including isotachophoresis) assays. Our model captures the important contributors to the effects of temperature on the observable electrophoretic mobilities of small ions, and on solution ionic strength, conductivity and

pH; the most relevant parameters in molecular reactions and separation assays. Our temperature model includes relations for temperature-dependent viscosity, ionic strength corrections, degree of ionization (pK), and ion solvation effects on mobility. We incorporate thermophysical data for water viscosity; temperature-dependence of the Onsager-Fuoss model for finite ionic strength effects on mobility; temperature-dependence of the extended Debye-Huckel theory for correction of ionic activity; the Clarke-Glew approach and tabulated thermodynamic quantities of ionization reaction for acid dissociation constants as a function of temperature; and species-specific, empirically evaluated correction terms for temperature-dependence of Stokes' radii. We incorporated our model into a MATLAB-based simulation tool we named Simulation of Temperature Effects on ElectroPhoresis (STEEP). We validated our model using conductance and pH measurements across a temperature variation of 25°C to 70°C for a set of electrolytes routinely used in electrophoresis. The model accurately captures electrolyte solution pH and conductivity, including important effects not captured by simple Walden type relations.

In the third and final part of the dissertation, we introduce a cost-effective and simple-to-implement method for direct detection of RNA, by analyzing images of randomly distributed multicolor fluorescent beads bound by the target molecule. We term our method particle imaging, tracking and collocation (PITC). We use a fairly standard epifluorescence microscopy setup fitted with an off-the-shelf dual view color separator attachment which images fluorescence emission at two wavelengths onto two respective halves of a single CCD image array. We perform automated analysis of these two color channels to track thousands of particle images in either or both wavelengths, and we track

particle image motion in time and space. We can quantify particle image wavelength (or wavelength ratio), absolute intensities, and particle image diameter. We also perform cross-correlation image analyses on this multi-wavelength data to track particle collocations and the degree of correlation of particle motion. Particles or cells can be suspended in solution and flowed through a wide variety of microchannels (with optical access for image collection). Particles can be transported through the detection region via electrophoresis and/or pressure driven flow, to increase throughput of analysis. We here introduce and evaluate the performance of our method. We use Monte Carlo simulations to demonstrate robustness of the algorithm and optimize algorithm parameters. We present an experimental demonstration of the method on challenging image data, including flow of randomly distributed Brownian particles and particle populations which undergo particle-to-particle binding. We show results of bead collocation measurements on bead-to-bead binding created by the *E.coli* 16S rRNA gene.

Acknowledgments

I was only 18 when I first walked the grounds of The Farm, dreaming of a life at this prestigious University. It was only a month after I moved here from Hungary, leaving my family and friends behind. I sat on the fields of the Oval on Palm Drive, thinking how ridiculous this dream was, and that I should consider myself lucky to even talk to someone attending here. Many years have passed since that day, and I find myself wondering, how I got here. Frankly, it does not take much effort to find the answer to this question: I had a dream and I surrounded myself with the people I admired the most. Dreaming for a better, successful and rewarding life is easy. That was my part. But the rest of this story is about the amazing people I met during this journey. I am humbled by the number of individuals who have blessed me with their time, their patience, and their knowledge.

First, I would like to thank my research advisor, Professor Juan Santiago, for supervising my doctoral research and for guiding me through the natural ups and downs of scientific research. Juan is a brilliant researcher with an infectious passion for science and teaching. He motives by example, sets high expectations (definitely higher than what you think you can achieve), and gives sometimes harsh, but always honest feedback on progress and results. (I have heard others refer to this as "extreme professional honesty.") I find his professional honesty one of the most refreshing and effective aspects in his advising methods. The greatness in his approach lies in his transparent motivation: Above all he wants you to succeed. He takes his role as your mentor and adviser personally. While his passion is science, his mission is preparing you for a life in research. Thanks to his great efforts and care, I have grown infinitely more capable and confident in my

work, to a point where I dare to dream bigger and better. I am incredibly fortunate to call him my mentor and adviser.

I am also very grateful for Professor Kenneth Goodson, who was my research adviser during the first three years of graduate school. The first year at Stanford can be scary, overwhelming and hectic. My meetings with Ken were always constructive and productive, as he rose above the noise of my frantic concerns and advised me to prioritize and focus my attention on the issues with greatest impact and importance. He is a man of few, but carefully selected words. I always admired his professional and personal wisdom and calm demeanor. He has given me much invaluable personal and professional career advice for which I have benefited greatly. I would also like to thank Professor Thomas Kenny for his advice, guidance and support on my dissertation and for his genuine curiously and interest in my work and career plans. I regard the opportunities I had for interaction with Prof. Kenny as an absolute privilege.

I want to thank my undergraduate research adviser, Prof. Jinny Rhee, who has taken me under her wings, introduced me to the word of research, helped me write my first conference paper and continued to cheer me on during this journey. Jinny, you have been a wonderful mentor and a great friend. I am also incredibly thankful for the support and guidance I received from the team at HP Labs: Chandrakant Patel, Amip Shah, and Cullen Bash. I especially thank Amip for the many lunch meetings, thought-provoking discussions, and his unwavering support and mentorship.

I thank all my lab mates in both the Santiago and the Goodson labs. I greatly appreciate the immense knowledge (professional and personal) I gained from interacting with Jeremy, Shilpi, Lewis, Julie, Joe, Milnes, Amy, Moran, Supreet, Giancarlo, and

Yatian. I thank you and the rest of the group(s) for everything you taught me, for your willingness to share ideas, and for always being supportive and encouraging. I especially thank Lewis Marshall and Julie Steinbrenner, who spent many hours building experiments, taking data, and debating problems and solutions with me. But what I cherished the most was the time we spent together burning off stress by either running or rock climbing. You guys rock (pun intended)! I admire you both for your wits, humor and positive attitude. I am lucky to have found such great friends in lab.

I also want to give special thanks to our administrators, Cecilia Gichane-Belle and Linda Huber, for their unwavering support. Without you, we simply could not function.

Finally, I want to say that I could not have done any of this without my family. I am eternally grateful to my parents who have instilled in me the great value of hard work, and the deep sense of accomplishment it offers. I am also very grateful for my family here, Jeremy, Jane and John, for supporting me at every step of this long journey. I am blessed to have a loving husband who understands me, who makes me laugh, and who inspires me to be a better person every day. Jeremy has seen me at my best and at my worst and has kept me anchored in reality throughout. I am so thankful to have him in my life. Lastly, I want to give huge thanks to my closest friends who reminded every day that life outside the lab is fun, exciting and beautiful. Jeremy, Zoli, Ildiko, Yasmin, Shilpi, and Ashley: thanks for keeping me balanced all these years. You are the family I chose.

x

Table of Contents

List of Tables

List of Figures

Figure 4.3. PITC algorithm structure. Each image sequence contains data for thousands of unique particles. After registration of the two images, the algorithm proceeds in two main phases. The first phase quantifies local drift particle velocities using micron resolution particle image velocimetry (micro-PIV). Unique particle images in Channel 1 (Ch1) are then identified, located and characterized via the particle mask correlation and particle characterization (PMC-PC) method. The particle image intensity and radius are evaluated using a non-linear Gaussian fitting routine. The algorithm then combines results of PMC-PC and micro-PIV for a particle tracking velocimetry (PTV) subroutine enhanced by Kalman filter and χ^2-testing method (KC-PTV). This analysis results in accurate determination and tracking of the location of each particle over time and space. The second phase of the algorithm cross-correlates subregions surrounding the particle locations identified in Ch1 with corresponding subregions in the registered Ch2. Ch2 particle characteristics, such as radius and total fluorescence, are evaluated using the Gaussian fitting subroutine.

1 Introduction

1.1 Why target Ribonucleic acid (RNA)

RNA transcripts within a cell can be broadly classified as ribosomal RNA (rRNA), transfer RNA (tRNA), messenger RNA (mRNA), and small RNAs.[1] rRNA is the most abundant RNA component in the cell. The abundance of rRNA allows it to be exploited as a control signal for total RNA mass, as a set of molecular weight markers for electrophoresis, and as a biomarker for detection of bacterial infection.[2, 3] Transfer RNA is responsible for transporting amino acids to the ribosome to support protein synthesis and is a target of genetic and metabolic research.[4] Messenger RNA is the most diverse of all RNA transcripts and it is the central driver of cell phenotype. The abundance levels of an individual mRNA sequence might range from a single copy to thousands of copies per cell.[5] The expression levels of low to moderate abundance mRNA can provide information on the clinical status and outcome of cancer[6] and/or the effectiveness of applied treatment.[7] Housekeeping genes typically make up the set of high abundance mRNAs and are often used to normalize gene expression levels of other relevant mRNAs.[8] Finally, micro-RNAs (miRNAs) are subset of transcripts, which only recently gained significant attention. They serve essential and diverse physiological functions such as differentiation and development, proliferation, and maintaining cell type phenotypes; and will likely serve as the basis for novel therapies and diagnostic tools in the future.[9] The menagerie of RNA species and their functions is still expanding, and it is becoming clear that RNA species can play roles in post-transcription RNA modification, DNA modification, telomerase extension, and a range of other functions.

1.2 Workflow of RNA analysis

Figure 1.1 illustrates a typical process flow for RNA analysis, which includes steps such as RNA extraction, purification, quantitation, reaction and detection. The choice for the method of RNA extraction or lysis is primary governed by the subpolulation of RNA (e.g.: tRNA, mRNA, rRNA) that is of interest, the biological source of RNA (e.g.: bacteria, virus, fungi, host mammalian cell), and of the sample matrix (e.g.: urine, saliva and blood). Due to the enormous complexity of the extraction process, such protocols are often empirically derived and optimized. Many efficient methodologies which accommodate the expedient isolation of RNA have already been developed[1] and can be categorized into chemical, thermal, mechanical and electrical based methods. After extraction, the RNA is ideally purified from interfering compounds. The most common methods include liquid phase and solid phase extractions (See Section 1.3.2 for detailed discussion). The purified RNA quantity and quality is subsequently analyzed via electrophoretic separations (for example, the Bioanalyzer[10, 11]). While the presence of unique RNA sequence can be directly detected with various transduction methods, its instable nature,[12-14] or requirement for sequence amplification, often necessitates its conversion to its complimentary DNA (cDNA) sequence via reverse-transcription (RT). The conversion of RNA to DNA is accomplished by an enzyme, called reverse transcriptase, and the process takes approximately 45 min at elevated temperature. This process is then followed by either polymerase chain reaction (PCR) for sequence-specific DNA amplification, and/or DNA sequencing or hybridization to solid support, such as complimentary probe functionalized microarrays and beads. The solid supports enable highly multiplexed platforms for sequence identification. For example,

2

microarrays rely on a single color fluorescent labeling of the target nucleic acid, and achieve multiplexing by spatial localization of sequence identity (each spot on a glass slide is functionalized with probes that are complimentary to different target sequences).[15] In contrast, bead based assays achieve multiplexing via differential internal labeling of beads. As an example, Luminex Inc. offers bead populations with two fluorescent dyes infused at unique ratios.[16] Detection of the ratio of these two dyes gives identity to the bead, and subsequently to the probe sequences that are attached to the beads. DNA probe functionalized beads are incubated with targets which are labeled with a fluorescent molecule that emit at a wavelength different from those used for bead identification.

Fluorescence based detection of RNA/DNA can be based on (1) volumetric fluorescence integration of the reaction solution where color is related to sequence identity (e.g., PCR reactions), (2) imaging of spatially resolved fluorescent spots, where location is correlated to sequence identity (e.g: microarray), and (3) time-resolved measurements of florescence associated with flow-through beads, where emitted bead color gives sequence identity, and the target label indicated its presence on the bead.

| Extraction *(Lysis)* | Separation *(Purification and/or quantitation)* | Reaction *(Enzymatic- and/or hybridization-based)* | Detection *(Fluorescence-based)* |

RNA source:
bacteria, virus, fungi

Sample matrix:
urine, saliva, blood

Target:
rRNA, mRNA, miRNA

Method:
chemical, thermal, mechanical, electrical

Liquid phase

aqueous phase: RNA
interphase: DNA
organic phase: proteins, lipids

openwetware.org

Solid phase

imgm.com

Bioanalyzer

[FU]
15
10
5
0
25 200 1000 4000 [nt]

Reverse transcription
Single-stranded cDNA
mRNA

studyblue.com

Hybridization
e.g.: microarray

cs.wustl.edu/~jbuhler

Hybridization e.g.: bead-RNA

asurgen.com

Volumetric

medscape.com

Spatially-resolved

igece.org

Time-resolved

40%

PE

5% 52%

FITC

springerimages.com

THESIS CONTRIBUTIONS

EXTRACTION	SEPARATION	REACTION	DETECTION
Bacterial RNA Extraction and Purification from Whole Human Blood Using Isotachophoresis			
	Temperature effect on electrolyte properties (pH, ionic strength) and electrophoretic separation performance		
		Tracking and multispectral colocation method for cytometry-like and bead binding assays	

Figure 1.1 (Top) Traditional RNA workflow and example techniques. The workflow typically involves four phases: extraction, separation (involving purification and quantitation), reaction and detection. We here show representative example methods for each of the phases. (Bottom) Schematic of thesis contributions in the corresponding RNA workflow phases are listed in grey blocks. The details of these contributions are described in Chapter 2, 3 and 4, respectively.

Currently, the promise of NA-based diagnostics has been hampered by the requirement for trained laboratory technicians or prohibitively complex or expensive robotics to carry out these complex, multi-step assays. After collection, samples are sent to centralized laboratories for processing, where they undergo extensive preparatory steps (e.g. centrifugation, DNA/RNA extraction, multiple pipetting) before being assayed for

4

select pathogens or physiological condition. There is thus an urgent need for widely-proliferated, unbiased, multiplexed platforms able to perform all sample extraction, purification, and detection in a highly-automated yet robust fashion. The throughput, recovery efficiency, reagent volume, flow rate, and various protocol parameters of sample preparation and reaction should be compatible with the downstream molecular analysis. These method need to be fast, cost-effective, and have high throughput capabilities.[17] Also important are methods that can be easily automated and integrated into an analytical module.

This dissertation describes our work towards designing a robust and novel system with no moving parts, for highly-automated, sample preparation and multiplexed detection of bacterial RNA from infected whole human blood. We addressed critical needs in each of the RNA workflow phases, as shown in bottom schematic of **Figure 1.1**. First, we have designed a protocol and microfluidic device which uses isotachophoresis (ITP), an electrokinetic method for sample concentration and separation, to perform, rapid, automated RNA extraction, which avoids degradation of (extremely labile) RNA and requires minimal or no user intervention. Next, we developed a novel electrophoresis model which includes formulations for temperature effects on electrolyte properties that are relevant for molecular reactions and separations. And finally, we introduce a novel, cost-effective, and simple-to-implement RNA detection method. Our custom particle tracking and collocation algorithm analyzes images of randomly distributed fluorescent beads flowing through a fluidic channel. The presence of RNA is correlated to the detection of spectral collocation of two fluorescent beads bound to the RNA (or DNA) target.

In this introductory section, we first review sample matrix effects and traditional extraction and purification methods. We then highlight the importance of temperature in electrophoretic separations and reactions. In the final section, we review the most common methods for RNA detection.

1.3 Sample preparation

1.3.1 Sample Matrix Interference

Urine, saliva, and blood are among the most common types of biological matrices used for nucleic acid analysis. Whole blood is perhaps the most important sample matrix for clinical analysis, as it is collected routinely and contains information about the entire body.[18] While the composition of whole blood can be very stable, its complexity presents significant challenges as the matrix components interfere with sample preparation methods, and can effect signal response of many bioanalytical assays.[19, 20] These components include cell debris, serum proteins, endogenous phospholipids, iron ions, and anticoagulants.[21] The high and variable viscosity of blood can also affect binding efficiency and specificity. Therefore, most sample preparation techniques require that blood components be separated by centrifugation or filtration, two techniques which are notoriously difficult to implement in an automated format.

1.3.2 Traditional purification methods

NA preconcentration and purification from a complex biological matrix are required preparation steps for PCR,[22] capillary electrophoresis,[22] microarray hybridization,[23] and many other analytical techniques used in biology and medicine. Sample preparation "is the most error-prone and labor-intensive task in the analytical laboratory".[24]   Because of

6

its impact on nearly all subsequent steps, methods involving large numbers of manual sample manipulations are highly risky as they may result in NA degradation or sample loss or cross-contamination, particularly when several samples are processed simultaneously. Thus the success of fully automated, benchtop analytical device is inherently dependent on the successful miniaturization and seamless integration of sample preparation with downstream processing including aliquoting, parallelization, and analysis mechanisms.[25]

A very common method of RNA preparation is phenol/chloroform extraction followed by an ethanol precipitation originally devised by Chomczynski and Sacchi in 1987.[26] While this purification protocol produces high purity NA at high and repeatable recovery efficiency, it is a time- and labor-intensive process, involving a complex series of precipitation and washing steps, centrifuging steps, and requiring relatively large quantities of toxic organic solvents disposal of which is expensive. Despite this, such techniques are often the norm in biology and repeated frequently. The aforementioned Chomczynski reference alone has been cited over 59,800 times (as of August 2013).

The manual labor and reagent use of RNA purification is greatly reduced by adapting solid-phase extraction (SPE) on silica or ion exchange resins.[27] The SPE extraction protocol leverages the use of low pH, high ionic strength chaotropic lysing agents. NAs in such media has high affinity for silica-like surfaces to which they adsorb. Commercial spin columns such as the QIAGEN kits (Valencia, CA) are now the standard methods for purification of RNAs.[28] Magnetic separation avoids the need for centrifugation, but still requires trained technicians to manipulate reagents.[29]

Many of these nucleic acid sample preparation techniques have been developed into commercial products and purifications now often take less than 1 h to perform. However, most methods remain labor intensive; and typically involve multiple steps of mixing, centrifugation, separation, and buffer exchange—all of which are difficult to automate and miniaturize. Automation has been limited mostly to using robotic machinery to mimic the actions of human hands. These actions include sample dispensing, loading and unloading (e.g., onto a centrifuge), and buffer and reagent loading and washing steps. One example of this is Qiagen's Qiacube[30] which automates many of the processing steps of sample preparation; but which uses fairly standard spin-column kits which have roughly the same figures of merit (e.g., yield, processable sample volume) as their manual counterparts.

The last decade has also seen an impressive number of advancements in micron- and millimeter scale fluidic systems which aim to miniaturize and automate some sample preparation methods. This work has consisted mainly of miniaturizing SPE methods both DNA and RNA extractions.[28, 31, 32] Despite these advances and demonstrated devices, the miniaturization of sample preparation into small scale fluidic systems still poses a major challenge. Mariella[25] calls this the "weak link in microfluidics-based detection". Most of these limitations include dealing with the presence of PCR inhibiting chemistry (GITC, GuHCL, isopropanol, ethanol), the use of toxic chemicals, the requirement for special surface chemistries, the requirement for complex fluidic pumping and valving (to replace robotic or manual pipetting steps), and the reduced binding capacity due to competitive protein absorptions to silica or bead surfaces. For example, a recent review on sample matrix effects on automation[21] concluded that SPE based methods lack the potential to

8

deal with the complexity of whole blood and recommended that more effort should be expended on developing electrokinetic methods for matrix management. In our review of current microfluidic SPE technology, we found that most micro-SPE based methods still cannot efficiently process complex sample matrices, such as whole blood.

To date, studies reporting RNA purification using microfluidic platforms,[6, 33-39] are scarce. There is still a significant need for microfluidic approaches which have adequate RNase control, can enable direct integration of lysis, nucleic acid purification (particularly RNA) from complex samples, and provide compatibility with hybridization and enzymatic reaction-based detection methods. We here describe a new and emerging alternative to traditional sample preparation of RNA from complex biological samples using ITP as the central method of extraction, purification, and buffer exchange. The application of ITP to sample preparation is a fairly clear departure from traditional methods of dealing with NAs as it does not require specific surface materials, specific surface chemistries, specific solubility of one species versus another, specialized geometries, or pumping or valving of reagents. Instead, ITP leverages the high ionic electrophoretic mobility of NA relative to known impurities and downstream assay inhibitions to extraction, preconcentrate, purify, and deliver DNA and/or RNA to a downstream location or step in a protocol.[40] ITP uses an electric field to extract and pre-concentrate only target analytes whose electrophoretic mobility is in a specific range established by two buffers.[41] Specifically, extracts and focuses NA whose mobility is between the anion of low mobility trailing electrolyte (TE) and the anion of a high mobility leading electrolytes (LE).[42, 43]

1.4 Temperature effects on RNA reactions and separations

1.4.1 Enzyme-based reactions, hybridization stringency and reaction rates

Enzyme-based RNA manipulation, such as digestion, reverse-transcription, and amplification are especially sensitive to conditions such as temperature, pH and ionic strength. Typically, as the operating temperature is raised, the rate of enzyme-catalyzed reactions increase to a maximum. With respect to this optimum condition, variations in reaction temperature as small as 1 or 2 degrees may introduce changes of 10 to 20% in enzyme activity.[44] Further increases in temperature decreases activity, and can eventually result in irreversible enzyme inactivation and even denaturation. The optimum temperature for maximum activity varies substantially between enzymes, even within those that share the same template and functionality. For instance, reverse-transcriptase, is an enzyme used to generate complementary DNA (cDNA) from an RNA template, a process termed reverse transcription. Its optimum activity is at pH ~ 7, and at temperature of 37-65 °C, depending on the type of RT.[45]

Temperature also has a strong influence on hybridization stringency. For example, PCR, microarray and bead assay probe design typically involves equilibrium-based considerations, which are aimed at maximizing the difference in melting temperatures, ΔT, between target and mismatch sequences. There are two free-solution melting temperature definitions, one for (1) two polynucleotides (made of 13 or more nucleotide monomers), $T_{m,1}$ and for duplexes containing (2) at least one oligonucleotides with another oli- or polynucleotide, $T_{m,2}$.[46] $T_{m,1}$ is defined as the temperature at which 50% of the base pairs in a duplex have been denatured, leading to polynucleotides containing alternating duplex and denatured (loops or ends) regions.[47] $T_{m,2}$ is the temperature at

10

which 50% of the oligonucleotide duplex strands separated. In both cases, because the reaction is intramolecular and equilibrium is achieved, T_m is independent of oli- or polynucleotide concentration and time and is only affected by the composition of the sequences, and the composition of the solvent.[46] Performing DNA hybridization in low stringency conditions (e.g., low temperature, high salt) produces non-specific hybrids. Melting temperature of non-specific hybrids are typically much lower than of complimentary ones. Thus, if one raises temperate (high stringency condition) to surpass the melting temperature of these hybrids, only perfect matches will remain bound.

Temperature also affects the rate of hybridization reactions. At the melting temperature, T_m, the k_{on} rate (define equation) goes to zero.[47, 48] The hybridization rate constant can be expressed as, $k_{on} = k_n' \sqrt{L}/N$, where L is the length of the shortest strand participating in duplex formation, N is the complexity or the total number of base pairs present in non-repeating sequences, and k_n', is the nucleation rate constant.[47] The inverse dependence of k_{on}, on N results from mass action, where at constant concentration, increasing N means a lower concentration of any particular sequence. Because the yield of base pairs for a given nucleation increases as L, the dependence of k_{on} on $\sqrt{L}$, implies that fewer nucleation sites are available for reaction as the molecules get longer. The nucleation rate constant, k_n' is a strong function of salt concentration, temperature and viscosity. k_n' rises steadily as the criterion is increased to 25°C below T_m, than as it increased towards T_m, intramolecular base pair formation occurs, leading to structures that are no longer capable of presenting all possible sequences as nucleation sites. Although the maximum rate occurs at a criterion of 25°C below T_m, higher hybridization

temperatures are often employed to increase the stringency or fidelity of hybridization with excess target.[46]

1.4.2 Electrophoretic separation

In capillary electrophoresis, the primary roles of background electrolytes (BGE) are to provide the transport of electric current and to enable fast, resolvable separation of RNA. Electrophoretic separations rely on differences in ion drift velocities, which depend on solvent viscosity, ionic strength of the electrolyte solution, the degree of ionization of the ion, and solvation of the ion. The temperature sensitivity of viscosity, varying 2% per degree Celsius near room temperature,[49] has a marked influence on the electrophoretic mobility, and is commonly utilized to speed up separations.[50-52] Successful separation also relies on appropriate migration behavior, peak shape and resolution, which are strongly affected by the choice of BGE. For example, Joule heating is well known to limit separation time[53] and induce significant dispersion in electrophoretic separations.[54, 55] The absolute temperature rise in a capillary is often not the problem,[56] but rather radial and, in the case of significant EOF, axial temperature gradients[55, 57, 58] caused respectively by the internal heat generation and differential cooling/coupling to the environment. Temperature gradients in a given separation channel can be decreased by reducing the power dissipated in the channel, EI, where E and I are the applied electric field and current, respectively. To minimize EI, BGE which limits the rise in conductivity with increasing temperature are recommended.

Peak shapes are also strongly dependent on the mobility of the background coions. When an ionic analyte leaves its zone and experiences a higher electric field (in a

12

lower conductivity region), its velocity increases, a behavior that results in a diffuse boundary, and broadening of the migrating zone. This phenomena is known as is electromigration dispersion (EMD).[59-61] For a low number of analyte species, it is possible to reduce EMD by matching a BG coion to the analyte mobilites (analyte zone conductivity to BGE conductivity). Optimization of BGE to minimize the effects of EMD effects is challenging, as the mobilites of both the BGE and the analyte can have unique temperature dependence.

Peak broadening can also occur in the presence of analyte-free system zones (SZ) which migrate through an electrophoretic system. SZs form in BGEs containing two coions, or multivalent coions with pK values close to the sytem pH, and interact with analytes zones of similar mobility.[62, 63]

Despite the importance and prevalence of the various effects, we found no comprehensive models which capture the basic, important contributors of temperature to ion (weak and strong electrolyte) mobilities and electrolyte solution conductivity and pH. We further note that currently available freeware simulation tools (e.g., PeakMaster,[64] Simul 5,[65] SPRESSO[66, 67]) can simulate electrophoretic behavior and electrolyte properties only at room temperature. In this thesis, we aim to provide basic physical insights into the temperature contributions to solution pH, ionic strength and conductivity, the most important solvent parameters in molecular reactions and separations.

1.5 Sequence-specific RNA detection

A wide variety of mechanisms exist for sequence-specific detection of RNAs. These analytical techniques vary in key parameters such as sensitivity, assay length, and complexity of sample preparation.

The polymerase chain reaction (PCR) is perhaps the most important and most common analytical techniques in all of molecular biology. The widespread success of PCR is largely due its unparalleled sensitivity, with the capability of detecting even a single molecule of target NA in 1 h.[68] While this limit cannot always be achieved, in practice PCR can detect reliably in the range of 10–100 molecules.[69-71] In terms of sample concentration, PCR offers by far the highest sensitivity; for example, target molecule concentration in the actual master mix is routinely as low as 1 attomolar.[69] After sufficient sample preparation, PCR itself requires temperature cycling (say, up to 40 cycles) and optical volumetric fluorescence detection. However, PCR is associated with several technical challenges including strong sensitivity to solvent composition[72, 73] and nucleic acid contamination. Furthermore, the issue of amplification bias due to PCR drift[74] and/or PCR selection[74] of one sequence over another is well established.[75] And while there is no theoretical limit to the number of target sequences in parallel PCR,[76] the constraints on establishing optimal PCR conditions generally limit the useful number of target sequences and hence excludes PCR as an affordable and easily reconfigurable solution for massively multiplexed molecular detection.

Next-generation sequencing is another very important and rapidly-advancing technique. Commercially-available sequencing platforms provide an unprecedented

amount of information at an ever-decreasing cost and are expected to transition to the diagnostics market in the future.[77] However, current sequencing technologies require very large amounts of sample (> 100 ng) and have a highly complex and lengthy (~1 day or longer) sample preparation process.[77] While prototypes of more sensitive sequencing platforms requiring on the order of 100 pg of sample have been reported (e.g. Helicos Heliscope), these systems are costly (~$1M), again require lengthy sample prep (up to several days), and have very long running times (~1 week).[78, 79]

Surface-bound probes for RNA capture are effectively employed in microarray technology. Fluorescence-based detection is most common, with a limit of detection of ~10 pM.[15] Electrochemical and magnetoresistive detection methods were introduced recently, with limits of detection also in the 1–10 pM range.[80, 81] Surface-bound probes are easily multiplexed, thus enabling microarrays to simultaneously screen for thousands or even up to 10^6 biomarkers in a single experiment.[82, 83] However, the capture process is limited by both diffusion and slow reaction kinetics, and so incubation times typically exceed 24 hours.[84] Further, the complex sample preparation (target labeling, ligation) and numerous surface treatments (e.g. probe rehydration) required to perform surface-bound assays pose additional significant barriers towards automation and their utility for rapid diagnosis.[85]

An alternative approach to target immobilization is to hybridize DNA or RNA molecules to bead bound oligonucleotide probes. Using Dendrimer fluorescence DNA labeling, DNA detection was demonstrated at a single molecule sensitivity in a Luminex beads assay. The additional 100-color multiplexing capability of the Luminex two-color fluorescent beads makes this assay a particular powerful molecular analysis tool.

However, the Luminex analyzers require expensive instrumentation, and trained technicians to operate. These instruments are also not easily configurable to integrate with upstream sample preparation assays.

Others have implemented a hybrid approach to nucleic acid detection, combining the fast kinetics of beads assays with the supreme multiplexing capability of microarrays achieving impressive sensitivity for ultralow concentration of 500 zM, without PCR amplification.[86] The method developed by the Mirkin lab relies on oligonucleotide-modified gold nanoparticles (NPs) and oligonucleotide-modified magnetic microparticles (MMPs). Both, the MMPs and the NPs contains probes complimentary to target sequence. In addition, NPs contained access probes complimentary to bar-code sequences, holding a unique ID for the target of interest. MMPs and then NPs are incubated with the bar-code sequences and target DNA for 100 min. After MMPs-NPs doublet capture, the beads were washed and the bar-code sequences eluted and hybridized overnight to a microarray for detection.

A more recent publication by Leslie at al.,[87] replaced the microarray hybridization step by directly monitoring the binding events between two oligo-functionalized magnetic beads bound by the target sequence. The assay combined target DNA with oligonucleotide functionalized superparamagnetic beads in a rotating magnetic field and produced multiparticle aggregates. Quantification of dark area (aggregated beads) was correlated to the concentration of target DNA. This assay bypassed the need for fluorescent labeling and detection, as the bead aggregates are reportedly visible with the naked eye. However, due to the nature of aggregation, multiplexing in this assay is

16

limited to monitoring of melting temperature of and associated breakup of bead aggregates under magnetic agitation.

In this dissertation, we developed a different approach to bead-based RNA detection. Instead of monitoring large bead aggregates upon RNA binding, we use two sets of fluorescent beads. Each bead had a unique spectral signature (red and green emission) and each is functionalized with unique DNA probe complementary to a portion of the target. When these probes hybridize to the target DNA, the two beads form a two-color doublet. We load the bead suspension onto a microfluidic chip and image the beads as they electrophorese through the interrogation region. We analyze the spectrally separated bead image sets and look for spectral collocation. Since the beads are suspended freely in solution, we can levarage Brownian motion to separate randomly collocated beads, and distinguish these from those which are deteriminstically bound via the RNA or DNA target.

1.6 Scope of thesis

The objective of this thesis is to improve the state of the art in RNA analysis workflow, with a particular focus on sample preparation, modeling of temperature effects in electrophoresis (and buffers), and bead-based RNA detection methods. We explore methods which we believe are cost effective, simple-to-integrate with other assays steps, and are amenable for automation.

The thesis is composed of three main chapters. In Chapter 2 we demonstrate a novel assay for physicochemical extraction and isotachophoresis-based purification of 16S ribosomal RNA from whole human blood infected with *Pseudomonas Putida*. In

Chapter 3 we present a model capturing the important contributors to the effects of temperature on the observable electrophoretic mobilities of small ions, and on solution conductivity and pH. In Chapter 4, we introduce a new, imaging based cytometry-like assay and custom particle imaging, tracking, and collocation algorithm; and present an experimental demonstration of the method using challenging image data of a flow of randomly distributed Brownian beads undergoing 16S rRNA gene induced bead-to-bead binding. In Chapter 5 we present major conclusions, summarize our main achievements, and present recommendations for future directions for integration and automation RNA analysis.

2 Bacterial RNA Extraction and Purification from Whole Human Blood Using Isotachophoresis

The contents of this chapter were previously published by Rogacs, Qu, and Santiago (2012)[88] and are reproduces here with minor modifications.

2.1 Introduction

Nucleic acid amplification methods, including reverse transcription-quantitative polymerase chain reaction (RT-qPCR), targeting the 16S ribosomal RNA (16S rRNA) enable fast and specific detection of bacteria in complex samples such as whole blood.[89, 90] 16S rRNA is a universal constituent of bacterial ribosomes present at high copy numbers (10^3 to 10^4 per actively growing cell).[91, 92] Targeting these biomarkers can potentially increase assay sensitivity compared to the assays targeting the corresponding DNA.[2, 3] Sample preparation is time-consuming and labor-intensive, involving one or more centrifugation steps, buffer exchange(s), lysing, and associated multi-step processes of nucleic acid extraction and purification from PCR inhibitors. The latter can include endogenous species such as heme proteins, lactoferrin, and immunoglobin, as well as species used in preparation including heparin, denaturants, surfactants, chaotropic salts, and alcohols.[21, 72] These sample preparation steps can be difficult to integrate, automate, or hasten, particularly in a miniaturized system.[25, 93]

Fundamentally, RNA can be an exceedingly challenging blood biomarker due to its extreme lability. RNA is susceptible to the ubiquitous action of ribonucleases

(RNases)[12] and degradation to physicochemical conditions including elevated temperature (>65°C)[1] and high pH.[13, 14, 94] Careful decontamination together with assay standardization or automation can mitigate effects of exogenous RNase, but only careful design of assay chemistry can provide sufficient protection against the abundant endogenous RNases in blood. As one salient example, without adequate RNase control, free RNA is non-amplifiable after 15 s of incubation in plasma or serum.[12]

To date, the majority of microfluidic-based sample preparation approaches have focused on DNA isolation, and mainly via the miniaturization of solid-phase extraction (SPE) methods.[28, 31, 32, 95] SPE-type approaches include specialized structures such as packed beads, monolithic porous structures, and magnetic beads. These approaches are well-established in traditional settings but require multiple reagent wash steps and specialized fabrication or manipulation (e.g., pumping liquids for wash steps or moving magnets for beads). Further, SPE binding capacity can be low due to competitive protein absorptions (e.g., to silica) and the presence of PCR inhibiting chemistry such as guanidinium thiocyanate (GuCN), guanidinium chloride (GuHCl), isopropanol, or ethanol. Of the few studies reporting RNA purification using a microfluidic platform,[6, 33-39] to our knowledge only two have reported using blood or blood product as a sample matrix.[33, 34] Witek *et al.* employed an array of photoactivated polycarbonate micropillars as the solid-phase to purify total RNA from bacterial cells suspended in whole blood.[34] Their protocol eliminated the PCR-inhibiting guanidine chemistry by adopting thermal and mechanical lysing approaches. They also report a high, post-extraction RNA integrity. However, their assay did not address the need for adequate RNase control[34, 92] (see Tsui *et. al*[12] for a discussion of RNA stability in blood products). We attribute their

20

high RNA integrity to the very large number of bacteria they spiked into their blood sample. We estimate they spiked 18000 ¢/nL-blood (where ¢ is the number of bacteria), which is order 10^6-fold higher bacteria concentration than the current work. Further, their protocol required ethanol, which can inhibit PCR if not sufficiently removed.

Instead of SPE, Root et al.[33] used an oligonucleotide polymer capture matrix to purify free RNA spiked into serum. This aqueous purification process reported an impressive 375 RNA copies/μL-serum.[33] However, very importantly, the Root assay included no lysing strategy; instead, they demonstrated purification by spiking free RNA into a pre-prepared serum sample which already contained 0.5% w/v concentration of lithium dodecyl sulfate, a powerful RNase inhibitor.

We know of no reports of miniaturized systems which can extract RNA from blood or blood lysate at RNA copy numbers which is within a factor of about 10^5 orders of magnitude of clinically relevant RNA levels. For that matter, we know of no studies which have combined lysing and RNase control into a single chemistry. There is therefore still a significant need for a microfluidic assay which has adequate RNase control and can enable direct integration of lysis, nucleic acid purification (particularly RNA), and provide nucleic acid samples compatible with amplification methods.

Isotachophoresis (ITP) offers an alternative approach to nucleic acid extraction and purification, and the input and output reagents used in ITP can be compatible, respectively, with lysis and RNase control, and amplification. ITP does not require specific surfaces, specialized geometries, or pumping of reagents. As shown in **Figure 2.1a**, ITP uses an electric field to extract and preconcentrate only target analytes whose

electrophoretic mobility is bracketed between the anions of its trailing (TE) and leading electrolytes (LE). Anionic inhibitors with mobilites lower than of the TE do not focus, but do electrophorese into the microchannel.
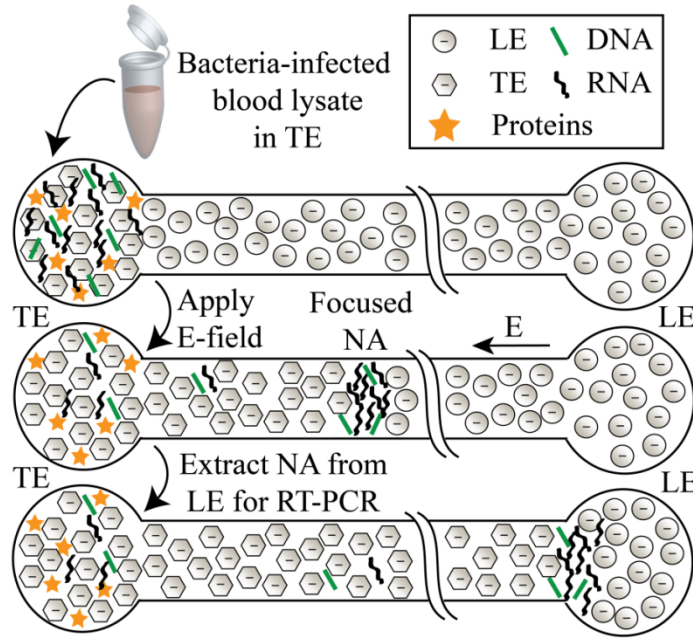
Figure 2.1 Schematic of the ITP-based NA purification from a complex biological sample such as blood lysate. After dispensing the lysate containing TE into the well (top left of schematic and top channel), an electric field was applied (middle channel), and the total NA migrated into the microchannel, where it was focused and purified into the ITP interface. This process enables PCR inhibitors (including proteins) to remain unfocused in the TE well (e.g., cations) or in channel regions well separated from the ITP zone. After the total NA elutes into the LE well (bottom channel), the content was extracted using a standard pipette. We then split this extract into two equal 4 ul aliquots for parallel off-chip RT-qPCR and qPCR analyses.

The separation distance between these potentially PCR-inhibiting contaminants and the focused nucleic acid in the ITP zone increases over time. For a channel length, L, the separation distance between the ITP and the inhibitor zone front, ΔL, can be expressed as $\Delta L = \left(1 - \mu_i / \mu_{TE}\right)L$, where μ_i and μ_{TE} are the inhibitor and TE anion mobilities,

22

respectively. For example, the zone front of an inhibitor with mobility $\mu_i = 0.9\mu_{TE}$ will lag 0.6 cm behind the ITP zone at the end of our 6 cm microchannel. ITP is a highly sensitive,[96, 97] robust[40, 98] sample preparation method which can, under ideal conditions, provide up to one million-fold preconcentration.[41] We have demonstrated successful ITP extraction of small RNA from cell culture lysate;[99] micro-RNA from total RNA;[100, 101] genomic DNA (gDNA)[102] and pathogenic DNA (malaria)[103] from whole blood lysate; and rRNA from bacteria in urine lysate.[104] However, no previous nucleic acid extraction protocols using ITP have been designed for adequate RNase control and RNA integrity.

2.2 Materials and methods

A schematic of our extraction process is shown in **Figure 2.2**. We started with human whole blood infected with known concentrations of *Pseudomonas Putida* cells. We chemically lysed the blood at room temperature for 1 min in a mixture of sodium hydroxide (NaOH) (pH >12), Dithiothreitol (DTT) reducing agent, Triton X-100 non-ionic surfactant, and synthetic carrier RNA. We then "quenched" this high pH with ice-cold TE buffer, and then directly pipetted this combined lysate and TE into the input well of a microfluidic chip with a single connecting channel (and single output well) pre-filled with LE. We placed 600 μm diameter platinum wire electrodes into the wells, and applied +1000 V to the extraction well and grounded the TE well using Keithley 2410 sourcemeter. We recorded current versus time using the sourcemeter interfaced with a computer running a custom Matlab (Mathworks, Inc) script. As shown in **Figure 2.4**, with constant voltage applied, the current monotonically decreased as the ITP zone (containing the focused NA) advanced in the channel, and as the lower-conductivity

trailing electrolyte (TE) replaced the higher-conductivity leading electrolyte (LE). The current signal plateaued near $t = 220$ s, coincident with the time at which the focused NA eluted into the extraction well. With a standard pipette, we gently mixed the content of the extraction well and collected 4 µl aliquots for each of the off-chip RT-qPCR and PCR assays. In this study, we also performed SYBR Green based NA visualizations to provide supporting evidence for the extracted and purified NA, however, the process can be performed by monitoring current alone.

PSEUDOMONAS PUTIDA AND BLOOD SAMPLES: Blood samples from healthy donors were collected in heparin tubes at the Stanford Blood Center. Aliquots of 100 µL blood were prepared and stored at -80°C. *Pseudomonas Putida* cells were purchased from ATCC (#12633), and cultured in Luria Broth (Invitrogen) at 37°C to a final concentration of 3e6 ¢/mL, and quantified by the plate count method. Bacteria suspensions were pelleted before diluting them in blood at $3x10^7$, $3x10^6$, $3x10^5$, and $3x10^4$ ¢/mL concentrations, and were stored at -80°C.

LYSIS: We lysed 20 µL of whole blood with suspended *P. putida* using a mixture of 1% Triton X-100, 125 mM NaOH, 40 mM DTT and 0.4 mg/mL carrier polyA RNA. After 1 min of incubation at room temperature, we mixed 10 µL of lysate with 90 µL of ice-cold TE buffer (28 mM HEPES, 1% Triton X-100, pH~7.4).

24
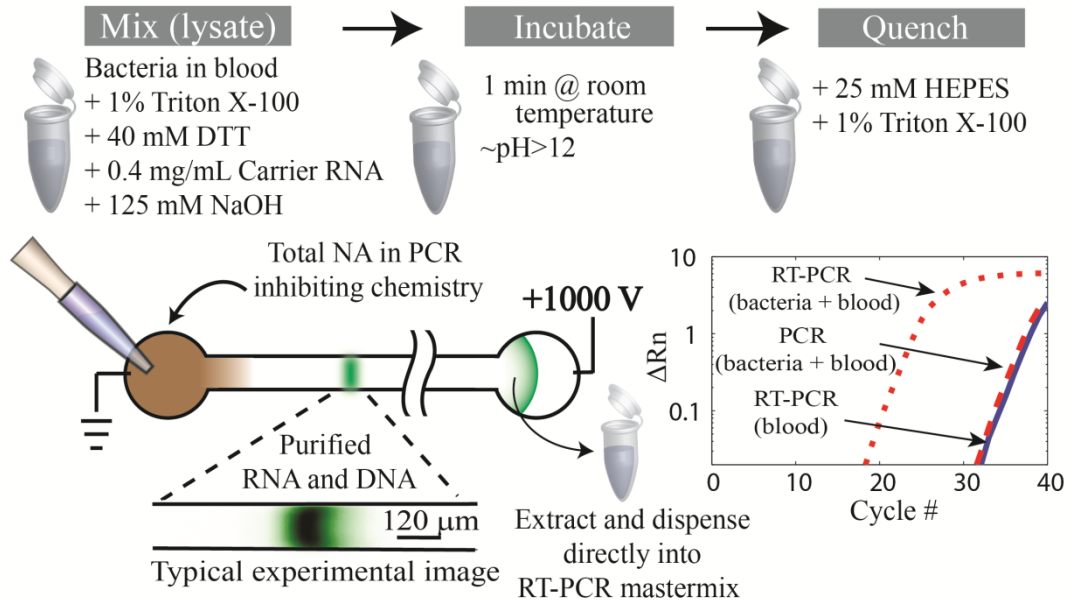
Figure 2.2 Schematic summarizing protocol with one mixing and two dispensing steps for otherwise automated on-chip RNA extraction from whole blood. TE mixed with lysate (brown) contains target nucleic acid (green), proteins, and potential PCR-inhibiting chemistries. Appropriate selection of trailing and leading ions enables selective focusing of target nucleic acid while leaving PCR inhibitors behind. The detail view shows on-chip extraction of RNA from blood stained with SYBR Green II, focused into a concentrated zone. The amplification plot shows the result of alkaline based lysing (enhanced with Triton X-100, DTT and carrier RNA) of total nucleic acid from whole blood spiked with *P. Putida at* 30 ¢/nL, followed by purification of total NA from lysate using ITP. The NA collected from the output well was split to perform both RT-qPCR and qPCR to verify successful extraction of 16S rRNA (red dotted) and 16S rDNA (red bold dashed). For the negative control template (uninfected blood) RT-qPCR amplified 16S rRNA (blue solid line) above 30 cycles and qPCR did not amplify 16S rDNA within 40 cycles, as expected.

ITP EXTRACTION: The leading electrolyte used to fill the microchannel, LE1, contained 1 U/μL Rnasin Plus, 0.1% Triton X-100, 1% 1.3 MDa poly(vinylpyrrolidone) (PVP) and 1X SYBR Green II in 100 mM Tris hydrochloride (Tris-HCl) at pH 7.5. The PCR-compatible leading electrolyte, LE2, contained 1 U/μL Rnasin Plus, and 1% 1.3 MDa PVP in 20 mM Tris-HCl at pH 7.5. We added PVP to LE to suppress electroosmotic flow and Triton X-100 to TE and LE to aid solubility of the denatured proteins.

25

Triton X-100, NaOH, Tris, HEPES, and HCl were obtained from Sigma-Aldrich (St. Louis, MO), DTT, carrier RNA, and SYBR Green II were obtained from Invitrogen (Carlsbad, CA), PVP (MW 1.3 MDa) was purchased from ACROS Organics (Thermo Fisher Scientific, NJ) and RNasin Plus was purchased from Promega (Madison, WI). All solutions were prepared in UltraPure DNase/RNase free deionized (DI) water (GIBCO Invitrogen, Carlsbad, CA).

CHANNEL PREPARATION: We performed isotachophoretic purification of RNA on a 60.7 mm long, 120 um wide, 35 um deep Crown glass microchannel (NS12A) interfaced with 3.5 mm deep and 3.5 mm diameter wells from Caliper Science Life Sciences, CA. Before first use, we rinsed the channel (**Figure 2.3**) with the following successive washes: methanol (2 min), DI (1 min), 1 M HCl (2 min), DI (1 min), 1 M NaOH (10 min) and DI (1 min). Between experiments, we rinsed the channel with 10% household bleach for 2 min to remove any residual nucleic acid contaminants and then with washes of 1 min DI, 10 min NaOH and 1 min DI. To fill channel with LE1, we dispensed 10 μl of LE1 into well 1, 2, and 3, and applied vacuum to well 4 for 1 min. We carefully emptied well 1 and filled it with 10 μl of the PCR compatible LE2, and emptied, rinsed and filled well 4 with 10 μl lysate containing TE. As the final step, we placed 600 μm diameter platinum wire electrodes into the wells and applied 1000 V to initiate ITP. After the total NA zone together with small amounts of TE anions eluted to well 1, we gently mixed the content of this well and aspirated 4 μl for the RT-PCR and another 4 μl for the PCR assays.
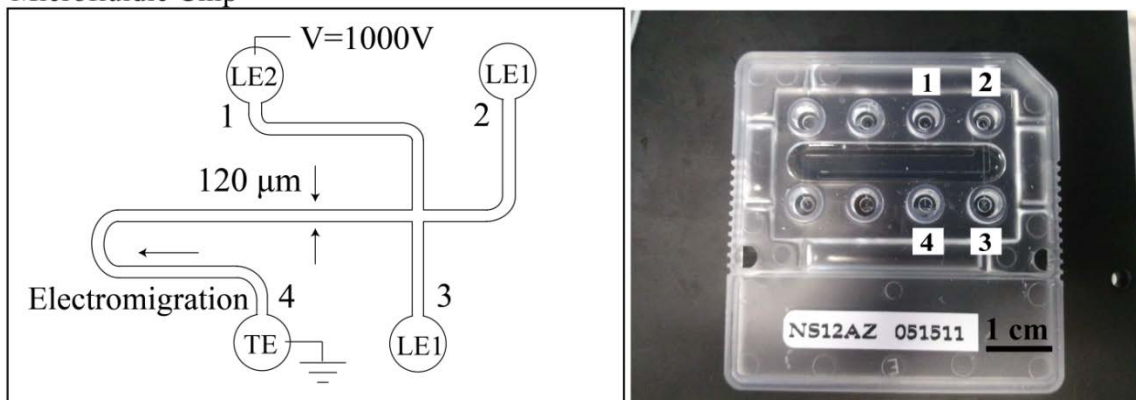
Figure 2.3 Microfluidic chip geometry. We performed isotachophoretic purification of NA on a $L_{1-4} = 60.7$ mm long, 120 um wide, 35 um deep Crown glass microchannel (NS12A) interfaced with 3.5 mm deep and 3.5 diameter wells from Caliper Science Life Sciences, CA. The wells sit open and exposed to room air during ITP.

IMAGING SYSTEM: We performed on-chip visualizations using an inverted epifluorescence microscope (Nikon Eclipse TE300) (Nikon, Tokyo, Japan) equipped with a 10x objective (Plan, NA 0.30 (Nikon, Tokyo, Japan). A blue LED (Thor Labs, Newton, NJ) was used for excitation of SYBR Green II (Invitrogen, Carlsbad, CA) nucleic acid dye. We used a filter cube optimized for detection of FITC (FITC-A-Basic, Semrock, Rochester, NY) and a 0.5x demagnification lens (Diagnostic Instruments, Sterling Heights, MI). We captured images using 512x512, 16 bit, CCD camera (Cascade 512F, QImaging/Photometrics, Canada). We controlled the camera using Winview32 (Princeton Instruments, Trenton, NJ) and processed the images with MATLAB (R2007b, Mathworks, Natick, MA).

TIMING: We recorded current over time using the sourcemeter interfaced with a computer running a custom Matlab (Mathworks, Inc) script. As shown in **Figure 2.4**, with constant voltage applied, the current monotonically decreased as the ITP zone

27

(containing the focused NA) advanced in the channel, and as the lower-conductivity trailing electrolyte (TE) replaced the higher-conductivity leading electrolyte (LE). The current signal plateaued near $t = 220$ s, coincident with the time at which the focused NA eluted into the extraction well. In this study we performed SYBR Green based NA visualizations to provide supporting evidence for the extracted and purified NA; however, one can perform these experiments by monitoring current alone.
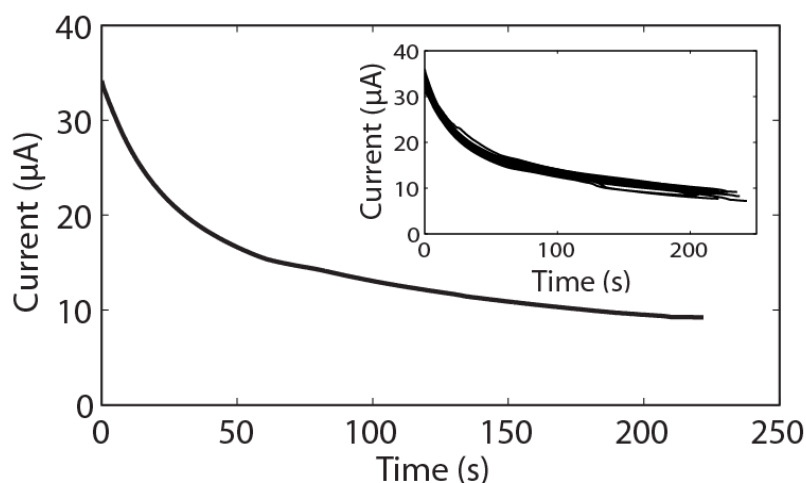
Figure 2.4 Main plot shows a representative trace of measured current *versus* time. Current can be used to control the timing of the experiment. **Inset:** Overlayed raw current measurements for 18 experiments (13 infected samples shown in figure 2 of the manuscript, and 5 negative controls) performed on a single chip. These repeats have a coefficient of variation of less than 6%.

RT-qPCR and qPCR: We used off-chip RT-qPCR and qPCR to validate the purity of our sample and PCR compatibility of our ITP assay. We added 4 µL of total nucleic acid extract from the chip's output well to a PCR tube containing 10 µl Power SYBR® Green RT-PCR Mix (2X) (Applied Biosystems), 0.16 µl RT Enzyme Mix (125X) (Applied Biosystems), 5.84 µl RNase free water, and 150 nM primers targeting 16SrRNA of *P. putida*. The forward (5'-CAAAACTGGCAAGCTAGAGTACG) and reverse

28

(5'-TAAAATCTCAAGGATTCCAACGGCT) primer sequence reagents were purchased from IDT. To confirm that the RT-qPCR amplification is specific to the RNA of the 16S rRNA gene, we also performed parallel qPCR reactions without the RT enzyme for each ITP extraction. We performed off-chip RT-qPCR and qPCR using a real-time PCR thermocycler (7500 Fast, Applied Biosystems, Carlsbad, CA) with the following thermal profile: 30 min initial hold at 48°C, followed by 10 min hold at 95°C and 40 cycles composed of 15 s denaturation at 95°C and 1 min annealing and extension at 60°C. We obtained post-PCR dissociation curves using the same instrument.

2.3 Results and discussion

2.3.1 Assay design and evaluations

The design of a sample preparation process requires careful evaluation of the integration and interrelation of each of its steps. For example, we observed that choices of specific initial lysing steps can have profound influence on the efficiency of the final analysis (e.g., compatibility with enzyme-based amplification). We designed the current sample preparation method for compatibility and use with PCR. Each of the following sections describes a major process step or chemistry; a brief reasoning for or background behind its inclusion; and a brief description of its integration with the rest of the assay.

LYSIS: Guanidinium-based lysing followed by phenol-chloroform extraction and ethanol precipitation is the gold standard chemistry for RNA isolation from whole blood.[26] When combined with enzymes (e.g.: lysozyme), strong detergents (e.g.: sodium dodecyl sulfate, SDS), and chelating agents (e.g.: ethylenediaminetetraacetic acid), the guanidinium-based approach can also be used to lyse bacterial cells suspended in blood.[105] However, the high

ionic strengths (e.g. >500 mM) of these mixtures require careful purification including wash and buffer exchanges as SDS, chaotropic agents, organic solvents, and alcohols are strong PCR inhibitors. We rejected these here because high ionic strength (especially when including high mobility anions) can be challenging to integrate with ITP. Instead, we opted for alkali-based lysis. The alkali approach is widely used for isolation of plasmid DNA from bacterial cells,[106] but it is not commonly applied for RNA isolation, likely due to the instability of RNA at high pH.[107] While incubation in NaOH may contribute to some RNA degradation, we found it had negligible effect on RT-qPCR amplification of our target RNA sequences. For example, in a set of preliminary experiments (data not shown), we found negligible differences in RT-qPCR threshold cycle for samples of pre-purified (using a standard SPE column, PureLink RNA Mini kit from Life Technologies Corp., Carlsbad, CA) 16S rRNA with and without treatment with 125 mM NaOH for 1 min. With respect to lysing, we found (again, through preliminary repeated trials and lysing quantitation studies) that this 1 min incubation (required to protect RNA) showed lysing performance on par with even 5 min of 130 mM NaOH or higher concentration (data not shown).

RNASE CONTROL: RNA is easily hydrolyzed at elevated temperature, and at either alkali or acidic conditions. Further, its stability is significantly compromised by the abundance of ribonucleases (RNases) in blood. Tsui et al. showed that free RNA can no longer be amplified after incubation in blood plasma for 15 s![12] RNase activity requires its disulfide (S-S) bond be intact. While NaOH can reduce these S-S bonds, the half-life of RNase in 0.2 M NaOH is ~30 min.[108] Meanwhile, as we have mentioned, long incubation in alkali conditions degrades RNA. However, RNase degradation can be

greatly accelerated during alkali lysing by adding detergents (e.g., SDS), and/or reducing agents (e.g., DTT).[109] While ITP can be compatible with anionic detergents, we found that the addition of a reducing agent alone, 40 mM DTT to 125 mM NaOH in the presence of 1% non-ionic detergent (Triton X-100), results in adequate mitigation of RNA degradation in our assay. We hypothesize that this mixture adequately destabilizes and covalently destroys disulfide bonds of the normally very stable RNases even during 1 min of incubation.

After the lysate is quenched to normal pH, residual RNase may be present. To inhibit the activity of the remaining ribonucleases, we explored the use of formamide as the solvent for the lysate and TE. While pure formamide stabilizes RNA in the presence of RNase,[110] we found (again through preliminary work) that a combination of 50% formamide and 20% blood unfortunately resulted in enhanced RNA degradation. Similar observations were reported by Strauss and Sinsheimer[111] in an evaluation of initial kinetics of RNA degradation by pancreatic ribonucleases. Instead of formamide, we opted for an indirect approach: the addition of carrier RNA. The term 'carrier RNA' refers to exogenous RNA spiked into a sample.[112] Addition of carrier RNA to lysate reportedly enhances the recovery of low traces of DNA and RNA in ethanol precipitation[113, 114] and SPE-based extraction[35, 115] procedures. In our application, we spiked large amounts of polyA synthetic carrier RNA sequences into the lysate to serve as a competitive substrate for RNase activity. That is, we hypothesize that the abundant carrier RNA reduces enzymatic activity on our trace-concentration, target RNA by acting as a high abundance inhibitor to RNase. **Figure 2.5** summarizes example preliminary experiments we performed in part to

confirm our hypotheses concerning the combined effect of both DTT and carrier RNA on target RNA stability and recovery.
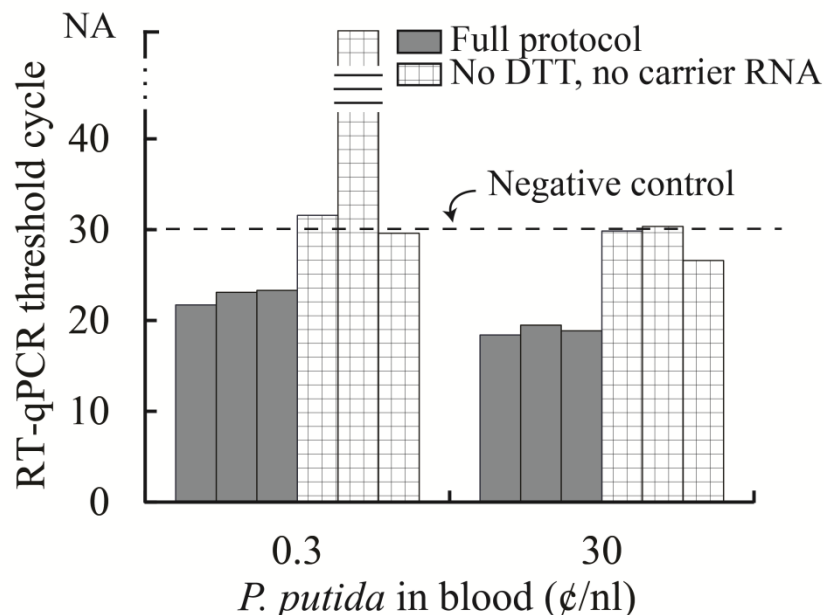
Figure 2.5 Experimental demonstrations of the combined effect of reducing agent (DTT) and carrier RNA on ITP-based RNA purification from bacteria infected human blood. The bars show RT-qPCR threshold cycles for 16S rRNA extracted from blood spiked with *P. putida* cells. All negative controls for RT-qPCR (RNA extracted from uninfected blood) amplified above 30 cycles. We show results from four sets of experiments. Lysing in the presence of DTT and carrier RNA yields consistent and low threshold amplification cycles for two different bacterial cell densities. In their absence, all bacterial RNA extractions failed, or were significantly compromised. We believe that the observed effect is primarily due to the presence of DTT. However, we hypothesize that carrier RNA would have significant effect on extraction efficiency at very low RNA concentration (which includes RNA from the background matrix). The latter hypothesis is supported by the typically higher variation in threshold target levels for the "no DTT, no carrier RNA" case at lower bacteria concentrations, such as the example data shown here. NA indicates no amplification within 40 cycles.

Lastly, to further guard against exogenous RNase contamination and residual RNase from lysate, we also included PCR compatible RNase inhibitor RNasin Plus (Promega) in the LE.

32

ITP CHEMISTRY: In addition to requiring TE and LE anions with mobilities which bracket that of RNA, the ITP chemistry prompted two additional concerns: pH and ionic strength. Again, throughout the course of a series of preliminary experiments, we observed severe repeatability problems at lower pH 5-7 (e.g., using Bis-Tris as the buffering weak base). We attribute these to the effects of (observed) protein aggregation and protein adsorption to channel walls.[116, 117] Recovery efficiency stabilized at pH ~7.5, and so we chose Tris as the buffering counterion. We also quantified LE buffer compatibility with RT-PCR (via independent, *ex situ* runs with the PCR system) and found no change in the amplification efficiency when using 20 mM Tris-HCl (pH = 7.5) as the sample buffer added to the RT-PCR mastermix. We filled the channel with 100 mM Tris-HCl (pH = 7.5) to improve the rate of nucleic acid accumulation[42] but used 20 mM Tris-HCl (pH = 7.5) as the LE buffer in the extraction well. The latter chemistry provided a good balance between PCR compatibility and buffering capacity in that well.

2.3.2 Demonstration of extraction purity and compatibility with RT-qPCR

FLOURESCENCE IMAGING: We monitored accumulation of RNA during ITP by visualizing the scalar fluorescence of RNA specific-intercalating dye, SYBR Green II. **Figure 2.6** illustrates results of extractions from blood containing 0 and 30 ¢/nL *P. putida* cells. Our 1X concentration of SYBR Green II (in original LE1; equivalent to 0.003X concentration in the final PCR mix) showed no observable effect on amplification signal.
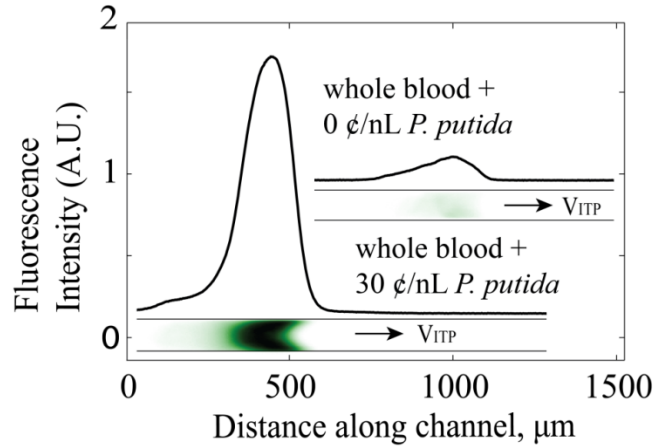
Figure 2.6 Example on-chip fluorescence images and experimental integrated fluorescence curves of extracted nucleic acid ITP zones stained with SYBR Green II. The inset fluorescence profile and image on the top right shows RNA extracted from uninfected blood (negative control). The main fluorescence plot and image at the bottom corresponds to a typical run with blood infected with *P. putida* at 30 ¢/nL concentration. We corrected the ITP-focused nucleic acid fluorescence images by subtracting a background fluorescence image and dividing this by the difference between a flat field image and the background image (see the supplementary information document of Persat et al. for further details). For the fluorescence peak distribution, we integrated image intensities along the width of the channel and show here versus distance along the channel's main axis. These image analysis and fluorescence integrations were performed using MATLAB (The Mathworks, MA).

RT-qPCR AND qPCR: **Figure 2.7** shows typical RT-qPCR threshold cycles for 16S rRNA extracted from *P. putida* suspended in whole human blood. We explored bacterial cell densities ranging four orders of magnitude from 0.03 to 30 ¢/nL.
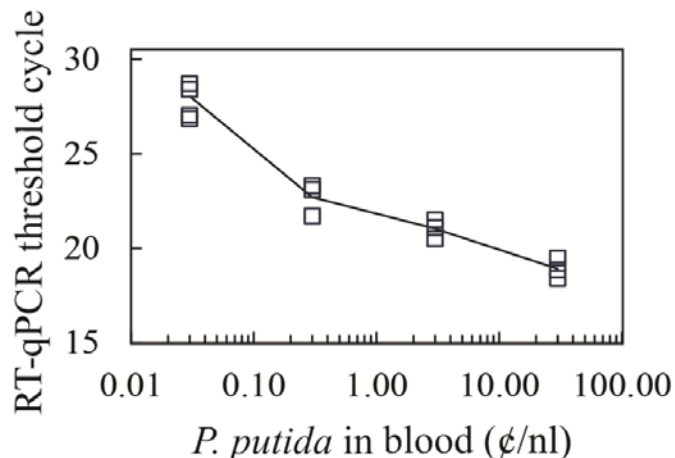
Figure 2.7 RT-qPCR threshold cycles for 16S rRNA extracted from whole human blood infected with *P. putida* using our DTT- and carrier-RNA-assisted, alkaline-based lysing and ITP purification protocol. Plot contains results for a total of 13 experiments, four at 0.03 ¢/nL and three each at 0.3, 3 and 30 ¢/nL bacterial cell concentrations. All negative controls for RT-qPCR (RNA extracted from uninfected blood) amplified above 30 cycles, as expected (not shown). Threshold amplification cycles for the (non RT) qPCR reactions targeting DNA were above 30 for all experiments, also demonstrating our sensitivity to RNA *versus* DNA.

In **Figure 2.8** we show examples of raw data from RT-qPCR reactions containing ITP-processed, lysed blood with and without bacteria. We observed no amplification below 30 thermal cycles for the negative controls in either the RT-qPCR or qPCR reactions. (Low threshold cycles associated with negative controls are, of course, a sign of contamination of the RT-PCR master mix and/or ITP buffers.) Amplified sequences dissociated at ~82°C, a measured temperature which matches the calculation from theory for dissociation temperature (mFold, RNA Institute, University of Albany, Albany, NY).
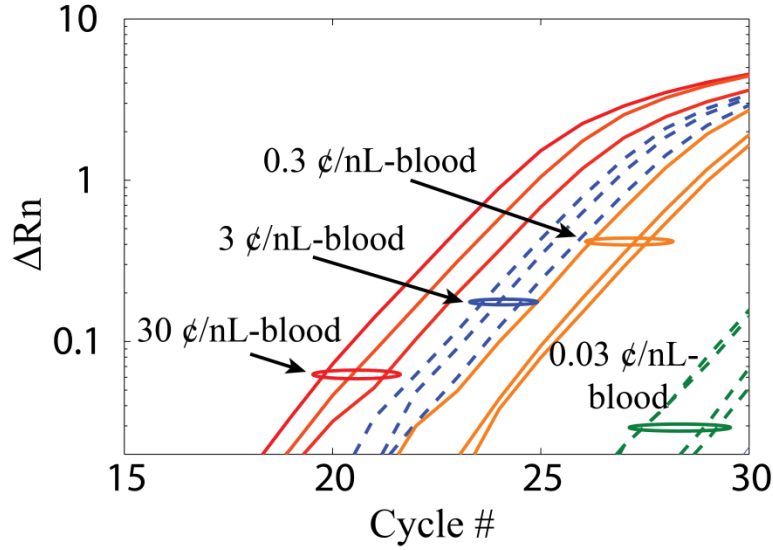
Figure 2.8 Shown are the raw reverse transcription polymerase chain reaction (RT-qPCR) amplification curves for the data shown in Figure 2 of the main paper for *P. putida* 16S rRNA. *P. putida* was spiked into whole human blood to final concentration of 0.03, 0.3, 3, and 30 ¢/nL. We performed RT-qPCR using *Power* SYBR Green RNA-to-C_T *1-Step Kit* from Applied Biosystems with 150 nM forward (5'-CAAAACTGGCAAGCTAGAGTACG) and 150 nM reverse (5'-TAAAATCTCAAGGATTCCAACGGCT) primers, with the following thermal profile: 30 min initial hold at 48°C, followed by 10 min hold at 95°C and 40 cycles composed of 15 s denaturation at 95°C and 1 min annealing and extension at 60°C. Negative RT-qPCR reactions (template: uninfected blood), and all PCR reactions amplified above 30 cycles.

DETECTION LIMITS: We detected *P. putida* infected whole blood at bacterial cell concentration of 0.03-30 ¢/nL-blood (4.5-8.5 $\log_{10}$¢/mL-blood). With the current channel design, our sensitivity is limited by contamination of our reagents with 16S rRNA. We hypothesize that we can improve sensitivity with a more carefully sterilized, dedicated lab space for RNA extraction work. In comparison, our sensitivity is still 6 orders of magnitude greater than the only other microfluidic RNA extraction from whole blood lysate, as reported by Witek *et al*.[34] On the other hand, Mahalanabis *et al*.[95] presented a method for on-chip DNA extraction from bacteria infected whole blood using an SPE-

36

based extraction method which processed about 100 μl of whole blood using a protocol with five reagent pumping steps, and which achieved 10^2 ¢/mL sensitivity. This sensitivity is order 300 fold higher than our assay, but used about 5 orders of magnitude higher processed sample volume than our assay's ~1 nL processed volume. We hypothesize that we can exceed this sensitivity by scaling up the geometry of our channel to process order 1000 fold higher sample volume (order ~1 μl), and hope to demonstrate this in future work.

In addition to the *P. putida* results we present here, we have also successfully performed RNA extraction from *E. coli* cells suspended in whole blood (data not shown). Together, our more extensive *P. putida* work and our limited work with *E. coli* suggest that our protocol can be successfully adapted to RNA extraction and detection from many gram-negative bacteria species by simply changing the primer sequence and thermal cycling conditions for RT-qPCR. One particular application that may benefit from our technique is diagnosis of *Menigococcemia*, an acute and potentially life-threatening infection of the bloodstream caused by bacteria *Neisseria meningitidis*. One large study including 1045 adult patients evaluated the full range bacterial loads upon hospital admission, 2.87 – 6.3 $\log_{10}$¢/mL,[118] using qPCR analysis of whole blood samples for *N. meningitides*. Another study, including a smaller cohort of 51 pediatric patients reported a slightly higher *N. meningitides* load range of 4.3 - 8.2 $\log_{10}$¢/mL[119] using a similar qPCR-based assay.

3 Temperature Effects on Electrophoresis

The contents of this chapter were previously published by Rogacs and Santiago (2013)[120] and are reproduces here with minor modifications.

3.1 Introduction

The fields of drug discovery, genetics, proteomics, toxin detection, and food analysis, among others, employ electrophoretic separation as a workhorse analysis technique. Electrophoresis methods include capillary electrophoresis (CE), isotachophoresis (ITP), isoelectric focusing (IEF) and temperature gradient focusing (TGF); all of which rely on differences between analyte electrophoretic mobilities for separation.[53] A wide range of these methods use temperature variation to improve performance and enable new functionalities. Likely the most common utility of elevated temperature is speeding up electrophoretic separations.[50-52] For example, compared to room temperature, CE separation times can be reduced by 2.5-fold at 70°C.[52, 53] Other uses include improvement of resolution by changing the degree of ionization of analytes,[121-127] and manipulation of nucleic acid secondary structure[52, 128] or protein conformation.[129, 130] TGF specifically relies on temperature gradients to focus and separate analytes.[131, 132] Temperature effects on electrophoresis can also cause non-ideal behavior, including experimental variability, Joule-heating-induced zone dispersion,[54, 56, 57] and increased electromigration dispersion.[59, 133] As we will discuss, a 5°C temperature change can produce as much as 0.1 units change in the pH, and over 25% change in observable mobility of analytes at specific conditions.

38

The observable mobility of an ion depends on the solvent viscosity, ionic strength of the electrolyte solution, the degree of ionization of the ion, and solvation of the ion. The temperature sensitivity of viscosity, varying 2% per °C near room temperature,[49] has a marked influence on electrophoretic mobility, and is typically modeled using the so-called Walden's rule. Similarly, the strong temperature dependence of ion dissociation constant (K) can have pronounced influence on the degree of ionization and so the observable mobility of an ion. We here refer to only acid dissociation constants, K_a and never the related base equilibrium constants, $K_a = K_W/K_a$, so we drop the ''a'' with no ambiguity.)   As we shall discuss, neglecting this effect can result in gross errors in prediction for buffer pH (e.g., greater than 0.5 pH unit), buffer conductivity (>100%) and effective mobility of analytes (>400%) at 80°C (all relative to room temperature, see Supporting Information for details). Although commonly used, Walden's rule does not hold for some small ions like potassium or chloride, which are poorly hydrated at low temperatures. Neglecting temperature dependence of hydration shell for small ions (e.g., K+ or Cl-) can result in as much as ~20% error in the predicted absolute mobilities over a 70°C change.[134]

In general, the contributions to electrophoretic mobility from temperature dependence of electrolyte ionization, ionic strength corrections, and ion solvation, have been largely overlooked.[135]   In **Table 3.1**, we show the results of a brief survey of temperature effects addressed by published models, and compare these to the current work.   Most of these studies explored temperature effects on one of two types of electrolyte properties, but not on both. These two types are (1) weak electrolyte pK, (e.g., Okamoto et al.[136]) and (2) the 'actual' mobility of fully ionized electrolytes. (e.g.,

Anderko and Lencka[137]) In **Table 3.1**, we indicate with a dash if temperature effects on an electrolyte property were not considered in (or if property was not relevant to) the study. Despite the importance and prevalence of the various effects, we found no comprehensive models which capture all important contributors of temperature to ion (weak and strong electrolyte) mobilities and electrolyte solution conductivity and pH. For example, we know of no studies of temperature effects on electrolyte properties which capture both solvation effects and dissociation effects, nor models including ionic strength corrections to both pK and absolute mobility.

Table 3.1 Examples of temperature models of aqueous electrolyte solutions from the last 25 years. Effects captured by each model are categorized into two types: pK or actual mobility, μ^o corrections. Abbreviation 'dpK/dT' indicates that only tabulated values of this slope were presented. 'pKC-VC' and 'pKC-CG' represent models which account for temperature dependence of pK using van't Hoff or the higher accuracy Clark-Glew model, respectively. Viscosity corrections using of the Walden rule type are indicated with 'W'. We also list models which account for the temperature dependence of ionic strength corrections of activity coefficient ('ISC-pK') and actual mobility ('ISC-μ').

References	Acid dissociation constant, $pK(T)$	Actual mobility, $\mu°(T)$
Clancy (1987)[138]	dpK/dT, ISC-pK	-
Rush et al. (1991)[129]	-	W
Whang and Yeung (1992)[126]	dpK/dT	W
Chang and Yeung (1993)[127]	dpK/dT	W
Beynon and Easterby (1996)[139]	dpK/dT	-
Okamoto et al. (1997)[136]	pKC-VH, ISC-pK	-
Anderko and Lencka (1997)[137]	-	W, ISC-μ, SSC
Fukada and Takahashi (1998)[140]	pKC-VH, pKC-CG	-
Rochu et al. (1999)[130]	-	W
Wang and Tsao (2004)[141]	-	W
Reijenga et al. (2007)[142]	dpK/dT	W
Evenhuis et al. (2007)[135]	-	W, ISC-μ
Mandaji et al. (2009)[143]	dpK/dT	W
Milanova et al. (2011)[144]	-	W
Current work	pKC-VH, pKC-CG, ISC-pK	W, ISC-μ, SSC

A fully comprehensive model for temperature effects on electrophoretic mobility is challenging as temperature change may lead to ad hoc and difficult-to-predict effects including variations in DNA gel migration dynamics,[145] sieving matrix properties,[146] and electroosmotic flow (EOF).[147] However, the basic phenomena associated with the mobility of weak electrolyte ions in water and the electrolyte solution pH are addressable using a fairly general model. These basic phenomena can be used to directly predict temperature-dependence of electrolyte solution pH and conductivity, and analyte mobility; likely the most relevant parameters in any separation assay.

We here present a fairly comprehensive model to quantify the effects of temperature on analyte mobility and solution conductivity. Our model includes temperature dependence of (1) viscosity, (2) ionic strength corrections on both mobility and pK, (3) degree of ionization (pK), and (4) ion solvation effects on mobility. Our model leverages thermophysical data for water viscosity;[49] temperature dependence of the Onsager-Fuoss model for finite ionic strength effects on mobility;[148, 149] temperature dependence of the extended Debye-Huckel theory for correction of ionic activity;[149, 150] the Clarke-Glew generalized approach[151] to predict $K(T)$ from tabulated thermodynamic properties;[152] and species-specific, empirically evaluated correction terms for temperature-dependence of Stokes' radii of 11 common small ions.[134] We validated our model using a series of conductance and pH measurements across a temperature variation of 25°C to 70°C for a set of electrolyte solutions routinely used in electrophoresis.

3.2 Theory

We define the mobility of species i, μ_i, as the drift velocity of the ion through the solvent divided by the applied electric field magnitude, E. As usual, we define the 'limiting' (or absolute) mobility of an ion in solution as the mobility that a fully ionized ion would take in the limit of infinite dilution and with known integer values of its valence. At finite ionic strength, the 'actual' mobility of an ion is obtained by considering the effect of the ionic atmosphere on the movement of the fully ionized ion.[66] For weak electrolytes, the observed or 'effective' electrophoretic mobilities are dependent on the degree of dissociation of the analyte. We here summarize the models describing the temperature effect on limiting, actual, and effective ionic mobilites. These include temperate dependent variations of viscosity, dielectric constant, ion solvation, ionic strength effects, and dissociation constants.

3.2.1 Walden's rule

The limiting mobility, μ_i^o, of ionic species i, can be formulated as a balance between the applied electric force and retarding frictional forces acting on the ion. For infinite dilution, this balance can be approximately modeled by a form of Stokes' drag law as follows:

$$\mu_i^0 = \frac{z_i e}{6\pi\eta r_{s,i}}.$$

(3.1)

Here z_i is the valence of the ion, e is the elementary charge (electron charge), η is the dynamic viscosity of the solvent, and $r_{s,i}$ is the Stokes' (or hydrodynamic) radius of the solvated ion. Stokes' law describes the drag on a sphere in a simple, continuum fluid

42

flow in the limit of negligible inertial effects. The Stokes's radius of an ion can be interpreted as the radius of a sphere with the same viscous drag as the ion. Because of non-continuum effects and the complex interactions between the ion, nearby counterions, and the solvent molecules, the Stokes' radius is only roughly related to other measures of ion dimensions such as the crystallographic radius. Even in the limit of infinite dilution, the Stokes' radius of an ion is therefore an empirically determined quantity which accounts for the non-spherical nature of the ion and the effect of its hydration shell. This quantity is often measured at some reference temperature, θ.

Treatment of limiting ion mobility as a balance between electric force and a drag law from continuum flow theory leads to an approximate relation between mobility and solvent viscosity. For aqueous solutions, we can leverage empirical correlations for water viscosity, η, as a function of temperature, T, as follows:[49]

$$log_{10}\left\{\frac{\mu(T)}{\mu(20°C)}\right\} = \frac{20-T}{T+96}\{1.2378 - 1.303 \times 10^{-3}(20-T)$$

$$(3.2)$$

$$+3.06 \times 10^{-6}(20-T)^2 + 2.55 \times 10^{-8}(20-T)^3\}.$$

This useful correlation covers the temperature range of $-8°C \leq T \leq 150°C$ with an uncertainty of $\pm0.26\%$. Equation (3.1) suggests that a change in the viscosity of the medium will lead to an approximately inversely proportionate change in the limiting mobility of the ion. This leads to the definition of the Walden's rule or Walden's product, $WP_i = \eta\mu_{i,z}^o$.[153] Walden's rule assumes WP_i is independent of temperature for each ion and can be used to correct the limiting mobility of ions, $\mu_{i,z}^o$, evaluated at the reference temperature, θ, as follows:

$$\mu_{i,z}^0(T) = \alpha \mu_{i,z}^0(\theta), \tag{3.3}$$

where $\alpha = \eta(\theta)/\eta(T)$. (We will use "$T$" in parentheses periodically to emphasize the temperature dependence of a variable.) Walden's rule is useful in gaining physical intuition into solvent viscosity effects on limiting ion mobility. However, as we discuss below, application of Walden's rule alone to predict ion mobility can result in severely erroneous mobility predictions at a given operating temperature, T.

3.2.2 Ion solvation effect on limiting ion mobility

As we have mentioned, the idea of a Stokes' radius and Walden's rule in determining limiting ion mobility has only limited use. Quantitatively, the Walden product in Eq. (3.3) is known to vary with temperature, particularly for small ions. This inaccuracy is due to the complexity of ion-solvent interactions which is only approximately captured by a continuum drag law in terms of solvent viscosity. We here present a summary discussion of the physicochemical nature of these interactions and then propose a set of empirical corrections for prediction of limiting ion mobilities for common small ions. We incorporate these empirical corrections in our model. E.R. Nightingale (1959) studied and showed the importance of ion-solvent interactions in the prediction of limiting ion mobility. Nightingale[134] provided empirical data for the Walden product (in water) of varying Stokes radii as a function of temperature. The data show that this temperature dependence is highly specific to ions. The typical trend is for Walden product, *WP*, to decrease with increasing temperature, and the effect is most pronounced for smaller ions such as chloride, potassium, and nitrate. Nightingale qualitatively attributed this effect to the ion-dependent disruption of water structure for

44

ions of varying size and shape. A review of such empirical data for limiting ion mobility and the theory behind solvent-ion interactions was presented by Sadek.[154] Sadek similarly described these phenomena in the context of 'structure making' or 'structure breaking' properties of ions and the solvent. Water possesses quartz-like molecular structure, a tetrahedral coordination, in which each water molecule can participate in two collective hydrogen bonds. This permits the existence of cavities of various sizes. Sadek classified ions into three categories associated with the relative size of the ions versus the size of these cavities in the water structure. These hypotheses propose that the small ions occupy these cavities in the water, and the relative size of the ion and the cavity helps determine the degree of order in the hydration shell around the ion. Stokes' type law is most useful and accurate for ions whose size is relatively large compared to the dimensions of these cavities.

The current theories of ion solvation are useful in providing intuition as to the ion-specific nature of temperature dependence of limiting mobility. However, despite significant work in the field,[154] a theory for quantitative prediction of these effects is not available. Indeed, the physicochemical nature of ion-solvent interactions is not well understood, and considered one of the most difficult problems associated with the study of electrolyte solutions.[154-156] We here therefore take the approach of providing ion-specific empirical corrections for the effect of solvation on limiting ion mobility. To this end, we exploit the clear trend in the data that the smallest ions are subject to the strongest temperature dependence of limiting ion mobility (and *WP*). We formulate this correction in terms of empirical data for temperature dependence of the ion-specific, valence-normalized Walden's product, $WP_i = \lambda_i^o \eta^o / z_i$, expressed in terms of the limiting

conductivity, λ_i^o, for 11 species,[134] where limiting ionic equivalent conductance is defined as $\lambda_i^o = 0.820z/(r_{i,s}\eta^o)$. Here, we define the solvation correction term for ion i as $\beta_i \equiv (\lambda_i^o(T)\eta^o(T))/(\lambda_i^o(\theta)\eta^o(\theta))$, which we use to correct for ion-solvation associated temperature effects on limiting mobility. At the operating temperature, T, we therefore evaluate the limiting mobility as

$$\mu_{i,z}^0(T) = \alpha\beta_i\mu_{i,z}^0(\theta), \tag{3.4}$$

where $\mu_{i,z}^o(\theta)$ is the limiting mobility of an ion measured at the reference temperature, θ, and α accounts for the inversely proportionate change in the limiting mobility of the ion with viscosity. The 11 cases for which we provide the temperature-dependent correction term, β_i include chloride, sodium, potassium, nitrate, lithium, magnesium, perchlorate, rubidium, cesium, calcium, silver, and sulfate. Chloride, potassium, perchlorate, and nitrate particularly exhibit strong temperature dependence and are also common electrolyte ions. Our experimental validation of our model shows that neglecting these ion solvation corrections can result in as much as 20% error in prediction of ion mobilities (e.g., for the case of K+ over a 70°C change).

3.2.3 Ionic strength correction of limiting mobility: actual ion mobility

So far, we have discussed ion mobilities for the case of fully-ionized ions at infinitesimal ionic strength. At finite ionic strength, the presence of an ionic atmosphere around the ion reduces (in all cases) the limiting ion mobility to the so-called actual mobility. There is a wide body of accepted quantitative theory describing these phenomena.[66] Here, we adopt

the extended Onsager-Fuoss model, which is applicable to an arbitrary mixture of species at ionic strengths up to 100 mM,[157] and can be formulated as follows:

$$\mu_{i,z}(T) = \alpha\beta_i\mu_{i,z}^0(\theta) - \left(A\alpha\beta_i\mu_{i,z}^0(\theta) + B\right)\frac{\sqrt{\Gamma}}{1 + \frac{aD}{\sqrt{2}}\sqrt{\Gamma}},$$ (3.5)

where

$$\Gamma = \sum_{i=1}^{s}\sum_{z=n_i}^{p_i} z^2 c_{i,z}.$$

Here, s is the number of species, z_i is the charge number of the i-th ionic species, ε the permittivity of solution, k is the Boltzmann constant, e is the elementary charge, N_{AV} is the Avogadro constant, T is the temperature of the solution and Γ is twice ionic strength, I. The coefficients C_n and the vectors R^n are given by Onsager and Fuoss.[148]

We note our formulation of the extended Onsager-Fuoss differs from previous versions (e.g., as used by Bahga and Santiago[66]) in employing the pre-factors α and β_i to account for temperature effects. Recall, the temperature-dependent term, α, accounts for the inversely proportionate change in the limiting mobility of the ion with viscosity; and β_i, is a modification of Onsager-Fuoss model which we propose here to correct for ion solvation effects.

We use a standard approach to account for the ionic-strength-related reduction in mobility. This reduction can be attributed primarily to two factors. The first is represented by the temperature dependent term, A. This is the so-called relaxation effect which captures the polarization of the ionic atmosphere surrounding the ion, which acts

47

to lower the effective, local electric field experienced by the ion. By definition, the absolute temperature appears in parameter A, which is defined as

$$A = z_i \frac{e^3}{12\pi} \sqrt{\frac{N_{AV}}{(\varepsilon kT)^3}} \sum_{n=0}^{\infty} C_n R_i^n,$$ (3.6)

where ε is the water dielectric constant, whose temperature dependence can be approximated by the following empirical correlation:[103]

$$\varepsilon = 249.21 - 0.79069T + (0.72997 \times 10^{-3})T^2.$$ (3.7)

A depends on temperature as, $1/(\varepsilon T)^{3/2}$, a fairly weak temperature dependence.

The second effect associated with ionic strength reduction of mobility is captured by the parameter B. This is the so-called electrophoretic effect which is associated with the drag force exerted by the moving counter-ion cloud on the central ion. Water viscosity and dielectric constant each impact the magnitude of this drag force, formulated as

$$B = |z_i| \frac{e^2}{6\pi\eta} \sqrt{\frac{N_{AV}}{\varepsilon kT}},$$ (3.8)

which makes B a strong function of temperature.

The aD term in the extended Onsager-Fuoss model takes into account the finite size of ions, where a represents the mean distance of the closest approach for the ions (distance from center of the central ion to the start of the ionic atmosphere).[148, 158] The value assigned to aD is empirically determined, and estimated to lie between 1 and 2 dm$^{3/2}$ mol

$^{1/2}$. For most electrolytes, the recommended approximation for aD is 1.5 dm$^{3/2}$ mol$^{-1/2}$, which we adopt here. D is defined as

$$D = \sqrt{\frac{2e^2 N_{AV}}{\varepsilon kT}},$$

(3.9)

and so has a weak temperature dependence, varying only 2.7% over 60°C change.[149] This change is smaller than the variation among reported values of aD. Therefore, in our model we assume a constant value of 1.5 dm$^{3/2}$ mol$^{-1/2}$ for aD for all temperatures, as recommended by Grenthe and Plyasunov.[149]

3.2.4 Degree of ionization: effective mobility

van't Hoff *($\Delta T < 20$°C):*

The effective (observable) mobility of a weak electrolyte is determined by its degree of ionization. Prediction of effective mobility for weak electrolytes is therefore a function of the acid-base equilibrium of the entire ion mixture. See Persat et al.[159] for a detailed discussion of the effect of ionization on observable mobility. Using the notation of Stěrdý et al.[61, 67] and Bercovici et al.,[67] we can express the total concentration of ionic species i, c_i, as the sum of its constituent ionization states as follows:

$$c_i = \sum_{z=n_i}^{p_i} c_{i,z}.$$

(3.10)

Here $c_{i,z}$ is the concentration of species i of an ionic state with valence z. The limits specify the maximum, p_i, and minimum, n_i, valance values of species i. The activities of

two consecutive ionic states of species i are related by the thermodynamic equilibrium constant $K_{i,z}$ as follows:[66, 160]

$$K_{i,z}(T) = \frac{a_{i,z}a_H}{a_{i,z+1}} = \frac{\gamma_{i,z}\gamma_H}{\gamma_{i,z+1}}\frac{c_{i,z}c_H}{c_{i,z+1}}, \tag{3.11}$$

where c_H is the concentration of H^+ and $\gamma_{i,z}$ is the activity coefficient of the z-th ionic state of species i. Extensive tabulations of thermodynamic data on ionization reactions are available for a large number of acids and bases.[152, 161] A particularly important subset of data belongs to species used as buffers in aqueous solutions. Accurate prediction of their pK, $pK_{i,z}(T) = -\log_{10} K_{i,z}(T)$, at a given operating temperature is critical in applications requiring knowledge and precise control of pH and ionic strength. The thermodynamic equilibrium constant, $K_{i,z}(T)$ is a thermodynamic quantity which depends on the standard free enthalpy, $\Delta H_{i,z}^o$, and entropy, $\Delta S_{i,z}^o$, of ionization of the electrolyte species. This relation can be expressed as follows:

$$pK_{i,z}(T) = \frac{\Delta G_{i,z}^o}{2.303RT} = -\frac{\Delta H_{i,z}^o - T\Delta S_{i,z}^o}{2.303RT}, \tag{3.12}$$

where the coefficient 2.303 arises from the conversion of natural to 10-base logarithm. Over very small temperature differences ($\Delta T < 5°C$), pK dependence on temperature is approximately linear, therefore the empirically determined temperature derivative, dpK/dT (e.g., see Persat et al.,[160] who reported dpK/dT for many common electrolyte species) can be used to predict variations in pK at the operating temperature.

In the case of moderate temperature variations ($5°C < \Delta T < 20°C$), we recommend the use of the simple integrated van't Hoff equation, which assumes that the standard

50

enthalpy change, $\Delta H^o_{i,z}$, and the standard entropy change, $\Delta S^o_{i,z}$, are constant with temperature. Differentiating Eq. (3.12) with respect to temperature, and then integrating from θ to T gives

$$pK_{i,z}(T) = pK_{i,z}(\theta) - \frac{\Delta H^o_{i,z}(\theta)}{2.303R}\left(\frac{1}{\theta} - \frac{1}{T}\right). \tag{3.13}$$

Eq. (3.13) can be used to evaluate $pK_{i,z}$ at the operating temperature, T, provided that we know the $pK_{i,z}(\theta)$ and $\Delta H^o_{i,z}(\theta)$. Goldberg et al.[152] and Christensen et al.[161] have an extensive list for empirically determined thermodynamic properties (including $pK_{i,z}$ and $\Delta H^o_{i,z}$) of ions in aqueous solution (at $\theta = 298.15K$). Our buffer simulation tool (see end of Theory Section) includes a database of $pK_{i,z}(\theta)$ and $\Delta H^o_{i,z}(\theta)$ for over 100 species.

Clarke and Glew relation (T<100°C)*:*

Over wider temperature ranges, we recommend the Clarke and Glew approach,[151] which accounts for the temperature dependence of the standard enthalpy, $\Delta H^o_{i,z}$, and the standard entropy change, $\Delta S^o_{i,z}$, when deriving the representative function for $pK_{i,z}(T)$, from Eq. (3.12). The temperature gradient of $\Delta H^o_{i,z}$ of species i, with valence z,

$$\left(\frac{\partial \Delta H^o_{i,z}}{\partial T}\right)_p = \left(\Delta C^o_p\right)_{i,z}, \tag{3.14}$$

defines another thermodynamic quantity, the change in heat capacity at constant pressure, $\Delta C^o_{p,i,z}$.[162] For many ionization reactions, the temperature dependence of $\Delta S^o_{i,z}$ also

reflects a non-zero $\Delta C_{p,i,z}^o$ associated with such reactions.[162] For a reversible process at constant pressure,

$$\left(\frac{\partial \Delta S_{i,z}^o}{\partial T} \right)_p = \frac{\left(\Delta C_p^o \right)_{i,z}}{T}. \tag{3.15}$$

Assuming that $\Delta H_{i,z}^o(T)$ and $\Delta C_{p,i,z}^o(T)$ are well-behaved functions of T, their value can be properly expressed as perturbations on the tabulated values of $\Delta H_{i,z}^o(\theta)$ and $\Delta C_{p,i,z}^o(\theta)$, respectively, by Taylor's series expansion (see Clarke and Glew[151] for derivation). The dissociation constant, $pK_{i,z}(T)$, can then be expressed at the operating temperature, T, as follows:

$$pK_{i,z}(T) = pK_{i,z}(\theta) - \frac{\Delta H_{i,z}^o(\theta)}{2.303R}\left(\frac{1}{\theta} - \frac{1}{T}\right) - \frac{\Delta C_{p,i,z}^o(\theta)}{2.303R}\left\{\left(\frac{\theta}{T}\right) - 1 + \ln\left(\frac{T}{\theta}\right)\right\}$$

$$- \frac{\theta}{4.606R}\frac{\partial \Delta C_{p,i,z}^o(\theta)}{\partial T}\left\{\left(\frac{T}{\theta}\right) - \left(\frac{\theta}{T}\right) - 2\ln\left(\frac{T}{\theta}\right)\right\}. \tag{3.16}$$

Additional terms involving higher order derivatives of $\partial \Delta C_{p,i,z}^o(\theta)/\partial T$ can be added to the right-hand side of Eq. (3.16).[151] Since the quantity $\partial \Delta C_{p,i,z}^o(\theta)/\partial T$ and its higher derivatives require difficult measurements of the third and higher derivative of $pK_{i,z}(T)$ versus temperature, they are not known for most ionization reactions.[152] However, in our own review of these issues, we found that for operating temperatures typically encountered in electrophoresis and focusing assays (T<100°C), the terms including temperature derivatives of $\Delta C_{p,i,z}^o$ have negligible contributions to $pK_{i,z}(T)$. Our buffer

simulation tool (see end of Theory Section) includes a database of $pK_{i,z}(\theta)$, $\Delta H^o_{i,z}(\theta)$ and $\Delta C^o_{p,i,z}(\theta)$ for 36 common species.

Temperature effects on ionic strength correction of activity coefficients:

For dilute solutions, concentrations can be used in place of chemical activities, a, in Eq. (3.11). However, at significant ionic strengths, the activity coefficients, γ, are smaller than unity, and their ionic strength and temperature dependence must be taken into account. Here we express the apparent thermodynamic equilibrium constant, $\tilde{K}_{i,z}(T)$, which is evaluated from the measured concentrations, Eq. (3.17), as a function of the temperature dependent equilibrium constant, $K_{i,z}(T)$, (Eq. 3.12 or 3.16) and the ionic strength and temperature dependent activity coefficients,

$$\tilde{K}_{i,z}(T) = \frac{\gamma_{i,z+1}}{\gamma_{i,z}\gamma_H} K_{i,z}(T) = \frac{c_{i,z}c_H}{c_{i,z+1}}. \tag{3.17}$$

Our model uses extended Debye-Huckel theory to capture the ionic strength and temperature effects on activity coefficients[150] as follows:

$$\log \gamma_{i,z}(T) = -z^2 \frac{A_{DH}\sqrt{I}}{1 + aD\sqrt{I}} + bz^2 I,$$

$$I = \frac{1}{2}\sum_{i=1}^{s}\sum_{z=n_i}^{p_i} z^2 c_{i,z} \tag{3.18}$$

The first term on the right hand side is the Debye-Huckel term, which accounts for long range, non-specific, electrostatic interactions. The value of A_{DH} at the reference temperature of 25°C, is 0.5012 dm$^{1/2}$ mol$^{-1/2}$ and its temperature dependence is given by

$$A_{DH} = \frac{e^3 N_{Av}^{1/2}}{4\pi\sqrt{2}(\varepsilon kT)^{3/2} \ln 10}.$$
(3.19)

As expected from the $1/(\varepsilon T)^{3/2}$ dependence, the variation of this parameter with temperature is relatively small.[150] Extended Debye-Huckel theory also takes into account contributions from the finite nature of ions in the denominator (see discussion on term aD in Section 2.3). The second term on the right hand side of Eq. (3.18) accounts for specific, short-range, non-electrostatic interactions occurring at high ionic strengths, as approximated by a linear, empirical correction term, b. The value of b at 25°C is 0.1 dm^3 mol^{-1}. b values at temperatures other than 25°C depend on the value adopted for aD.[149] However, the variation of b with temperature, $(db/dT)_p$, is less than 0.005 dm^3 mol^{-1} K^{-1}.[163, 164] The temperature effect of b is therefore very often negligible. For example, in the range 0°C to 50°C, assuming a constant value of b, the error in $\log\gamma_{i,z}/I$ will be less than 0.13 dm^3 mol^{-1}. This corresponds to a small uncertainty in $pK_{i,z}$ of <0.026 at $I = 100$ mM (see Eq. (3.17)). Therefore, in this study, we adopt constant values of 1.5 dm$^{3/2}$ mol$^{-1/2}$ for aD and 0.1 dm^3 mol^{-1} for b for all temperatures.

To evaluate degree of ionization of species i, we use the apparent equilibrium constant, $\widetilde{K}_{i,z}(T)$, which accounts for both, temperature and ionic strength effects, in the electroneutrality condition:[67]

$$\sum_{i=1}^{s} c_i \sum_{z=n_i}^{p_i} z g_{i,z}(T) + c_H - \frac{\widetilde{K}_w(T)}{c_H} = 0,$$
(3.20)

where $g_{i,z}(T) = L_{i,z}(T)c_H^z / \sum_{z=n_i}^{p_i} L_{i,z}(T)c_H^z$ is the dissociation level of the species i, c_i is the total concentration, and $\tilde{K}_w(T) = K_w(T)/\gamma_H(T)\gamma_{OH}(T)$ is the apparent equilibrium constant of water. Outside of the safe[159] pH range (pH of 5 to 9), one must take into account the variation in water equilibrium constant, $K_W(T)$, with temperature to accurately determine the concentration of OH- and H+, and their contribution to conductance. In the current model, we used the water properties $pK_W(\theta)$, $\Delta H_W^o(\theta)$ and $\Delta C_W^o(\theta)$ reported by Olofsson and Hepler.[165] $L_{i,z}(T)$ depends on the apparent equilibrium constants as given by Bercovici et al.:[67]

$$
L_{i,z}(T) = \begin{cases}
\displaystyle\prod_{z'=z}^{-1} \tilde{K}_{i,z'}(T) & z < 0 \\
1 & z = 0 \\
\displaystyle\prod_{z'=0}^{z-1} \tilde{K}_{i,z'}^{-1}(T) & z < 0.
\end{cases}
\tag{3.21}
$$

3.2.5 Solution method for temperature model

Equations (3.5, 3.16, 3.17, 3.18, 3.20 and 3.21) therefore constitute our temperature dependent model for effective mobility including the temperature effects on viscosity, ion solvation, ionic strength correction and degree of ionization. To solve this system, we first solve for the thermodynamic equilibrium constants of each species at the operating temperature using Eq. (3.16), and then we propose an initial guess for c_H. We take as an initial guess simply the solution of the Eq. (3.20) with zero ionic strength, and use this to calculate the ionic concentrations, $c_{i,z}$, activity coefficients, $\gamma_{i,z}(T)$, and apparent equilibrium constants, $\tilde{K}_{i,z}(T)$ as per Eqs. (3.17, 3.18 and 3.21). Then, Eq.

(3.20) is solved repeatedly for $c_{i,z}$ by Newton iteration, until the solution for c_H converges to a value within a predefined tolerance. Similar solution methods were adopted by Bercovici et al.[67] and Bahga et al.[66]

The ionic strength obtained through this process is then used to calculate the fully ionized actual mobility, $\mu_{i,z}(T)$, of every ionic species at the operating temperature, T, using our version of extended (and modified) Onsager–Fuoss expression, Eq (3.5), which accounts for viscosity, ion solvation, and ionic strength effects with temperature. This actual mobility of species i is then corrected to the effective mobility, as given by

$$\mu_i(T) = \sum_{z=n_i}^{p_i} \mu_{i,z}(T)\, g_{i,z}(T),$$

(3.22)

using the temperature dependent dissociation factor, $g_{i,z}(T)$.[67]

3.2.6 Quantifying the aggregate effect of temperature dependences unrelated to viscosity

In this study, we address all major physical phenomena associated with the temperature dependence of electrolyte mobility in water. The easiest, most common, and often most pronounced effect to take into account is the temperature dependence of viscosity of water. We introduce factor f, which normalizes the electrolyte solution conductance by the change associated with variations in viscosity as follows:

$$f = \frac{\sigma(\theta)\eta(\theta)}{\sigma(T)\eta(T)}$$

(3.23)

Here, conductivity, σ, is defined as

$$\sigma(T) = \sum_{i=1}^{s} c_i \sum_{z=n_i}^{p_i} F z_i \mu_{i,z}(T) \, g_{i,z}(T).\tag{3.24}$$

f therefore quantifies the aggregate effect of all phenomena other than simple changes in solvent viscosity. Namely, f describes the net effect on conductivity due to temperature-dependent changes in degree of ionization, ion solvation, and ionic strength corrections. An ideal ion which follows Walden's rule exactly has an f value of unity $(\log_{10} f = 0)$. The sign of $\log_{10} f$ indicates if these effects act in concert with or against the influence of viscosity on electrolyte solution conductivity (these effects oppose the influence of viscosity on buffer conductivity with positive $\log_{10} f$). This useful parameter and its application were first proposed by Ross and Locascio[131] in 2002 and is relevant for many electrophoresis effects including joule heating, dispersion, and voltage versus current requirements.

3.2.7 Stand-alone simulation tool for temperature-dependent electrolyte properties

We developed a MATLAB (R2012b Mathworks, Natick, MA) based simulation tool for electrolyte solutions which incorporates our comprehensive temperature model. This simulation tool inputs mobilities and thermophysical data and calculates system pH, system conductivity, and effective mobilities for arbitrary mixtures of strong or weak electrolytes. The electrophoretic mobilities of all analytes presented in this study (except water ions) were obtained from Hirokawa et al.[166] The ionization dissociation constants, $pK_{i,z}(\theta)$, standard molar enthalpy change, $\Delta H_{i,z}^{o}(\theta)$, and standard molar heat capacity change, $\Delta C_{p,i,z}^{o}(\theta)$, of each species were obtained from Goldberg at al.[152] (see **Table 3.2**).

We also offer an extended list of analytes with their chemical properties built into a graphical user interface of the Matlab script. When available, we list all four of the chemical properties. However, for the some ionic species, data on $\Delta C^o_{p,i,z}(\theta)$ is not available, in which case, we list only the mobility, $\mu_{i,z}(\theta)$,[166] $pK_{i,z}(\theta)$,[161] and $\Delta H^o_{i,z}(\theta)$.[161] Our code, which we named Simulation of Temperature Effects on ElectroPhoresis (STEEP), is available for free on our website at http://microfluidics.stanford.edu/download/index.html. We include source code, a data base of thermophysical data, and instructions for use.

Table 3.2. List of chemical species mobility, μ, (in $10^9\,\mathrm{m^2V^{-1}s^{-1}}$), p$K$, standard free enthalpy of ionization,$\Delta\mathrm{H}^\circ$, (in J mol^{-1}) standard free specific heat of ionization,$\Delta\mathrm{C_p}^\circ$, (in J K^{-1} mol^{-1}) values defined at 25°C, as used in main paper.

Name	μ(-3)	μ(-2)	μ(-1)	μ(+1)	pK(-3)	pK(-2)	pK(-1)	pK(+1)	ΔH°(-3)	ΔH°(-2)	ΔH°(-1)	ΔH°(+1)	ΔC$_p$°(-3)	ΔC$_p$°(-2)	ΔC$_p$°(-1)	ΔC$_p$°(+1)
ACETIC ACID			42.4				4.756				-410				-142	
BORIC ACID			36.5				9.237				13800				-240	
CITRIC ACID	74.4	54.7	28.7		6.396	4.761	3.128		-3380	2230	4070		-254	-178	-131	
HEPES			23.5				7.564				20400				47	
HYDROCHLORIC ACID			79.1				-2				0				0	
MOPS			26.9				7.184				21100				25	
PHOSPHORIC ACID	71.5	61.4	34.6		12.35	7.198	2.148		16000	3600	-8000		-242	-230	-141	
BISTRIS				26				6.484			28400				27	
ETHANOLAMINE				44.3				9.498				50520				26
HISTIDINE			28.3	28.8			9.34	6.07			43800	29500			-233	176
POTASSIUM				76.2				13				0				0
SODIUM				51.9				13.7				0				0
TRIS				29.5				8.072				47450				-59

59

3.3 Materials and Methods

To experimentally validate our model, we explored temperature effects on buffer conductivity and pH as these are the most generally applicable consequences of the model. As we shall see, these measurements can be used to illustrate each of the effects we model, including degree of ionization and ion solvation. We note that mobilities of individual analytes can be most strongly affected by temperature, but individual analyte mobilities are typically ad hoc and useful to a specific application. We further discuss examples of analyte mobility prediction in the Supporting Information. For example, in Section S-5 we discuss a case where the temperature trends of three background buffers determine whether the mobility of a single analyte increases dramatically, decreases, or stays approximately the same with increasing temperature. In Section S-6 we given an example of how three analytes can have very distinct temperature trends in a single background buffer.

We chose to summarize our experimental validation using the four two-component electrolyte solutions shown in **Table 3.4**. (In **Table 3.5**, we provide list of six additional solutions we analyzed experimentally in our study.) In each case, we prepared three replicates of each electrolyte solution in a 50 mL Erlenmeyer flasks. We placed each sample on a magnetic stirrer and hot plate (Fisher Scientific, Isotemp). We inserted a carbon conductivity probe (Corning Model 541P) into the flask, and sealed it with parafilm to minimize the effects of evaporation on the ion concentrations. The conductivity and temperature were measured during both heating and cooling between 25°C to 70°C in approximately 5°C increments using a Corning Pinnacle 542 conductivity meter. We calibrated the conductivity probe prior to each measurement set

60

using conductivity standards purchased from Ricca Chemical Company. Using the system's Pinnacle "3 in 1" Premium Gel Combo electrode, we also measured the pH of each electrolyte solution at 25°C and 70°C. Data obtained during either heating or cooling track each other closely, consistent with negligible hysteresis effects in our method.

3.4 Results and discussion

3.4.1 Predictions of effective mobility, conductivity, and pH

To demonstrate our model, we selected three example buffers which demonstrate the phenomena discussed in Theory. Figures 1-3 show plots of the effective mobility of the titrating anion for temperatures from 20°C to 80°C, with respect to its effective mobility at the reference temperature, $\theta = 25°C$, as follows: $\mu\_(T)/\mu\_(\theta)$ (the subscript indicates an anion). The curves associated with our full temperature model (including all effects considered here) are labeled "Current". In the upper insets of Figures 1-3, we show predictions of the full temperature model for the anion and cation pKs and electrolyte solution pH as functions of temperature. In the lower insets, we show plots of ionic strength, I, and normalized electrolyte solution conductance, f, as functions of temperature.

The main plots of **Figure 3.1-3.3** also include four additional curves which we use to demonstrate the effect of individual physical phenomena described in Theory. These curves represent incomplete versions of our model, and are described in **Table 3.3**. All curves correct for changes in water viscosity. The simplest model, 'W', uses only the Walden's viscosity correction term, α, to evaluate effective mobility at elevated

temperature. Model 'SSC' captures the temperature dependence of limiting ionic mobility due to changes in solvation, but disregards changes in degree of ionization and the temperature sensitivity of ionic strength corrections. Model 'ISC' quantifies the temperature dependence of the extended Onsager-Fuoss and the extended Debye-Huckel theory, but the degree of ionization and the ion solvation correction terms are to always equal the value at room temperature. Model 'pKC', captures the temperature effects on degree of ionization, but assumes that ion solvation and the ionic strength correction terms are always equal to the value at room temperature.

Table 3.3 Summary of full model (labeled "Current" in Figures 1-3) and limiting models used for comparing the various sources of temperature effects on effective ionic mobility. The values $\mu_{i,z}(\theta)$ and $\mu_{i,z}(T)$ are evaluated using Eq (3.22). $g_{i,z}(\theta)$, and $g_{i,z}(T)$ are evaluated using Eq (3.20). The assumptions made for the limiting models include temperature insensitivity of ion solvation, $(\beta_i = 1)$, temperature-independent degree of ionization ($dpK/dT = 0$), and temperature independent ionic strength corrections ("$IS\ corr. \neq f(T)$"). T is the operating temperature and θ is the reference temperature (25°C).

	Effective mobility at operating temperature, *T*	Assumptions
Current	$\mu_i(T) = \sum_{z=n_i}^{p_i} \mu_{i,z}(T)\, g_{i,z}(T)$	
W	$\mu_i(T) = \alpha \sum_{z=n_i}^{p_i} \mu_{i,z}(\theta)\, g_{i,z}(\theta)$	$\beta_i = 1$ $dpK/dT = 0$ $IS\ corr. \neq f(T)$
SSC	$\mu_i(T) = \alpha\beta_i \sum_{z=n_i}^{p_i} \mu_{i,z}(\theta)\, g_{i,z}(\theta)$	$dpK/dT = 0$ $IS\ corr. \neq f(T)$
ISC	$\mu_i(T) = \sum_{z=n_i}^{p_i} \mu_{i,z}(T)\, g_{i,z}(T)$	$\beta_i = 1$ $dpK/dT = 0$
pKC	$\mu_i(T) = \dfrac{\sum_{z=n_i}^{p_i} \mu_{i,z}(\theta)\, g_{i,z}(\theta)}{\left(\sum_{z=n_i}^{p_i} \mu_{i,z}(\theta)\, g_{i,z}(\theta)\right)_{(I=0)}} \sum_{z=n_i}^{p_i} \left(\mu_{i,z}(T) g_{i,z}(T)\right)_{(I=0)}$	$\beta_i = 1$ $IS\ corr. \neq f(T)$

Figure 3.1 shows predictions for a simple, two-component buffer consisting of a univalent weak electrolyte, 200 mM Tris, and a univalent, strong titrant anion donated by 100 mM HCl (pH = 8.18 at $\theta = 25°C$). The main plot shows Cl⁻ mobility normalized by its value at the reference temperature, θ. The anion mobility increases monotonically from 20°C to 80°C. We see that the comparison curves W, ISC, and pKC each overpredict anion mobility by about the same amount, while the SSC model matches the prediction quite closely. Here, the water viscosity has the most prominent influence on the effective mobility of the chloride ion. The most dominant, non-viscous related effect is due to changes in the solvation of Cl⁻. The Stokes radius of Cl⁻ increases with temperature resulting in reduction of its absolute electrophoretic mobility. The top inset plot shows that the buffer pH tracks closely the pK of the buffering Tris, as expected, since the titrant ion Cl⁻ is donated by a strong acid so the ionization of Tris is independent of pH. For the same reason, the ionic strength of the solution (lower inset) is constant (since dissociation of Tris is determined by the concentration of the pH-insensitive Cl⁻). The slight overprediction by the SSC model is associated with a mild temperature sensitivity of the Onsager-Fuoss correction. Overall, we note that simple buffers consisting of a weak electrolyte titrated with a strongly ionized (titrant) ion typically have uniform ionic strength but have a pH change with temperature dictated by the p$K(T)$ function of the weak electrolyte.
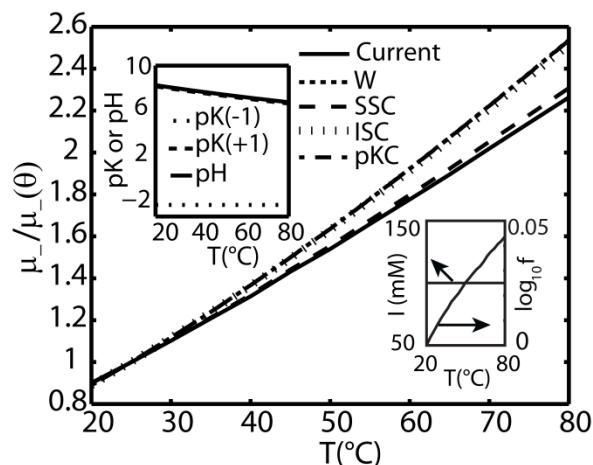
Figure 3.1. Predicted electrophoretic mobility of Cl- in solution containing 200 mM Tris and 100 mM HCl as a function of temperature. The pH of this simple buffer tracks closely temperature dependent value of pK as expected. However, the degree of Tris ionization is determined by the chloride ion whose molar density is insensitive to pH. Therefore, this electrolyte system maintains constant ionic strength with temperature. The simple 'SSC' model is fairly accurate here which suggest that the source of the non-viscosity related temperature dependence is due to the change in the hydration shell of the chloride ion.

Figure 3.2 shows a more interesting case of a two component, weak-electrolyte buffer composed of 20 mM ethanolamine (pK = 9.498) and 20 mM boric acid (pK = 9.237). Here, the model predicts a shallow, roughly parabolic anion mobility curve with a local maximum near T = 60°C. We see the comparison curves W, SSC, and ISC all track each other closely but grossly overpredict the rise in conductivity. Model pKC matches well with the comprehensive model (Current), suggesting that the temperature-induced decrease in degree of ionization is primarily the source of the observed mobility behavior. This conclusion is supported by the pK and pH trends shown in the upper inset, which show that the temperature dependence of ethanolamine pK is much stronger than that of borate. As temperature is increased, the buffer pH therefore decreases faster than the pK of borate. The anion and cation pKs are each, at room temperature, close to and bound the solution pH. The dominant effect of temperature on the ethanolamine pK causes a steep

64

drop in pH. This decreases the ionization of borate ion, thereby decreasing its effective mobility. The associated drop in the ionic strength (bottom inset), I, also influences the effective mobility by decreasing the magnitude of the Onsager-Fuoss correction (which explains the slight underprediction of pKC model from Current). Again, the large, positive value for $\log_{10}f$ (up to $\log_{10}f = 0.33$ or $f = 2.2$ at $T = 80°C$) shows how these effects act together to strongly compensate for the decrease in water viscosity. These predictions show a discrepancy between the full model and of the Walden model by as much as 116% for the anion mobility.
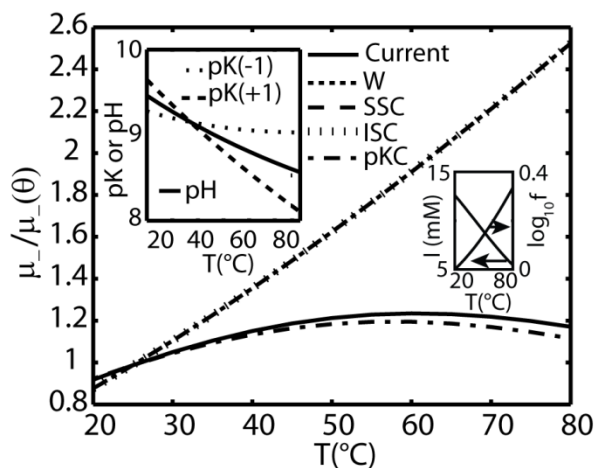
Figure 3.2. Predicted electrophoretic mobility versus temperature of boric acid anion (borate) in solution containing 20 mM ethanolamine and 20 mM boric acid. Increase in temperature results in strong drop in pK of ethanolamine and a moderate drop in the pK of boric acid, resulting in an overall decrease in pH (top inset). Here, the most prominent contribution to both anion mobility and ionic strength, I (bottom inset) is due to the sharp decrease in degree of ionization of boric acid (hence the proximity of 'pKC' model to 'Current'). The large, positive value of $\log_{10} f$ (bottom inset) shows how this effect opposes contributions from the decreasing viscosity to conductivity. Ultimately, these opposing effects are also reflected by the shallow mobility curve (main plot). Predictions based on Walden's rule here overestimate the anion mobility by 116% (and buffer conductivity by 106%).

Figure 3.3 shows an electrolyte solution composed of 200 mM Bis-tris (pK = 6.484) and 50 mM citric acid (pK_{-3} = 6.396, pK_{-2} = 4.761, pK_{-1} = 3.128). At room temperature, the pH is ~6.2, so for simplicity, we only plot the pK of its tri-valent anion (citrate). Here again the model predicts that citrate mobility increases monotonically from 20°C to 80°C temperature range. The comparison curves ISC and pKC underpredict the rise in mobility, while curves W and SSC overpredict it slightly. The top inset shows that the pK of citrate increases moderately while the pK of Bis-tris drops sharply with increasing temperature, resulting in a 0.6 pH unit drop over the temperature range.
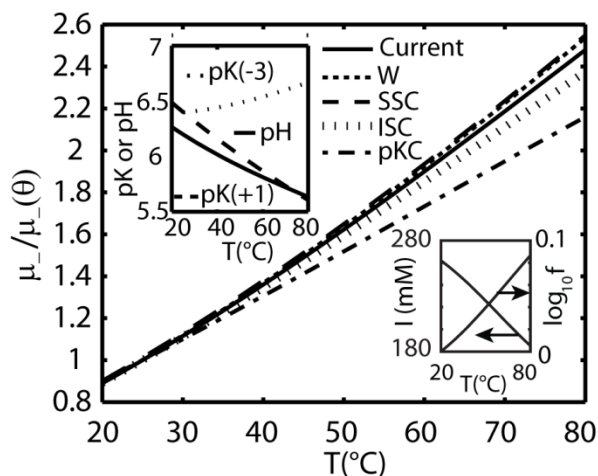
Figure 3.3 Predicted electrophoretic mobility of a trivalent ion, citrate, in a solution containing 200 mM Bis-tris and 50 mM citric acid. For simplicity we show only the pK of the trivalent anion of citric acid (citrate ion, $z = -3$). Increase in temperature results in a strong drop in pK of Bis-tris and a mild increase in the pK of citrate ion, resulting in an overall reduction in pH (top inset). The sharp decrease in the degree of ionization of the citrate ion contributes strongly to the decrease in ionic strength (bottom inset), which would suggest a considerable effect on its effective mobility (see limiting model 'pKC'). However, the ion's multivalent nature makes citrate extremely sensitivity to changes in the ionic strength. Therefore, the temperature-induced reduction in ionic strength is accompanied by a reduction in the magnitude of the Onsager-Fuoss correction term. The two effects offset each other and so the net effects are well approximated by the Walden model (which nearly exactly overlies the Current model).

The decrease in pH results in an overall strong decrease in ionic strength by promoting reassociation of the citrate ion with hydrogen. However, the effective mobility of the trivalent citrate is only mildly reduced, because a decrease in ionic strength also strongly attenuates ionic strength effects on mobility. Interestingly, in this system including a multivalent electrolyte, the two effects ($pK(T)$ affecting dissociation and ionic strength on mobility) largely offset each other.

3.4.2 Additional electrolyte examples

Here we include additional curves which we use to demonstrate the effect of individual physical phenomena described in the **Table 3.4**. For clarity, if one of the physical phenomena has no temperature contribution to mobility (other than a Walden type behavior), and its corresponding limiting model overlaps with model 'W'; we chose not to plot the curve. **Figure 3.4** shows predictions for the second electrolyte in Table 3, which is composed of 50 mM potassium citrate ($pK_{-3} = 6.396$, $pK_{-2} = 4.761$, $pK_{-1} = 3.128$) mixed with 200 mM Bis-tris ($pK = 6.484$). Citric acid is trivalent and is therefore very sensitive to ionic strength effects. Further, potassium is a small ion whose hydration changes with temperature. We also added weak Bis-tris to increase the pH. We chose this solution as a large difference between the pH and citrate pKs ensures that citrate remains fully ionized for all temperatures. This enables the isolation of two temperature related phenomena: ionic strength effects on citrate ion mobility (right plot) and ion solvation effect on the potassium ion mobility (left plot). Note that, since pH > $pK_{\text{Bis-tris}}$ - 2, Bis-tris is practically neutral and has virtually zero effective mobility. Bis-tris therefore has negligible contribution to solution ionic strength and conductivity. This solution is an

interesting example of ionic strength and solvation effects, but it is a poor buffer with buffering capacity of only ~0.6 mM.
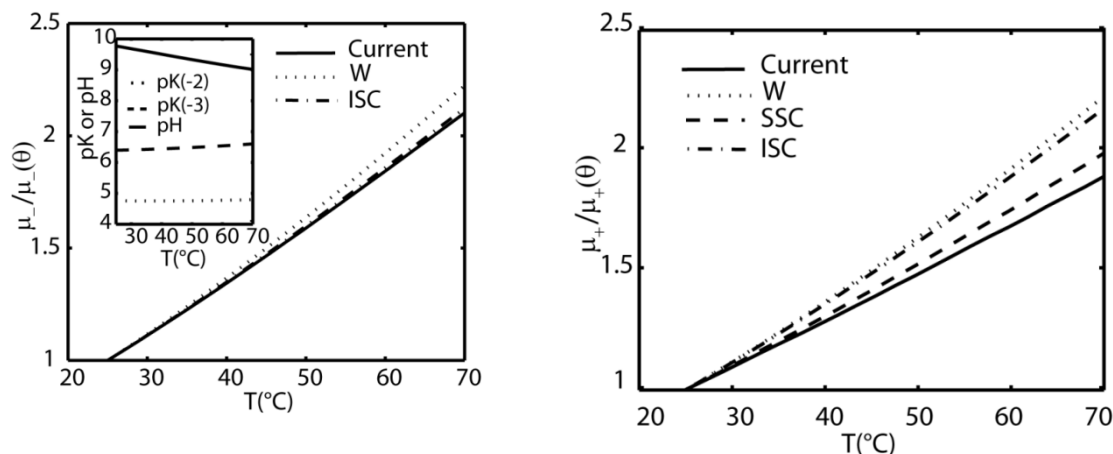
Figure 3.4 Prediction of anionic (citrate) and cationic (potassium) mobilites in an electrolyte solution composed of 50 mM potassium citrate ($pK_{-3} = 6.396$, $pK_{-2} = 4.761$, $pK_{-1} = 3.128$) mixed with 200 mM Bis-tris ($pK = 6.484$) (Solution 2, in Table 3 of paper). Left plot shows the predicted electrophoretic mobility of a trivalent ion, citrate. In the inset, we show only the pK of the trivalent and divalent anion of citric acid, which lie far from the solution pH, indicating no change in degree of ionization. Thus we can attribute the change in the effective mobility of citrate to temperature variation of ionic strength correction terms. Right plot shows the predicted electrophoretic mobility of a monovalent cation, potassium. The simple 'SSC' model is fairly accurate here which suggest that the dominant source of the non-viscosity related temperature dependence is due to the change in the hydration shell of the potassium ion. The residual deviation of 'SSC' from the 'Current' solution is due to the temperature dependence of ionic strength correction, captured by 'ISC'. Limiting models 'SSC' and 'pKC' (and 'pKC' on the left plot) are not plotted as they nearly perfectly overlap the W curve.

     Figure 3.5 shows a weak-electrolyte buffer composed of 30 mM Tris and 30 mM HEPES (the third solution in Table 3). Here, the model predicts a shallow, linear anionic mobility curve. Limiting model pKC matches well with the comprehensive model (Current), suggesting that the temperature induced decrease in degree of ionization is the primarily the source of the observed mobility behavior. This conclusion is supported by the pK and pH trend shown in upper inset which show that the temperature dependence

68

of Tris pK is much stronger than that of HEPES. At room temperature, the anion and cation pKs are close to and bound the solution pH. As temperature is increased, the buffer pH decreases faster than the pK of HEPES. This decreases the ionization of HEPES ion, thereby decreasing its effective mobility.
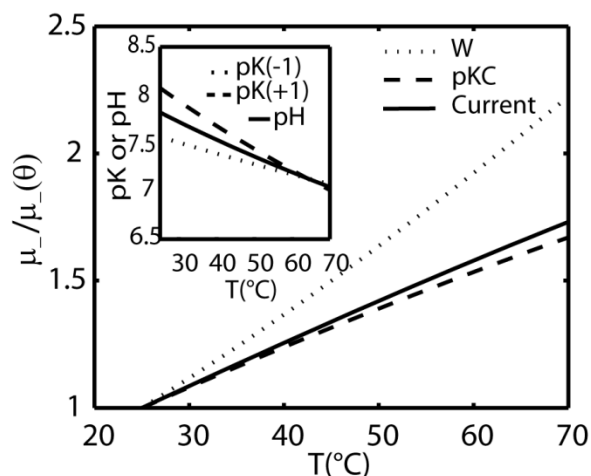
Figure 3.5 Predicted electrophoretic mobility versus temperature for HEPES (anion) in the solution of 30 mM Tris and 30 mM HEPES (Solution 3, in Table 3 of main paper). Increase in temperature results in a strong drop in the pK of Tris and a moderate drop in the pK of HEPES, resulting in an overall decrease in pH (inset). Here, the most prominent contribution to anion mobility is due to the sharp reduction in degree of ionization of HEPES (hence the proximity of 'pKC' model to 'Current'). Predictions based on Walden rule here overestimate the anion mobility by 30% at 70°C. Limiting models 'SSC' and 'ISC' are not plotted as they nearly perfectly overlap the W curve.

Figure 3.6 shows a weak-electrolyte buffer composed of 30 mM Tris and 15 mM acetic acid (Solution 4 in **Table 3.4**). Here, the comprehensive model (Current) tracks model 'W' closely, suggesting temperature effects on ion solvation, ionic strength correction, and degree of ionization are insignificant. The latter conclusion is supported by the pK and pH trend shown in upper inset of **Figure 3.6**. Tris is included at twice the concentration of acetic acid, so the solution pH is dominated the p$K(T)$ function of Tris. The large difference (>2 units for all temperatures) between the acetate pK and solution

pH ensures the acetate remains fully ionized for all temperatures. In this electrolyte solution, the mobility of acetate can be estimated by correcting for changes in viscosity of water alone.
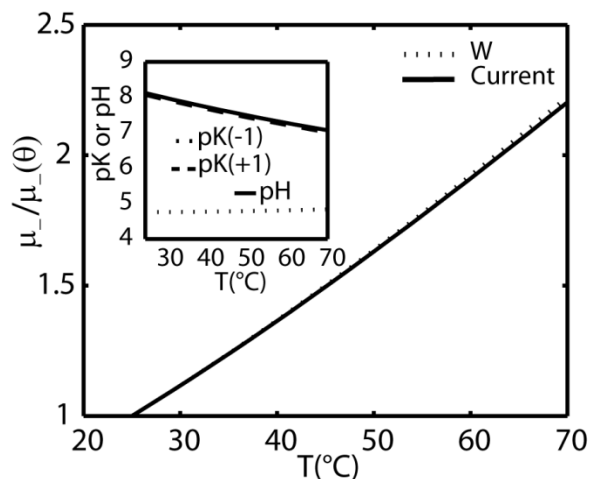
Figure 3.6 Predicted electrophoretic mobility versus temperature of acetate (anion) in a solution containing 30 mM Tris and 15 mM acetic acid (Solution 4, in **Table 3.3**). Here, ionic strength of solution containing cation (Tris) and titrant (acetic acid) are determined by the molarity of the fully-ionized acetic acid. While the pH varies with temperature dictated by the p$K(T)$ function of the Tris, the large difference (>2 units for all T) between acetate pK and solution pH ensures that acetic acid remains fully ionized. Therefore, the acetate mobility predictions based on Walden's rule estimate anion mobility fairly accurately, within ~4%. Limiting models 'SSC', 'ISC', and 'pKC' are not plotted as they nearly perfectly overlap the W curve.

3.4.3 Temperature model validation

We validated our model using conductivity and pH measurements in the temperature range of 25°C to 70°C for the two-component electrolyte solutions listed in **Table 3.4**. For convenience of presentation, we present the data in terms of the *f* factor, which quantifies temperature dependence that is not attributed to variations in water viscosity (see Theory). Presentation of the experimental data in terms of *f* therefore also offers a direct comparison with the commonly applied Walden's rule. We also plot the

conductivity for each temperature, T, with respect to conductivity evaluated at the reference temperature, θ, as follows: $\sigma(T)/\sigma(\theta)$, where $\theta = 25°C$.

The data of Figure 4 is a compact summary of our conductivity measurements and model validation. As mentioned earlier, we prepared three replicates for each chemistry and measured electrolyte solution conductivity as a function of temperature from $T = 25°C$ to $70°C$. Shown in **Figure 3.7** are the raw data for all runs.
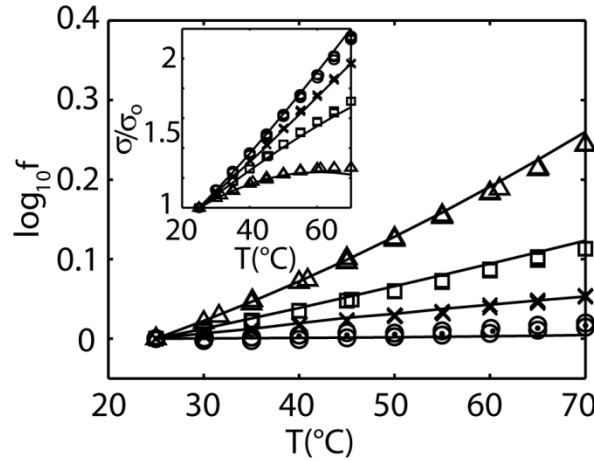
Figure 3.7 Experimental validation of the temperature model. Shown are theory curves along with respective conductivity (σ) measurements (raw data). The measurements are three realizations per condition (symbols clustered at each temperature) for the following electrolyte solutions: 20mM ethanolamine & 20mM boric acid ($\triangle$); 200 mM Bis-tris & 50 mM citric acid ($\times$); 30 mM Tris & 15 mM HEPES ($\square$); and 30mM Tris & 15 mM acetic acid ($\circ$). The factor f is defined as $\sigma(\theta)\eta(\theta)/(\sigma(T)\eta(T))$, where $\theta = 25°C$, and η is dynamic viscosity. For the ethanolamine buffer, Walden's rule prediction for σ at 70°C would result in 75% error.

The data points cluster into groups of three since exactly revisiting each temperature value was difficult across buffer runs given our measurement method. In many cases, the three measurements overlap enough such that they are approximately indistinguishable—showing the high degree of reproducibility across replicate experiments. For all cases, we

also decreased temperature from $T = 70°C$ down to $T = 25°C$ and measured conductivity at 5°C increments (not shown here) to ensure our experiment showed no hysteresis effects (e.g., due to unwanted evaporation of water during the run). None of the data demonstrated a dependence on the sign of temperature increase. Shown together with the raw data are predictions from the 'Current', full temperature model (solid curve).

In Fig. 4, the solution of ethanolamine and boric acid (parabola) shows conductivity which is concave down and parabolic similar to the predicted anion mobility curve shown in Fig. 2. The conductivity increases by a maximum of only 25%, due to the steep decline of ionization of both borate and ethanolamine ions (c.f **Figure 3.2** for more details). The solutions Bis-tris-potassium citrate and Tris-hepes also show increases in conductivity, but with shallower slopes, and associated higher values of $\log_{10} f$. The Bis-tris and potassium citrate conductivity changes are influenced mostly by the change in solvation of the potassium ion and by the temperature dependence of the ionic strength corrections (citrate is trivalent and therefore its mobility is very sensitive to ionic strength, see Fig. S-1). The conductivity dependence of Tris-hepes is dominated by the change in degree of ionization of its constituent weak electrolyte ions (see **Figure 3.5** for more details). The conductivity increases by 70% for Tris-hepes and by 100% for Bis-tris and potassium citrate (from $T = 25°C$ to $T = 70°C$). The electrolyte mixture of Tris and acetic acid has the strongest temperature dependence. We see that this buffer also shows the smallest and nearly constant values of $\log_{10} f$, suggesting that this buffer's temperature dependence is mostly due to the Walden type dependence (**Figure 3.6**). In all four electrolyte solutions, the highlighted effects oppose the influence of viscosity (Walden) on conductivity (positive $\log_{10} f$). At $T = 70°C$, Walden's rule would yield the following

errors in prediction of our measured conductivity values: 75%, 13%, 30%, and 4% for the solutions in **Table 3.4**, respectively.

Table 3.4 Experimental validation of the temperature model for electrolyte solution pH at 25°C and 70°C. Uncertainty values indicate 95% confidence on the mean.

Electrolyte Solution		pH (T = 25°C)		pH (T = 70°C)	
		Data	**Theory**	**Data**	**Theory**
20 mM boric acid	20 mM ethanolamine	9.37±0.09	9.37	8.63±0.09	8.68
50 mM potassium citrate	200 mM Bis-tris	9.6±0.3	9.73	8.9±0.1	9.01
30 mM HEPES	30 mM Tris	7.82±0.02	7.82	7.0±0.1	7.04
15 mM acetic acid	30 mM Tris	8.1±0.1	8.12	7.04±0.04	7.07

For all temperatures, our electrolyte simulation tool was able to accurately predict conductivity and pH within 10% and ~ 0.1 pH units, respectively. We attribute a large fraction the discrepancy between data and prediction to small errors in pipetting and dilution. For example, at room temperature, the conductivity predictions for some electrolyte solutions were off by as much as 6%. If we correct our conductivity data to account for this offset at room temperature, then our conductivity prediction is within approximately 4% for all temperatures (20°C to about 70°C).

We measured the temperature dependence of conductivity and pH in detail for ten electrolyte solutions, and we summarize measurements associated with the additional six solutions in **Table 3.5**. The latter additional solutions include sodium phosphate, Tris-HCl, Bis-tris-MOPS, sodium phosphate, histidine-acetate, and Tris-borate buffers. With

the sole exception of Tris-borate buffers, the conductivity and pH predictions agreed to measured values within 4% and 0.2 pH units or better. These data suggest the model can accurately predict the temperature dependence of electrolyte solution conductivity for all the electrolyte solution explored, again with the exception of Tris-boric acid. Interestingly we are able to well predict the behavior of Tris and of boric acid when these species are paired with other ions we explored. However, the particular combination of Tris and boric acid consistently showed large discrepancies between model and measurements of conductivity and pH (respectively, 17 to 68% and as much as 0.32 pH units). We hypothesize that Tris and boric acid ions may undergo non-acid/base reactions with each other (see Supplementary Information). This hypothesis is strongly supported by the work of Michov,[167] which showed that Tris-borate buffers contain a cyclic complex compound of betainic structure, and a buffer with both of these ions therefore does not obey the Henderson-Hasselbalch equation.

Table 3.5 Summary of predictions and measurements of pH and conductivity for six additional electrolyte solutions at temperatures 25°C and 70°C.

Composition		pH (T=25°C)				pH (T=70°C)			
		pH_{exp}	pH_{th}	σ_{exp} (μS/cm)	σ_{th} (μS/cm)	pH_{exp}	pH_{th}	σ_{exp} (μS/cm)	σ_{th} (μS/cm)
30 mM Bis-tris	30 mM MOPS	6.75	6.83	466	444	6.19	6.25	945	868
30 mM NaOH	20 mM phosphoric acid	7.22	6.98	2620	2463	7.21	6.99	5780	5358
20 mM L-histidine	20 mM acetic acid	5.34	5.41	1017	1013	5.03	5.07	1795	1796
200 mM Tris	100 mM HCL	8.19	8.15	4470	4527	7.12	7.10	8970	9378
10 mM Tris	10 mM boric acid	8.55	8.65	115	131	7.82	8.00	142	118
100 mM Tris	100 mM boric acid	8.31	8.65	749	1258	7.68	8.00	1414	1161

74

4 Particle Tracking and Multispectral Collocation Method for Cytometry-Like and Particle-to-Particle Binding Assays

The contents of this chapter are under review in Analytical Chemistry. They are reproduced here with minor modifications.

4.1 Introduction

Accompanying the growing number of particle, cell, and bead-based assay applications,[86, 168-172] particle and cell analysis methods have become more rigorous and sophisticated.[173, 174] The two most frequently cited techniques are likely flow-cytometry (FCM)[174, 175] and laser-scanning cytometry (LSC).[176] Flow cytometry is a workhorse technology used routinely in immunology,[177] pathology[178] and hemotology.[179] FCM performs a single high content multiparametric measurement for thousands of particles in minutes or less. (Here we shall use "particles" to denote micron-scale beads and/or living cells.) The core of a standard cytometer is a flow chamber where a particle-laden stream is hydrodynamically focused with the aid of sheath flow into a small interrogation region through which particles traverse one at a time. Multicolor lasers illuminate particles in the interrogation region. Forward scatter is approximately correlated to the size of the particle and side scatter provides an indication of particle granularity.[175] Increasing need for multiplexing via polychromatic excitation and emission has pushed the frontiers of flow cytometry, and enabled, for example, implementation of instruments that measure up to 19 parameters (17 fluorescent colors and 2 physical parameters).[177]

Laser-Scanning Cytometry (LSC)[176] was originally designed to provide an imaging complement to traditional FCM and allow morphological analysis of adherent cells.[180] LSC scans stationary particles (typically cells) adhered to a surface and its implementation has evolved to include analyses of cell proliferation, tissue architecture, and immunophenotyping using precious samples.[169] The cells are fixed onto slides and scanned with multiple lasers. This can be repeated over time for studies of enzyme kinetics and other time-resolved processes. The slide can be removed from the instrument in order to change staining or otherwise modify the cells; and it can then be placed back on the instrument for re-analysis.[180] Each cell can be relocated and all of the data points can be correlated for multivariate analysis.

There is a range of other multicolor particle image counting and analysis systems. For example, recently the field has seen development of imaging versions of FCM systems wherein point detectors are replaced by high speed imaging to analyze particle morphology in more detail and using up to 12 wavelengths (e.g., the Amnis Imagestream system). These systems employ time delay integration (TDI) wherein the camera is panned electronically to track the cells in the flow stream. These systems track cell velocities and use this to time the shift of photoelectrons on the CCD chip. These systems can produce up to 12 simultaneous realizations of a darkfield, two brightfield images, and nine fluorescence images of each particle in suspension.

Both FCM-type and LSC-type particle analysis techniques have fairly complex and expensive instrumentation. As of the time of this writing, fluorescence flow cytometers start at $50,000 (two-laser configuration BD Accuri C6) and easily range up to $500,000 for units with multi-wavelength capability.[168] Similarly, LSC instruments use

laser sources, precision scanning optics, and PMT detectors in systems with the same order of magnitude price as FCM. Furthermore, these systems often require annual maintenance contracts and highly trained operators to obtain and process data. Interestingly, as pointed out by Shapiro,[168] FCM and LSC are each overkill for most cell identification applications as most cytometry assays are based on measurements of emitted cell fluorescence at most four colors,[173] and do not require highly complex multiparametric fluorescence, or morphological information.[168] A notable example application of cytometers is the two-[181] and three-color[173] immunophenotyping of T cells of HIV-infected patients for monitoring progression and treatment of HIV/AIDS. FCM and LSC systems each require specialized particle handling systems: precise hydrodynamic focusing for FCM and immobilization and scanning for LSC. Neither method is applicable to randomly distributed (in three dimensions) particles flowing in a channel.

In brief, there is much interest and active work in multispectral particle analysis, including cytometry-like counting. Also, the cost of these systems can be prohibitive for some settings and applications, and may be unwarranted for many applications. In this work we present a low-component-cost and simple-to-implement alternative technology for multispectral particle enumeration, image analysis, collocation and quantitation of particle-to-particle interactions. We compare the features and capabilities of the current method with typical characteristics of FCM and LSC in **Table 4.1**.

Our method is applicable for either single images or time-resolved images of the motion of randomly distributed particles flowing in a channel. Our method offers measurements of fluorescence intensity, particle image size and collocation between

multiple colors. The latter helps monitor particles which emit at multiple wavelengths and particle-to-particle type interactions. One unique feature of our technique is that it can monitor the time evolution of particle-particle interactions (we demonstrate evolution times of ~8 s, but this can be increased by changing flow and/or imaging conditions). Further, our image analysis can handle suspensions with particle densities in excess of 10^8 mL^{-1} (by comparison, FCM require densities of 10^6 mL^{-1} or less). All of the analysis can be performed in a suspension flow inside virtually any microchannel or tube with optical access for particle imaging (e.g., off-the-shelf microfluidic chips). Here we demonstrate a version of our technique optimized for analyzing specific particle-to-particle interactions and the resulting collocation and correlation of particle image motions.

Table 4.1. Brief review and comparison of multispectral particle analysis and enumeration techniques. We compare the capabilities and features of the current technique (PITC) with FCM and LSC.

	FCM	LSC	PITC
Cost	High	High	Low
Particle matrix	Hydrodynamically focused suspension	Fixed onto a slide surface	Flowing, random suspension
Multi-particle visualization	No	No	Yes
Spatially-resolved particle images	No	Yes	Yes
Number of measurements per particle	One	Several	5-20+
Time-resolved particle analysis	No	Yes	Yes
Particle-to-particle interactions	No	Yes	Yes
Particle rate	100-50,000 s^{-1}	Up to 100 s^{-1}	Up to 1000 s^{-1}
Spatial resolution	Low	High	Moderate
Recommended particle concentration	Up to 10^6 mL^{-1}	10^9 mL^{-1}	Up to 10^8 mL^{-1}
Minimum sample vol. required	Order 100 µl	Order 1 ul	Order 10 µl

4.2 Materials and methods

4.2.1 Overview of Collocation method

The example setup of our PITC method uses a standard epifluorescence microscope with a 20x objective, a CCD camera equipped with a dual-view color separator,[182] and a mercury arc lamp for illumination. The particles are suspended in an aqueous solution and loaded onto a microfluidics chip, as depicted schematically in **Figure 4.1**. The particles are transported through the interrogation region via electrophoresis. Our instrumentation is simple and off-the-shelf; and we rely instead on image analyses and computations for detailed analysis. Our custom particle tracking algorithm tracks each particle and monitors its location, size, diffusivity, fluorescence intensity, and its correlation to particle images at other wavelengths in time. Our technique can generate time resolved measurements for thousands of particles in minutes.
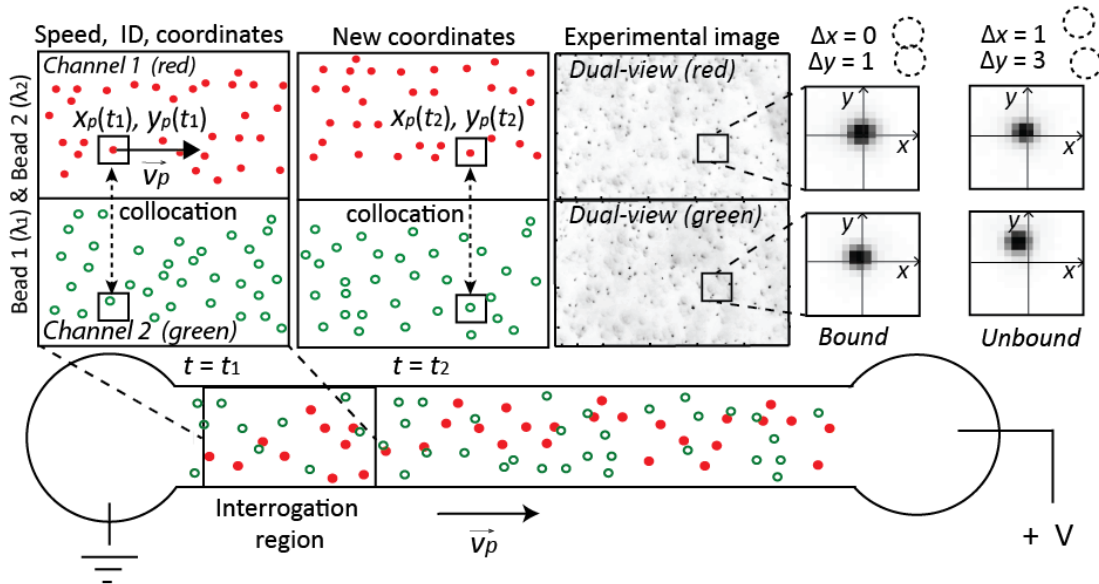
Figure 4.1. Particle imaging, tracking and collocation for particle monitoring and particle-to-particle binding assays. A two-color version is shown here, but the system is easily scalable to four colors using off-the-shelf instrumentation. A typical experiment involves (1) loading a solution containing particles

emitting in the red and green into a microchannel; (2) electrophoresing the particles through a detection region with optical access; and (3) imaging at a user-specified rate using a microscope equipped with dual-view system and high-sensitivity CCD camera. The dual-view system chromatically separates the particle images into separate spatial domains on the CCD array. The PITC algorithm determines location and in-plane velocity vectors of each particle in one spectral channel. This analysis is used to track the coordinates, image size, and fluorescence intensity of the individual particles in time. The subregions surrounding the particles in channel 1 are identified and tracked then cross-correlated with the corresponding subregions in the other channel. The persistence (in time) of a high cross-correlation signal indicates deterministically bound particles.

4.2.2 *Reagents and materials*

We purchased 1.0 µm carboxylate-modified FluoSpheres® microspheres (625/645), and 1.0 µm carboxylate-modified FluoSpheres® microspheres (505/515) manufactured by Molecular Probes, Life Technologies. The red bead was conjugated with 5'- Amino Modifier C12 – CGGATTGGAGTCTGCAACTCG and the green bead with 5'- Amino Modifier C12- CACAAAGTGGTAAGCGCCCTC. The conjugation reactions were performed by Radix Biosolutions (Georgetown, TX), and beads were suspended in Tris-EDTA, pH 8 at 2% solids. The functionalized beads were mixed with the target, a sequence that corresponds to a region in the E.coli 16S rRNA transcript:

AAACGAGTTGCAGACTCCAATCCGAAAAGAAGTAGGTAGCTTAACCTTCGGG AGGGCGCTTACCACTTTGTGTTT

The hybridization buffer contained 20 mM Tris, 10 mM hydrochloric acid, HCl, 0.08% Triton X-100 and 50 mM sodium chloride, NaCl. Reagents Tris, HCl, Triton X-100 and NaCl were purchased from Sigma-Aldrich (St. Louis, MO). The DNA was synthesized by Integrated DNA technologies, (IDT, Coralville, IA). The bead probes were desalted and the target sequence was PAGE purified. The buffered bead suspension was first

mixed with 100 nM target DNA in presence of $3x10^9$ beads/mL of each color and incubated at 60°C for 1 min followed by 50°C incubation for 10 min. The solution was diluted 10-fold with the hybridization buffer and pressure loaded into a poly(methyl methacrylate) microfluidic chip channel with dimensions 2 x 0.15 x 100 mm (**Figure 4.2**). The output well was filled with 50 µl of 1 M Tris-HCl buffer. The loading well was filled with the same buffer containing 25% Pluronic F-127 solution in order to reduce pressure driven flow. Platinum electrodes were placed in the loading and output wells and electrophoresis was initiated by applying a constant current of 100 µA. The bead suspension is imaged using an Olympus IX70 microscope equipped with a 20x, NA = 0.5 Olympus UPlanFl objective, a 16-bit CCD (Cascade 512F) camera (520 x 520 of 16 µm pixels). We achieved spatial separation of two wavelengths using an XF53 dual pass filter cube (Omega Optical) with peak excitation wavelength ranges of 475–500 and 550–600 nm, and peak emission wavelength ranges of 500–550 and 600–675 nm, in combination with a quad-view imager (Micro-Imager, Photometrics, Tucson, AZ). (Used here in dual-view mode for simple demonstration.) In a typical experiment, we record 200 images of particles illuminated with a mercury light source for 5 ms at a frequency of 1 Hz. During this time, order 1,000-10,000 unique beads traverse through the field of view. The particle motion and imaging rate can be increased for applications requiring higher throughput and where particles or cells require shorter evolution period monitoring.
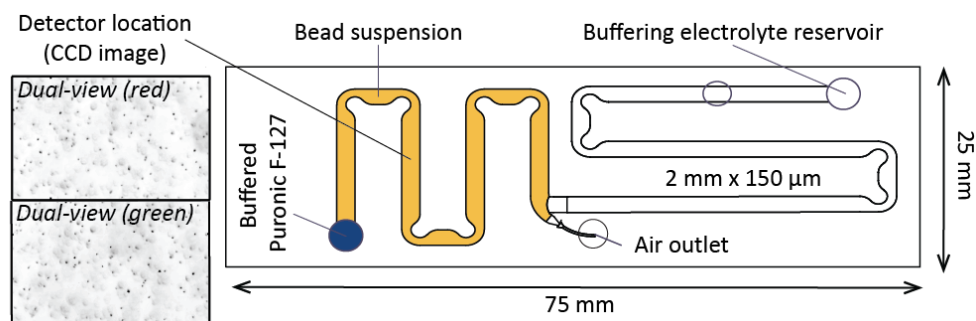
Figure 4.2. Fluidic channel architecture and loading protocol used in demonstration of particle imaging, tracking and collocation method. A poly(methyl methacrylate), PMMA, microfluidic fluidic chip with dimensions (10 cm x 2 mm x 150 µm) is loaded with the buffered bead suspension. The output well was filled with 50 µl of 1 M Tris-HCl (pH 8) buffer. The loading well was filled with the same buffer containing 25% Pluronic F-127 solution in order to reduce pressure driven flow. Platinum electrodes were placed in the loading and output well and electrophoresis was initiated by applying 100 µA across the microchannel. In a typical experiment, we record 200 chromatically separated particle images at a frequency of 1Hz. During this time, order 1,000-10,000 unique beads traverse through the field of view.

We note here that most biological laboratories already have access to epifluorescence microscopes and CCD cameras. Our method requires only a CCD camera with fairly good sensitivity and imaging rates of about 1 frame per second or higher. We also require an off-the-shelf dual- or quad-view type image splitter. The dual-view imager and filter set for two-color imaging is currently available for $11,000, while a quad-view (for four color imaging) is available for $19,000. We believe our method is amenable to further lowering component cost.

4.2.3 Imaging and particle residence time requirements

Our algorithm relies on particle brightness patterns, and so we recommend imaging conditions such that particle image diameters correspond to distances of 3 or more pixels (roughly 3 to 8 pixels is ideal). To discriminate between bound and closely neighboring particles we can monitor the persistence (in time) of the spatial correlation of

83

particle images. This option places a minimum requirement on the amount of time the algorithm tracks particles. The algorithm should track particles long enough for Brownian motion or other dispersion to cause separation of unbound particles. For particle separation phenomena determined by Brownian motion, we can estimate this minimum time of observation from particle diffusivity. For particles with radius, r_p, and particle image radius (geometrically projected into the object plane), r_{pi}, we recommend the following relation to estimate the minimum time, t_{ch}, over which to track particle pairs undergoing Brownian diffusion:

$$L_{ch} = \sqrt{4D_{eff}t_{ch}} > \left[\left(r_{p,1} + r_{p,2} \right) + \left(5/4 \right) \min(r_{pi,1}, r_{pi,2}) \right]. \tag{4.1}$$

Here, L_{ch} is a characteristic minimum particle center-to-center distance in object space, required before the algorithm concludes the particles are not bound. At the characteristic time, t_{ch}, diffusion statistics[183] suggest that 67% of all randomly aligned particles pairs with effective diffusivity of D_{eff}, are separated by L_{ch}. We estimate the Brownian separation distance between two particles using an effective diffusion coefficient of the form $D_{eff} = D_{p1} + D_{p2}$, where D_{p1} and D_{p2} are respectively the diffusivities of particles imaged in channels 1 and 2. Here we assume that the diffusive motions of the closely-spaced particles are statistically independent.[183] Combining equation (4.1) with the Einstein diffusivity expression,[184] $D_p = 2kT/3\pi\mu r_p$, we can solve for the characteristic minimum evolution time:

$$t_{ch} = \frac{3\pi\mu \left(\left(r_{p,1} + r_{p,1} \right) + \left(5/4 \right) \min(r_{pi,1}, r_{pi,2}) \right)^2}{2kT \left(\dfrac{1}{r_{p,1}} + \dfrac{1}{r_{p,2}} \right)} \tag{4.2}$$

In our experiments, this time is roughly 2.5 s. Appropriate choices for monitoring time are discussed further in the 'Validation and Performance' section.

So far, we focused on the point-to-point lateral resolution and separation distance in the plane perpendicular to the optical axis. Another important consideration is the depth of field, L_{Df}, which is determined by the distance from the nearest object plane in focus to that of the farthest plane. In microscopy depth of field is very short and it is determined only by the numerical aperture of the objective. In general, high numerical aperture systems have higher magnification power. For particle tracking and colocation analysis, we recommend choosing imaging conditions that ensures that the tracked particle hybrids remain in focus for the minimum required elution time. This condition is met if the depth of field is larger than the characteristic length, $D_f > (r_{p,1} + r_{p,2}) + (5/4)\min(r_{pi,1}, r_{pi,2})$. This requirement can place a constraint on the maximum magnification power of the optical train. When higher resolving power is required, alternative means to keep particles is focus may be necessary.

4.2.4 Particle tracking and collocation algorithm

Figure 4.3 shows an overview of our PITC algorithm, which we implemented on MATLAB (Mathworks Inc., Natick, MA). We first spatially register the two spectral channels using a bright field image of an alignment mask. The algorithm is then divided into two phases. In the first phase, we analyze particle images from one spectral channel (Channel 1) to identify and track particle coordinates, size and fluorescence. In the second phase, we perform collocation, which analyzes the region in the second channel images (Channel 2) which are immediately near particles identified in the first channel.

85

The process can be performed twice with the first phase starting with each of the two channels. This enables counting and tracking particles individually in each channel and corroboration of the collocation analysis. For the current demonstration, the algorithm is performed as a post-process routine but the process is amenable to parallelization and real-time implementation. In the following sections, we provide details of the particle tracking and particle collocation phases.

Figure 4.3. PITC algorithm structure. Each image sequence contains data for thousands of unique particles. After registration of the two images, the algorithm proceeds in two main phases. The first phase quantifies local drift particle velocities using micron resolution particle image velocimetry (micro-PIV). Unique particle images in Channel 1 (Ch1) are then identified, located and characterized via the particle mask correlation and particle characterization (PMC-PC) method. The particle image intensity and radius are evaluated using a non-linear Gaussian fitting routine. The algorithm then combines results of PMC-PC and micro-PIV for a particle tracking velocimetry (PTV) subroutine enhanced by Kalman filter and χ^2-testing method (KC-PTV). This analysis results in accurate determination and tracking of the location of each particle over time and space. The second phase of the algorithm cross-correlates subregions surrounding the particle locations identified in Ch1 with corresponding subregions in the registered Ch2. Ch2 particle characteristics, such as radius and total fluorescence, are evaluated using the Gaussian fitting

subroutine. Thresholds for intensity, size, velocity, and correlation coefficient are applied at each step to eliminate spurious results.

Alignment and spatial registration

We spatially register the two channel images using a bright field image of an alignment pattern (Negative 1951 wheel pattern resolution test target from Thorlabs, R3L1S4N). Example misaligned (initial) and aligned (final) versions of this test pattern are shown in **Figure 4.4**. We used Matlab's function imregister, an iterative process that requires a pair of images, an image-similarity metric, an optimizer, and a transformation type. The metric defines the image similarity for evaluating the accuracy of the registration. The optimizer defines the methodology for minimizing or maximizing the similarity metric.
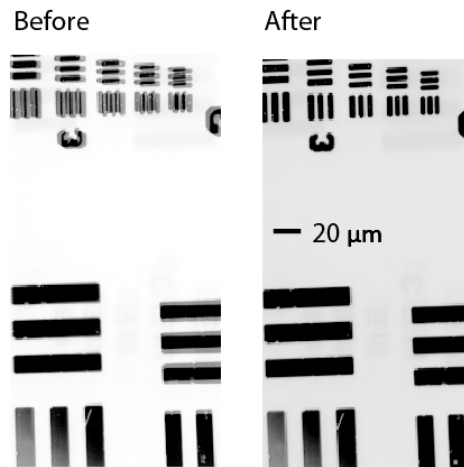
Figure 4.4. Example of misaligned (initial) and aligned (final) bright-field images of two spectral channels recorded with a quad-view imager (Micro-Imager, Photometrics, Tucson, AZ), used here in dual-view mode. The images are plotted using Matlab's function, imshowpair, which displays the differences between two images. We used alpha blending to overlay the two spectral channel images before (left) and after (right) image registration. Note, alpha blending is the process of combining a translucent foreground color with a background color, which produces a new blended color. These test images were taken with a 20x objective with a numerical aperture of 0.5.

We used Matlab's function imconfig to generate the optimizer and metric assuming multimodal image capture, as the brightness range in the two spectral channels are different. The transformation type used for the image alignment is specified as "rigid", which consists of translation, and rotation. We set the maximum iterations to 1000. The ROI coordinates and the transformation matrix generated in this alignment phase are then used to translate and rotate the Ch2 particle image to achieve spatial registration with Ch1. Using images of simulated particle patterns; we have verified that this alignment procedure results in registration with sub-pixel accuracy. Note, the image alignment and registration process will produce artifacts at the perimeter of the images, which are eliminated by trimming ~ 5 pixels from the image edges. This entire process needs to be performed only periodically as a part of the instrumentation calibration procedure.

Particle tracking phase (Channel 1)

Micron-resolution Particle Image Velocimetry

We use measurements of spatially correlated particle motion (i.e., velocities averaged over finite subregions containing multiple particles) to guide our individual particle tracking algorithm. This correlated particle motion is the result of non-Brownian transport such as fluid flow or electrophoresis or both. micro-PIV provides a robust and high-resolution method for determining such spatially correlated particle velocities.[185] micro-PIV was developed specifically for microfluidic applications, and has been reviewed and described extensively.[186-188] The process limits particle tracking to particles near the focal plane of epifluorescence imaging.[188] The process measures two components (x- and y-velocities) of the velocity field in the imaging plane. For our

88

micro-PIV analysis, we used 30 by 100 pixel interrogation regions with 50% overlap (for a total of 25 interrogation regions).[189, 190] Since the flows here were approximately steady, we averaged velocity information by ensemble averaging 50 correlations functions (each associated with an image pair) per velocity calculation.[191] (For experimental data in **Figure 4.9** and **Figure 4.10**, we ensemble averaged over 200 correlation functions)

Particle Mask Correlation method and Particle Characterization

In parallel with micro-PIV analysis, our method identifies particle images and their coordinates by employing the PMC[192] method. PMC convolves raw images with a kernel "mask" made up of a two dimensional circularly symmetric Gaussian brightness pattern, I_{ma}, expressed as follows:

$$I_{ma}(x, y) = A \exp\left[-\frac{(x - x_o)^2 + (y - y_o)^2}{2\sigma_m^2} \right] + b \qquad (4.3)$$

We set the peak brightness, A, to unity, but note, that it can be set to any value, since we perform normalized cross-correlations between the image and particle mask (see Eq. 4.3). The mask brightness background, b, is set to zero.

The mask standard deviation, σ_m is chosen equal to or smaller than the radius of the smallest expected particle image radius in the image set. In our experiments, the particle brightness spans approximately 3 pixels, and so we set $\sigma_m = l_p$, where l_p is the pixel size in the object plane. The particle mask is scanned over the entire image plane and the normalized cross-covariance coefficient, r_{PMC} is calculated at each pixel location, (x_o, y_o). The normalized cross-covariance coefficient between the particle mask centered at (x_o, y_o) and the image subregion of same size centered at (x_o, y_o) are computed as follows:

89

$$r_{PMC}(x_o, y_o) = \frac{\sum\limits_{i=x_o-m/2}^{x_o+m/2}\sum\limits_{j=y_o-n/2}^{y_o+n/2}(I(i,j)-\hat{I})(I_{ma}(i,j)-\hat{I}_{ma})}{\sqrt{\sum\limits_{i=x_o-m/2}^{x_o+m/2}\sum\limits_{j=y_o-n/2}^{y_o+n/2}\left(I(i,j)-\hat{I}\right)^2}\sqrt{\sum\limits_{i=x_o-m/2}^{x_o+m/2}\sum\limits_{j=y_o-n/2}^{y_o+n/2}\left(I_{ma}(i,j)-\hat{I}_{ma}\right)^2}}$$ (4.4)

where $I(i,j)$ is the brightness value of particle image plane at (i,j).[192] In this study, we set the particle mask size (n,m) to $8\sigma_m$ x $8\sigma_m$. r_{PMC} varies between -1 to 1, depending on the degree of similarity between the brightness patterns. Pixels with high covariance coefficients indicate the presence of particles. Using a covariance threshold of 0.7 enables the PMC method to find all concentric convex brightness patterns of size of roughly < 8 σ_m.[192] The calculated covariance coefficient plane is binarized using this threshold. For simplicity, we assign the pixel with the highest r_{PMC} value as the coordinate for the center of the particle, $(x_{p,1},y_{p,1})$. As an approximation, we evaluate the particle image radius (geometrically projected into the object plane) as $r_{pi,1} = \sqrt{(pl_p)^2/\pi}$, where p is the number of 'unity' pixels for a particle group in the binarized image, and l_p is the size of the pixel in the object space. While the cross-covariance was performed on raw particle images, the particle intensity, $I_{p,1}$, is estimated by summing the background corrected intensity of a $4r_{pi,1}$ x $4r_{pi,1}$ subregion centered at the particle center $(x_{p,1}, y_{p,1})$. The corrected images are evaluated as follows:

$$I_c = \frac{I_{raw} - I_{bg}}{I_{flat}} \quad .$$ (4.5)

The background of the raw image, I_{bg} is obtained by filtering the original image with a median filter of size 10x10. The flatfield, I_{flat}, is obtained by imaging the microchannel

filled with uniform concentration of dyes (100 nM AF488 and 100nM AF647) which are processed with a median filter of size 10x10.

We note that our method can significantly improve the accuracy of particle localization and size and fluorescence characterization by using a sub-pixel resolution method. The sub-pixel resolution approach fits the particle brightness pattern in the local $8\sigma_m$ x $8\sigma_m$ subregion of background corrected particle image using a non-linear Gaussian fitting routine. The brightness pattern is defined by Eq. 4.3, where we set the standard deviation equal to the particle image radius, $\sigma_m = r_{pi,1}$. The fitting routine uses the median intensity of the $8\sigma_m$ x $8\sigma_m$ subregion as the background, b; the highest pixel intensity minus the background as the amplitude, A; and the simple estimates, described above, for particle coordinates and particle radius for $x_{p,1}$, $y_{p,1}$ and $r_{pi,1}$, as a first guess. We used and recommend the fitting routine for more detailed cytometry-like data of particle populations. For the simulated particle-to-particle binding assay data we present in **Figure 4.6** and **Figure 4.7** below, we disabled this Gaussian fitting algorithm step in order to save computational time.

To eliminate large aggregates and out-of-focus particles from analysis, we implemented size- and intensity-based threshold filters. For the particle-to-particle collocation analysis presented in this study (unless stated otherwise), we set the size-based threshold to eliminate particles with radii larger than the mean plus 2 times the standard deviation of the particle population in each image. The intensity-based threshold eliminated all features with intensity 3 times the standard deviation away from the mean of the particle population.

Kalman filter and χ^2-test *enhanced Particle Tracking Velocimetry*

For robust and accurate operation, we us *Kalman filter* and χ^2-test[192, 193] to identify and track each unique particle over time and space. This latter method, KC-PTV, was developed by Etoh and Takehera for particle tracking velocimetry.[192, 194] KC-PTV was later adapted for microfluidics by incorporating micro-PIV.[195, 196] In KC-PTV, particle image data (here location, fluorescence intensity, and particle image radius) from the first time step ($t = 0$) is used to predict the particle information in the next time step ($t = t+\Delta t$). The probability of two particle images belonging to the same particle identity is evaluated using a χ^2-test which uses these image data as parameters. See work by Takehara and co-workers[192, 193] for more detailed information on the implementation of the approach.

In this phase of our algorithm, we apply filters to the data which reject particle image motions which are significantly far from bounds determined by local micro-PIV velocity data and particle diffusion estimates. For example, we reject particle matches with apparent velocities, $\vec{v}_{p,a}$, which fail the following criteria: $5v_{diff} > \left| \vec{v}_{p,a} - \vec{v}_{PIV}(x_{p,1}, y_{p,1}) \right|$. Here, $v_{diff} = \sqrt{4D_p / \Delta t}$, and $\vec{v}_{PIV}(i, j)$ is the drift velocity at the particle position ($x_{p,1}, y_{p,1}$) obtained from micro-PIV analysis. Output parameters from this phase, including particle identification number (ID), coordinates, $x_{p1}(t)$, $y_{p1}(t)$, particle image radius, $r_{pi,1}(t)$, and integrated background-corrected fluorescence intensity, $I_p(t)$, are stored for further processing.

Particle collocation phase from Channel 1 and 2 data

Our particle collocation approach begins by positioning a small $8\sigma_m$ x $8\sigma_m$ subregion at the coordinates of each particle identified and tracked in Ch1. The algorithm then selects a $16\sigma_m$ x $16\sigma_m$ subregion in Ch2 centered at the same coordinates. We limit the shifts in correlations so that the Ch1 subregion always completely overlaps the Ch2 subregion, and so we eliminate the known biases associated with cross-correlations of finite-sized correlation functions.[189, 190] For the collocation analysis, we evaluate the normalized cross-covariance as described by Eq. 4.4, but where we set I_m to the Ch1 subregion and set I to the Ch2 subregion. The parameter r_{PMC} is then interpreted as the degree of correlation in the position of the particle or particles detected in both Ch1 and Ch2, which we refer to as collocation coefficient, $R_{12}(x_o, y_o, t)$. $R_{12}(x_o, y_o, t)$ is evaluated for widow offsets of (x_o, y_o) equal to or less than a predefined minimum value, $Sh = (r_{p,1} + r_{p,2}) + (1/4)\min(r_{pi,1}, r_{pi,2})$. We initially assign the offset (x_o, y_o) with the highest $R_{12}(x_o, y_o, t)$ value as the coordinate for the center of the Ch2 particle, $(x_{p,2}, y_{p,2})$. If the maximum coefficient, $R_{12,\max}$, is below 0.6, we conclude that no particles are present in Ch2 subregion. For such a case, we set $r_{pi,2} = 0$ and estimate $I_{p,2}$ as the sum of the background corrected particle image intensity (Eq. 4.5) of a $4r_{pi,1}$ x $4r_{pi,1}$ subregion centered at $(x_{p,1}, y_{p,1})$ in Ch2. If $R_{12,\max}$ is above 0.6, we conclude that there is a particle in the Ch2 subregion. To estimate the radius of the particle, we first binarize the collocation matrix and find the group of unity pixels associated with the Ch2 particle coordinates $(x_{p,1}, y_{p,1})$. We approximate the particle image radius (in object plane) as $r_{pi,2} = \sqrt{(pl_p)^2 / \pi}$. Particle radius is subsequently used to determine the Ch2 particle

intensity, $I_{p,2}$, by summing the background corrected image intensity (Eq. 4.5) of a $4r_{pi,2}$ x $4r_{pi,2}$ subregion centered at $(x_{p,2}, y_{p,2})$.

Recall that the particle characterization method can significantly improve the accuracy of particle localization, size and fluorescence characterization by using a sub-pixel resolution method as described in the PMC subsection. We implement the non-linear Gaussian fitting routine in data analysis presented in **Figure 4.9** and **Figure 4.10**.

Interpreting collocation data

The persistence (in time) of a high cross-correlation signal indicates deterministically bound particles. This is in contrast to unbound, but closely neighboring particles, which eventually separate due to Brownian motion and/or dispersion. We therefore identify particles as bound only if their collocation coefficient $R_{12,\max}(t)$ remains sufficiently high for longer than a predefined minimum tracking time, t_{ch} determined from Eq. 4.2. Particle image pairs in Ch1 and Ch2 with collocation traces, $R_{12,\max}(t)$, with a median collocation value above a predefined threshold, $\tilde{R}_{12}$, are determined to be bound. Appropriate choices for median collocation thresholds are discussed in the following section.

To prevent highly correlated, non-particle related events to contribute to bound event counts, we have also implemented an intensity-based threshold filter, which

removes all collocated events with intensities 3 (for simulated) and 1 (for experimental) data) standard deviation away from the mean of the "bound" particle population.[1]

4.3 Validation and Performance

4.3.1 Monte Carlo simulations

We used Monte Carlo simulations to guide our choices of user specified algorithm parameters and to demonstrate the performance and robustness of our particle collocation algorithm. We first performed Monte Carlo simulations of Brownian particles with Gaussian brightness patterns of one pixel standard deviation (see **Figure 4.5** for example images). The particles were randomly distributed in a 500 x 150 cell simulation domain which corresponded to the pixel array. Particle diffusivity was set to 0.44 µm^2/s, and the particles were given a uniform advective velocity of $v_{p,x}$ = 10 µm/s. As typical with Brownian Monte Carlo, we chose specular reflection boundary conditions for the side walls of the simulation domain. Further, particles exiting the x = 150 end of the domain were reintroduced at x = 0, at random y-coordinates. To explore the sensitivity of our method to experimental conditions, we simulated the following variations: (1) percentage of bound particles between the two channels ranged between 0-100%, (2) inter-particle distance varied between 5 to 20 µm, and (3) image signal to noise ratio (SNR) ranged between 2 to 100. Note, that the average inter-particle distance of nearest neighbor particles can be determined as L_{IP}=0.5539$d^{-1/3}$,[183] where d(m^{-3}) is particle density. Inter-

---

[1] We note here, that the effectiveness of these filters relies on access to accurate particle intensity and size distributions. For experiments where the fraction of bound particles are zero or exceptionally low, the intensity and size distribution of Ch2 particle images are biased from false positive collocation matches. For example, in a negative control experiment, most collocation matches are due to image artifacts. Therefore, the intensity and size characteristics of their distribution should not be used in these filters. We thus recommend the calibration of particle intensity and size via PMC-PC in Ch2 before collocation analysis.

particle distance of 5 to 20 µm is equivalent to about 800 to 50 particles in a 500 x 150 simulation domain.

4.3.2 Image SNR and median collocation threshold

The probability of successful particle identification and collocation rely strictly on the degree of correlation between two normalized brightness patterns. Signal-to-noise ratio (SNR) has a strong effect on the brightness pattern of raw particle images. We define SNR as the peak particle intensity above the mean of local background divided by 2 times the standard deviation of background image intensity. To determine how SNR influences particle tracking and collocation accuracy, we added Gaussian white noise to the simulated particle fields (see **Figure 4.5** for simulated images with SNR of 2 and 100). During the 200 s simulation time, we introduced 1422 of unique particles, 1200 of which had a residence time of roughly 15 s. We performed particle tracking on the simulated images and plot in **Figure 4.5** the histogram of tracked particle times (duration over which algorithm tracks each particle) as a function of SNR. In the case of low image SNR (SNR = 2), over 200 s, approximately 5000 particles were identified, but only 10% were tracked for 3 s or longer. Note, that when the algorithm loses a particle due to the interfering effects of SNR, if the same particle reemerges at a later time step, it is identified as a new particle (as would happen in an experiment). Consequently, the number of particle counts increases, and residence time shortens with increasing image noise. Consistent with this is the large discrepancy present between the number of particles detected (~5000) and simulated (~1400) at SNR = 2. For image SNR of 5 or above, the number of particles identified and their tracked time converges to the known values.

96
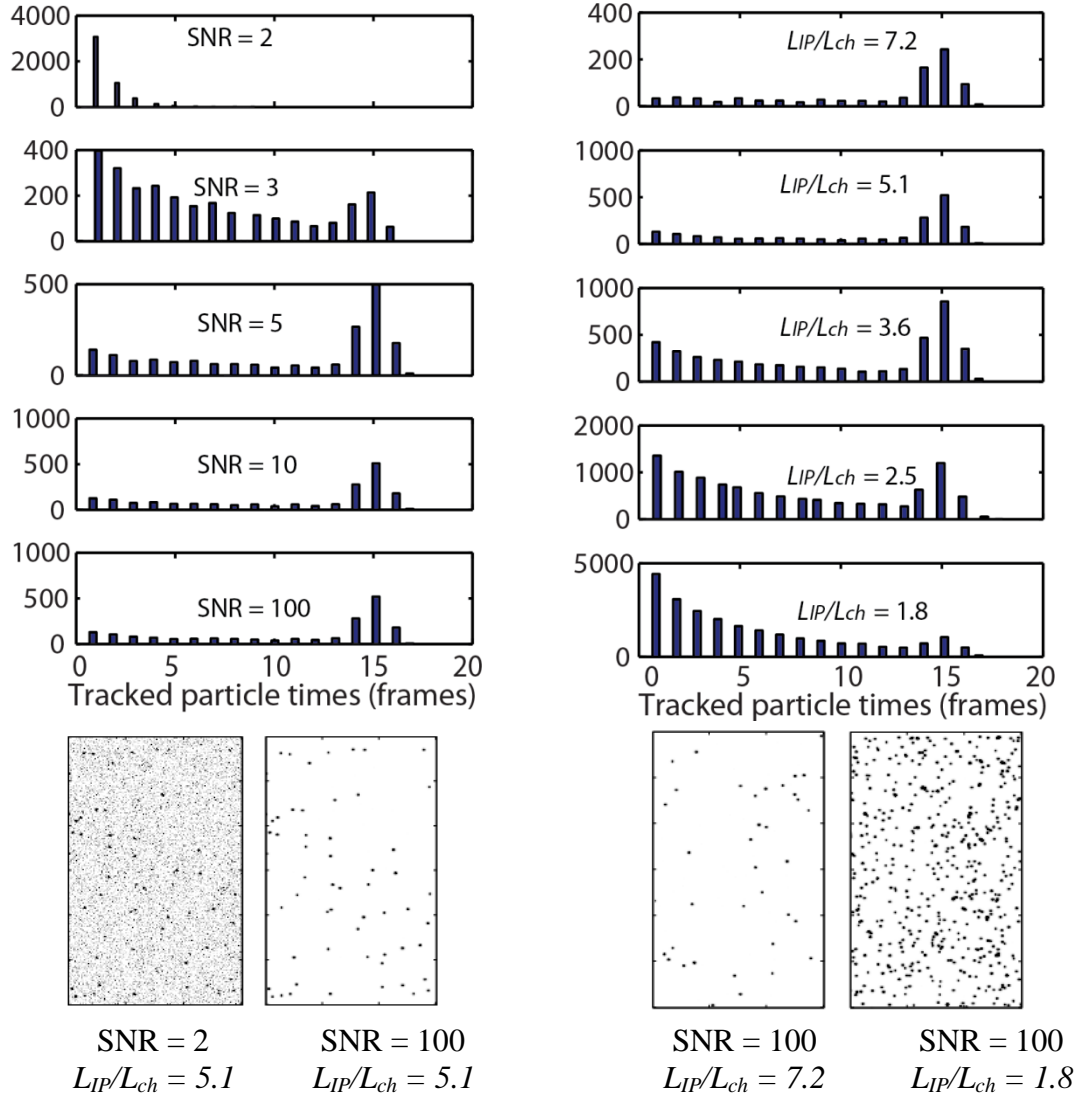
Figure 4.5. Histogram of the number of particles that were tracked for 1 to 20 frames. Left: Simulated particle density was set to 100 particles/domain (L_{IP}/L_{ch} = 5.1). The PMC method relies on brightness patterns for identification of particles. When SNR is too low (SNR ≤ 6), the brightness patterns are distorted and particles are not easily identified. Right: SNR for Monte Carlo simulated images were set to 100. PMC method fails if particle brightness pattern is overly affected by neighboring particles and Kalman filter and χ^2 test will fail as trajectories of closely spaced particles become indistinguishable. As the inter-particle distance decreases, the particles can be tracked successfully for progressively shorter times as they are lost due to particle crowding. For $L_{IP}/L_{ch} \leq 3.6$ large fractions of these particles are tracked for shorter times than that required for collocation (i.e., the minimum evolution time, t_{ch}, defined in Eq. 4.2).

In **Figure 4.6**, we show the combined accuracy of particle tracking and collocation as a function SNR and collocation median threshold, $\tilde{R}_{12}$ for two different simulation fractions of bound particles. For both cases of 3% and 50% bound particles, increasing image SNR improves collocation accuracy. In general, strong image noise results in an underestimation of the bound fraction. Of the severest of cases, SNR = 2, no bound particles were detected for any collocation thresholds in the tested range ($\tilde{R}_{12} = 0.6 - 0.8$). The collocation results for images with SNR of three, using threshold of $\tilde{R}_{12} = 0.6$ are in close agreement with the simulated values, but raising $\tilde{R}_{12}$ to 0.8, causes complete failure of the collocation analysis. For SNR > 5, the collocation accuracy is weakly dependent of SNR and collocation thresholds. For example, prediction of PITC analysis of the 3% bound fraction case (solid line) at SNR = 10, is 2.91%, when $\tilde{R}_{12} = 0.6$ and 2.64%, when $\tilde{R}_{12} = 0.7 - 0.8$. Based on these analyses, we determined that a value of $\tilde{R}_{12} = 0.6$ yields an appropriate accuracy for a fairly wide range of image SNR.

In the inset of **Figure 4.6**, we also show the results of collocation performed on image sets with 0% simulated bound particle fraction. At image SNR = 100, the PITC algorithm found that bound particle doublets made up 0.9%, 0.6%, and 0.25% of the total particles with collocation threshold values of 0.6, 0.7 and 0.8, respectively. False positive collocation detections occur in the negative control case due to failure of the particle intensity threshold filter we implemented in the collocation phase. This intensity based threshold relies on the intensity distribution of true positive particle matches in Ch2. Since there are no true positive matches in the negative control case, the intensity distribution obtained this way is not a true representation of the Ch2 particle intensities.

These bound fractions in **Figure 4.6** inset, therefore, represent the limit of detection (LOD) of our method in the absence of a priori Ch2 particle intensity calibration. To improve the LOD, we recommend the evaluation of particle intensities in Ch2 using the PMC-PC method. The calibrated intensity distribution can then be used to filter particle matches in the collocation phase. After we performed a simple calibration of Ch2 particles, the PITC algorithm detected 0% bound fractions for all collocation thresholds in the negative control case.
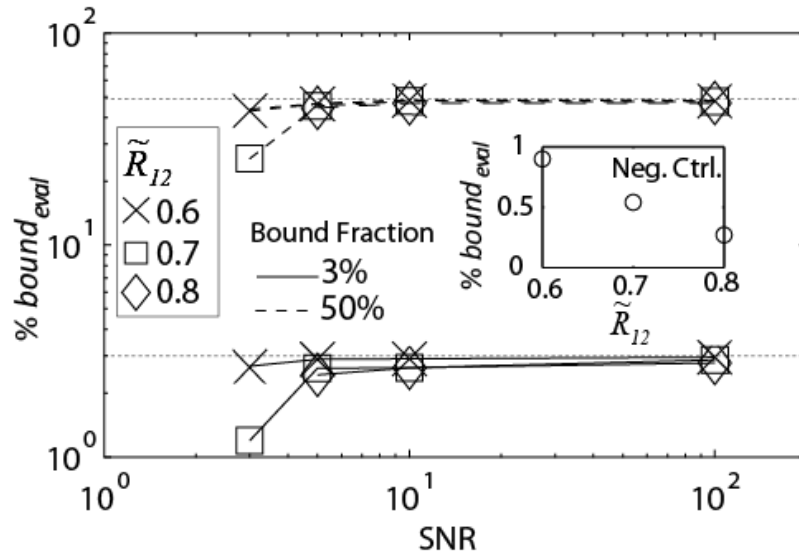
Figure 4.6. Accuracy of particle hybrid count as a function of simulated SNR and the median collocation threshold, $\widetilde{R}_{12}$. The total number of 1 μm diameter particles in each image from the Monte Carlo simulation is 100 (with a mean inter-particle distance of roughly 15 μm). The simulated fraction of bound versus total particle number was 0% (inset), 3% (solid line) and 50% (dashed line). Particles were considered only if they were tracked for 10 s or longer. For the tested range of collocation thresholds, the bound particle fraction is underpredicted. For the highest collocation threshold of 0.8, PITC detected no bound particles for SNR < 5. As SNR increases above 5, the detected bound fraction converges to the simulated values. In inset, we show 0.9%, 0.5% and 0.3% false positive bound fraction detected in the negative control case for the three collocation threshold values. The false positive bound fraction is reduced to 0% for all $\widetilde{R}_{12}$, when Ch2 particle intensity distribution (calibrated Ch2 particle intensity) is used as the basis of the intensity-based filter in the collocation phase.

4.3.3 *Particle density and monitoring time*

The rate of particle analysis of our collocation method is primarily limited by two parameters, the maximum particle concentration tolerated by the PITC algorithm and the minimum monitoring time, t_m. Here we examine the effect of these parameters on particle tracking and collocation performance. We analyzed image pairs containing 50, 100, 200, 400 and 800 particles per image, 3% of which were deterministically bound. During the 200 s simulation time, we introduced 718, 1437, 2851, 5692 and 11314 unique particles, most of which had a residence time (time spent in the field of view) of roughly 15 s. In **Figure 4.5** of the SI, we show a histogram of particle tracked times as a function of particle density. High particle density is associated with short inter-particle distances. Since neighboring particles influence the brightness pattern of those that are tracked, the success rate of particle tracking decreases with increasing particle density. For image sets containing 200 or more particles, the tracked times are limited by particle crowding, and not by the user specified parameters such velocity and interrogation widow-size. For example, for the highest particle density case (800/image), most particles can be tracked for at most 5 s.

In **Figure 4.7**, we elucidate the influence of particle density on collocation performance by comparing the inter-particle distance, L_{IP}, to the characteristic distance that two randomly aligned particles must separate for the algorithm to consider them unbound, L_{ch} (Eq.4.4). Here we also examine the influence of monitoring time, t_m on collocation by comparing t_m to the minimum elution time, t_{ch} (Eq. 4.2), the characteristic time it takes two randomly bound particles to separate by L_{ch}. **Figure 4.7** shows the ratio between the evaluated and simulated bound fraction as a function of L_{IP}/L_{ch} and t_m/t_{ch},

using two collocation thresholds $\widetilde{R}_{12} = 0.6, 0.7$. In a single instance in time, the collocation algorithm cannot differentiate between random and deterministic particle interactions. When particle densities are low (high L_{IP}/L_{ch}), the random particle-particle interactions are rare, and the bound fractions detected by PITC converge to the simulated values for all t_m and $\widetilde{R}_{12}$. When high particles densities (low L_{IP}/L_{ch}) yield frequent random particle-particle interactions, the bound particle fractions for short observation times are over-predicted as expected. For example, for $L_{IP}/L_{ch} = 1.8$ and a collocation threshold of $\widetilde{R}_{12} = 0.6$, the PITC algorithm detects ~6.2 times the simulated bound particle events for the shortest monitoring time ($t_m/t_{ch} = 0.77$). Using a more conservative collocation threshold, $\widetilde{R}_{12} = 0.7$, this error reduces to ~3.2 times the simulated fraction. For both values of $\widetilde{R}_{12}$, increasing monitoring time improves collocation accuracy. When we increase the monitoring time to more than four times the evolution time of particle pairs ($t_m/t_{ch} > 3.87$), the PITC algorithm detects ~1.5 times the simulated fraction at a challenging value of $L_{IP}/L_{ch} = 1.8$ (using $\widetilde{R}_{12} = 0.7$). While this trend suggests that increasing monitoring time leads to improved collocation accuracy, recall from **Figure 4.5** at high particle densities, the monitoring time is severely limited by the short L_{IP}. Based on these results we recommend using particle densities which yield approximately $L_{IP}/L_{ch} > 3.5$, and collocation threshold of $\widetilde{R}_{12} = 0.7$, but note that low SNR images will likely require a slightly lower value of 0.6 or 0.65. Finally, for all cases, we conclude that increasing monitoring time increases collocation certainty. In general, we recommend monitoring times of 2 times the minimum evolution time, t_{ch}, or higher. For our recommend value of $\widetilde{R}_{12} = 0.7$ and a value of $t_m/t_{ch} = 3.87$, PITC predictions are within

~10% or less for SNR = 100, for the case of only 3% particles bound (bound fraction is estimated between 2.7% - 3.3%).

Based on the aforementioned study of the influence of L_{IP}/L_{ch}, we recommend using particle densities which yield approximately $L_{IP}/L_{ch} > 3.5$, and a collocation threshold of $\tilde{R}_{12} = 0.7$. We note that images with SNR of less than about 5 will likely require a slightly lower value of $\tilde{R}_{12}$ (say 0.6 or 0.65). In general, we recommend monitoring times of 2 times the minimum evolution time, t_{ch}, or higher.
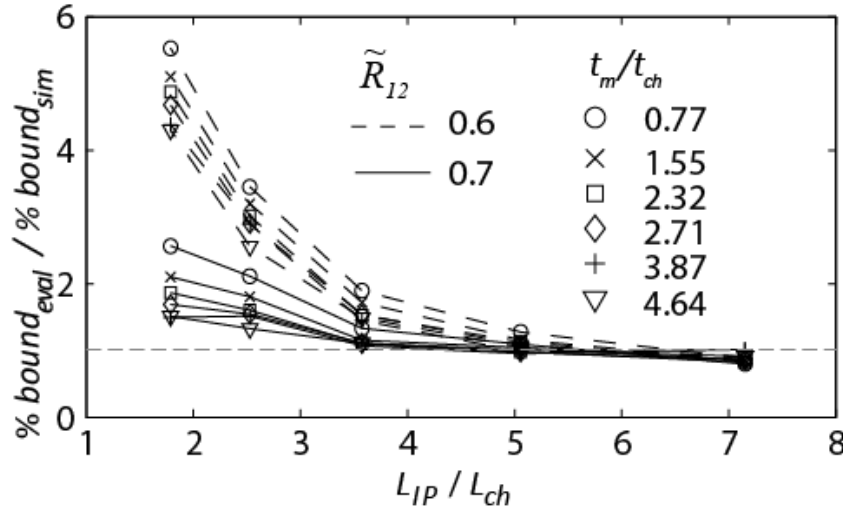
Figure 4.7. Accuracy of particle hybrid count as a function of particle density, monitoring time, and collocation threshold. The simulated fraction of bound particles was set to 3%, and the image SNR to 100. For all collocation thresholds, as the inter-particle distance decreases, the frequency of random particle-particle interaction increase. As a result, the algorithm overestimates the bound particle fraction. While the accuracy of collocation improves by increasing the monitoring time, t_m, and increasing collocation threshold, $\tilde{R}_{12}$ from 0.6 to 0.7, the error in the detected fraction for $L_{IP}/L_{ch} < 3$ is still significant. At $L_{IP}/L_{ch} =$ 1.8, $\tilde{R}_{12} = 0.7$, and $t_m/t_{ch} = 3.87$, PITC detects 4.5% bound. Using the same algorithm settings on image sets with lower particle density, PITC detects 3.23%, 2.87 % and 3.06% bound particle fractions at L_{IP}/L_{ch} of 3.6, 5.1 and 7.2, respectively.

4.4 Experimental demonstration of cytometry-like data and collocation analysis

We here show an experimental demonstration of our particle tracking and collocation method by analyzing a solution containing two populations of 1 µm diameter, fluorescent beads and DNA targets of length 173 nt. Each bead population has a unique spectral signature and each is functionalized with unique molecules complimentary to the target (21 nt sequences for both Ch1 and Ch2 beads). Upon hybridization to the complimentary oligos, the target DNA bridges the two beads, creating a two-color bead doublet (**Figure 4.8**). The resulting bead solution containing three bead populations, red singlets, green singlets, and red-green bead hybrids, were loaded onto a microfluidic chip (**Figure 4.2**) and imaged with our dual-view system. We also performed a negative control experiment, using bead suspension absent of the DNA target.
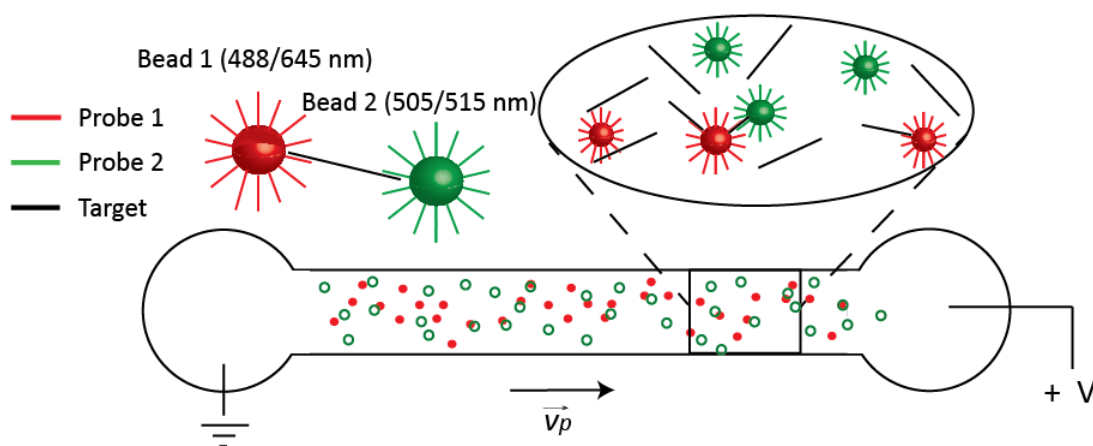
Figure 4.8. Collocation particle imaging for DNA detection. A solution containing red and green beads was mixed with target DNA in a hybridization buffer. Bead doublet formed when Probe 1 on red fluorescence bead (Bead 1) and Probe 2 on green fluorescence bead (Bead 2) are hybridized to the target DNA sequence. The bead-DNA mixture was electrophoresed in a channel with a transparent top wall and visualized using a microscope equipped with a dual-view system and high-sensitivity CCD camera.

4.4.1 Time resolved collocation coefficient

Monitoring collocation and other particle parameters in time improves the accuracy of our estimates, as many sources of variation are uncorrelated in time. One example of this is the discretization error associated with imaging with a CCD array. For instance, particle intensities can vary significantly depending on the location of their center relative to the pixel edge. Another source of variation is associated with the random interaction between particles which can cause 'spikes' in the collocation coefficient, $R_{12,max}(t)$. Acquiring a single realization in time would therefore yield significant error in particle-to-particle binding studies. In **Figure 4.9**, we show this phenomenon by plotting the collocation coefficients evaluated from the experimentally obtained image sets. We set the minimum monitoring time to 8 s, which is approximately 3.2 times longer than the characteristic evolution time, t_{ch}, for this experiment. Filtering particles based on the 8 s of minimum monitoring time yielded time-resolved measurements of particle fluorescence, radius, and collocation for 163 red beads. The plot in the figure shows 50 representative traces of the time-resolved collocation coefficient, $R_{12,max}(t)$, for the red particles correlated with the green channel in the presence of DNA. The distribution of $R_{12,max}(t)$ for all realizations of the 163 red beads is shown on the right hand side of **Figure 4.9**. To accurately determine the fraction of bound beads (two-color doublets), we set the median collocation threshold to 0.65 and filtered out particle matches with intensity lower than 1 standard deviation from the mean of green particle matches. The black shaded region of the PDF is associated with the bound and the grey shaded region is associated with the unbound beads. The appropriateness of this collocation threshold is corroborated by the distinct difference

between the bound (solid) and unbound (dashed) collocation traces. Each of the bound traces has a high mean (and high median) value in time with a narrow variance, indicating deterministically correlated binding events. Meanwhile, the low mean (and low median) value and large variance of unbound collocation traces indicate random, weakly correlated events, such as those associated with image noise or close proximity of a neighboring bead.
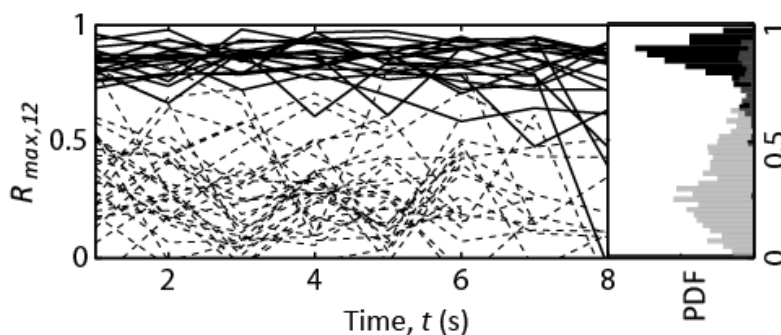
Figure 4.9. Measured normalized cross-covariance coefficients between Ch1 and Ch2 particle images of a bead suspension containing two sets of oligo-conjugated polystyrene beads (one red and one green) in the presence of complimentary DNA. The plot shows 50 representative traces (20 of them were judged as bound by the algorithm). The PDF of the covariance coefficients are plotted on the right hand side of the trace plot. The collocation traces of the bound red beads (solid black) remain relatively high during the 8 s of monitoring time, indicating deterministic interaction between Ch1 and Ch2 beads.

4.4.2 Cytometry-like fluorescence data

Integrated bead fluorescence were collected and analyzed to yield cytometry-like data. We identified and tracked beads in Ch1 and performed collocation analysis with Ch2 beads. The algorithm was then run again, but starting by identifying and tracking beads in Ch2 and collocating these with beads in Ch1. This process helps corroborate collocation information and helps reduce the effect of bead images which may fail threshold tests associated with particle tracking but not collocation analysis.

105

In **Figure 4.10**, we show the results of these two approaches overlaid on a scatter plot for two bead experiments (one negative control, and one containing target DNA). The fluorescent intensity of each bead was evaluated by integrating the intensity profile obtained from the non-linear Gaussian fitting routine. In the PMC-PC phase, we set the size-based threshold to eliminate beads with radii larger than the mean plus 1 times the standard deviation of the bead population in each image. The intensity-based threshold eliminated all features with intensity 1 times the standard deviation away from the mean of the bead population.

By performing PITC analysis twice starting with alternate image channels, we obtained the intensity distribution of both Ch1 and Ch2 beads independently. These distributions were used to calibrate the intensity-based filters of the collocation phase.

We set the median threshold, $\tilde{R}_{12}$ to 0.65 and monitored the bead intensities and collocation for 5 s which is approximately 2 times longer than the characteristic evolution time, tch. In **Figure 4.10**, we plot the mean intensity of each beads. For the 200 s duration of this experiment, the PITC counted total of 7903 (1010) red and 9351 (1292) green beads in the DNA-containing solution, and 7641 (1127) red and 9966 (1163) green beads for the negative control solution. In parenthesis, we note the number of beads that were tracked for 5 s or longer. In the solution containing DNA, the PITC algorithm detected 418 red beads collocated with green (R-G, blue markers), and 430 green beads collocated with red (G-R, purple markers).

In the negative control case, PITC detected 9 red beads collocated with green (R-G, blue markers), and 19 green beads collocated with red (G-R, purple markers). Visual

106

inspection of the particle field revealed that a small fraction of beads did form two-color bead hybrids. We hypothesize that this is a result of DNA contamination and/or non-specific bead-to-bead binding.
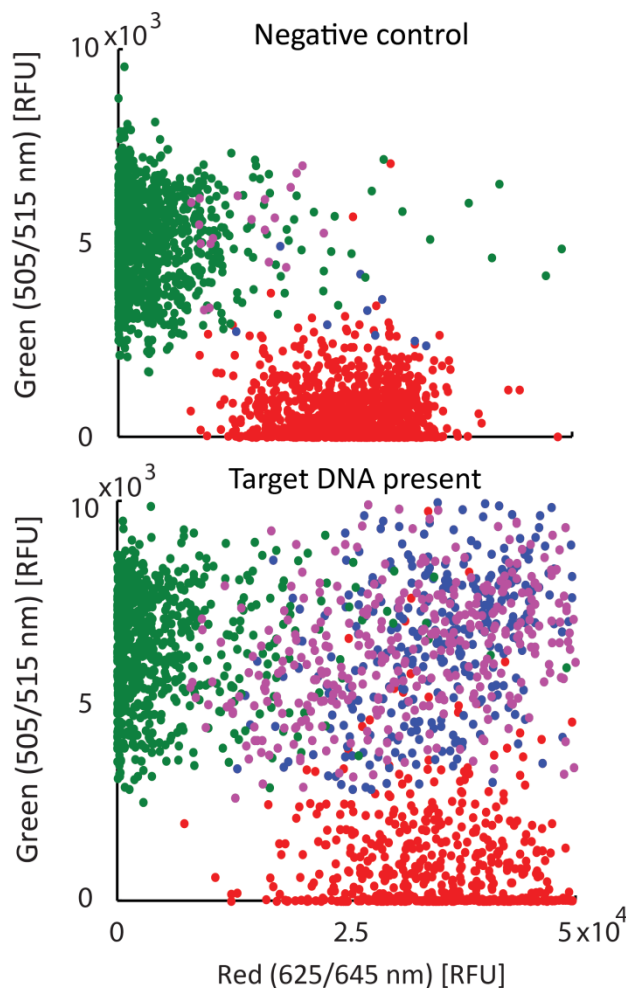
Figure 4.10. Multicolor bead hybrid fluorescence in a DNA-induced bead-to-bead binding assay. Algorithm parameters were set to $t_m / t_{ch} \cong 2$ and $\tilde{R}_{ID,co} = 0.65$. Here we show overlaid results of two particle tracking approaches. In first approach, red beads were tracked and cross-correlated with green channel. In the second approach, green beads were tracked and cross-correlated with red channel. The green and red markers correspond to green and red fluorescent bead singlets. The purple subpopulations on the scatter plot represent the green beads that were judged by the algorithm as collocated with the red beads (G-R). The blue subpopulation was obtained with the second approach (R-G). When DNA is present in the bead suspension, 33% of red and 41% of green beads were judged as bound. In the absence of DNA, 0.8% of red and 1.6% of green beads were judged as deterministically bound.

5 Conclusions, contributions, and recommendations

In this chapter, we summarize the main conclusions and major achievements of the work presented in this dissertation. We also present recommendations for future work, including ideas for significant extensions of the current work. Sections 4.1 through 4.3 respectively describe the major conclusions, contributions, and recommendations of our work on (1) bacterial RNA extraction and purification from whole human blood using ITP, (2) temperature effects on electrophoresis and (3) particle tracking and multispectral collocation method for particle-to-particle binding assays.

5.1 Summary of conclusions

5.1.1 Bacterial RNA Extraction and Purification from Whole Human Blood Using Isotachophoresis

1. Alkali-based lysing is well compatible with ITP extraction chemistry. ITP-based extraction and purification was shown efficacious for 16S rRNA from Pseudomonas Putida bacteria suspended in whole human blood.

2. The assay can be implemented with minimal manual steps and can automate the extraction, preconcentration, and purification of nucleic acid in less than 5 min.

3. RNA is easily hydrolyzed at elevated temperature, and at either alkali or acidic conditions. Further, its stability is significantly compromised by the abundance of RNases in blood. We showed that a novel ITP and PCR compatible chemistry

which ensures RNA stability and recovery using the addition of DTT, a strong reducing agent, and large amounts of polyA carrier RNA.

4. We showed that the extracted 16S rRNA was purified of PCR inhibitors and compatible with RT-qPCR. We demonstrated a sensitivity of 0.03 bacteria per nanoliter of blood, and hypothesize our sensitivity is currently limited by the presence of RNA contaminants in our reagents.

5.1.2 *Temperature Effects on Electrophoresis*

1. Our approach of including the effects of (1) viscosity, (2) ionic strength, (3) degree of ionization (pK), and (4) ion solvation effects on mobility, led to an electrolyte solution simulation tool which predicts the effects of temperature on ion mobility, solution pH, and solution conductivity.

2. We measured the temperature dependence of conductivity and pH in detail for ten electrolyte solutions. For temperatures between 20°C and 70°C, our electrolyte simulation tool was able to accurately predict conductivity and pH within 4% and ~ 0.2 pH units, respectively.

3. The model included a treatment of key phenomena, such that experimental validation was possible across a wide range of buffers including Tris-HCl, and enthanolamine-borate. In the case of Tris-HCl, we found that the non-viscosity related temperature dependence is due to the change in the hydration shell of the chloride ion. Whereas the temperature dependence of enthanolamine-borate conductivity and pH is dominated by the change in the degree of ionization of its constituent weak electrolyte ions.

4. The model predictions show and experiments confirm temperature sensitivity of electrolyte solution pH, and the clear presence of non-viscosity related temperature effects on conductivity.

5. For some electrolytes, the temperature induced reduction in degree of ionization strongly compensates for decreases in water viscosity, resulting in moderate conductivity increases (and even local maxima) with increasing temperature. For other electrolyte solutions, viscosity remains the dominant source of temperature dependence of conductivity, but pH can still vary significantly.

6. Walden's rule alone can lead to large errors. For example, Walden's rule yields 75% error for 20 mM ethanolamine and 20 mM boric acid solution, and 30% error for 30 mM Tris and 30mM HEPES solution conductivities.

5.1.3 Particle Tracking and Multispectral Collocation Method for Cytometry-Like and Particle-to-Particle Binding Assays

1. A custom algorithm which identifies, and tracks particle parameters was shown by simulations and experiments to capture cytometry-like data and particle collocation data for thousands of particles, using a relatively simple experiment. The data included size, intensity and collocation with other wavelengths.

2. Algorithm validation via Monte Carlo simulations of particle images at various image SNR and particle densities demonstrated that the algorithm can be relatively robust with just a few user-specified parameters. Analyses suggest that the optimum algorithm performance is achieved for SNR > 5 and inter-particle distance of $L_{IP} > 3\ L_{ch}$. For particle-to-particle collocation we recommend multiple realizations through monitoring times of $t_m > 2\ t_{ch}$.

3. The collocation algorithm and imaging technique was demonstrated as a method for quantifying DNA target identification by flowing oligonucleotide functionalized fluorescent bead populations in the presence of DNA targets to induce bead-to-bead binding. The algorithm was able to identify thousands of unique beads, over 1000 of which were monitored for 5 s or longer. Time-resolved fluorescent intensity and collocation with other channels were obtained and analyzed for detection of the target molecule. We found that in positive control experiments, over 400 of each bead set (~40%) participated in a bead-DNA-bead hybrid. In the negative control, the number of beads identified as collocated with another color was roughly 1%.

4. Out method has capabilities beyond those offered by conventional flow cytometry (FCM). For example, unlike FCM, our method obtains multiple realization of the same particle, so we can monitor kinetic events (e.g.: time evolution of particle intensity, size, or collocation) Furthermore, we do not require precise hydrodynamic focusing, or significant particle/cell dilution (we can operate with 10^8 particles/mL).

5.2 Summary of major contributions

5.2.1 Bacterial RNA Extraction and Purification from Whole Human Blood Using Isotachophoresis

1. Development of ITP compatible lysing chemistry enabling RNA isolation from ribonuclease- (RNase) rich samples such as biological fluids and cell-free suspensions (e.g., whole blood).

2. Optimization of RNA extraction protocol to be performed entirely in aqueous solution. Lysing chemistry is directly compatible with downstream transduction methods, including but not limited to enzymatic- (reverse-transcription (RT), polymerase chain reaction (PCR, ligation, etc.) and hybridization-based (e.g., RNA microarray chips) assays.

3. Integration and automation of RNA extraction protocol with ITP-based purification, and on-chip RNA detection.

4. Extraction and purification of bacterial RNA from whole human blood. Demonstration of compatibility with reverse transcription-quantitative polymerase chain reaction (RT-qPCR).

5. Demonstration of clinically relevant sensitivity of 0.03 bacteria per nanoliter blood using RT-qPCR.

5.2.2 *Temperature Effects on Electrophoresis*

1. Development of model capturing the important contributors to the effects of temperature on the observable electrophoretic mobilities of small ions, and on solution conductivity and pH. Model includes temperature effects on viscosity, ionic strength corrections, degree of ionization (pK), and ion solvation. Specifically, the model includes thermophysical data of the temperature dependence of the water viscosity; the temperature dependence of the Onsager-Fuoss model for finite ionic strength effects on mobility; the temperature dependence of the extended Debye-Huckel theory for correction of ionic activity; the Clarke-Glew generalized approach to predict the acid dissociation constant, pK, from tabulated thermodynamic properties; and species-specific, empirically

112

evaluated correction terms for temperature-dependence of Stokes' radii of 11 common small ions.

2. Development of free, open source MATLAB-based simulation tool named Simulation of Temperature Effects on ElectroPhoresis (STEEP).

3. Experimental validation of STEEP using conductance and pH measurements across a temperature variation of 25°C to 70°C for a set of electrolytes routinely used in electrophoresis.

5.2.3 *Particle Tracking and Multispectral Collocation Method for Cytometry-Like and Particle-to-Particle Binding Assays*

1. Development of particle imaging, tracking and collocation (PITC) algorithm applicable for analysis of either single images or time-resolved and spectrally-separated images of the motion of randomly distributed particles.

2. Optimization and validation of PITC algorithm parameters using Monte Carlo simulations. This study showed that our PITC algorithm is robust given sufficient image SNR (SNR>5) even at high particle densities (10^8 /mL). For example, we have shown that we can track thousands of particles, and collect time-resolved multiparametric data in less than 5 min.

3. Demonstrated high throughput capability. For applications requiring a single realization per particle, our method can produce particle size and multispectral intensity data for roughly 100-200 particles per realization, where the frequency of data capture is limited by CCD camera readout rates. With our setup (readout time: 35 ms, exposure time: 5 s), this translates to 120,000-240,000 particle scans per minute.

4. Experimental demonstration of the tracking and collocation method on challenging image data, including flow of randomly distributed Brownian bead populations which undergo bead-to-bead binding induced by hybridization to 16S rRNA gene.

5.3 Recommendations for future work

5.3.1 Bacterial RNA Extraction and Purification from Whole Human Blood Using Isotachophoresis

1. In order to improve sensitivity, and ease of use, we can envision a disposable plastic chip that can be discarded after each use, largely mitigating decontamination and obviating surface re-conditioning procedures.

2. With the current channel design, we expect, at most, 2 orders of magnitude improvement in sensitivity by addressing the presence of RNA contaminants in our reagents. To achieve higher sensitivity, our method will likely require redesign of chip geometry to achieve higher extraction efficiency and to accommodate processing of larger sample volumes. We hypothesize that, given sufficient sample capacity, our RNA extraction method can be made compatible with DNA or RNA chips, perhaps without the need for nucleic acid amplification.

5.3.2 Temperature Effects on Electrophoresis

1. Modification of SPRESSO, a free, open-source MATLAB-based nonlinear electrophoresis solver, to account for temperature effects could enable more complex, and ad hoc separation optimizations which can accurately capture electromigration dispersion and so-called system zones at elevated temperature.

2. To simulate the effect of externally imposed axial and radial temperature gradients on electrophoretic separations and focusing, we recommend performing temperature-dependent calculations at every grid point in the domain.

3. Further enhancement of the simulation capabilities can be achieved by iterative computation of the Joule heating induced changes in conductivity and corresponding changes in local temperature.

5.3.3 *Particle Tracking and Multispectral Collocation Method for Cytometry-Like and Particle-to-Particle Binding Assays*

1. The particle tracking phase of the algorithm (KC-PTV) can be further refined by including other particle parameters in the χ^2-test. For example, the accuracy of particle matches can be improved by including particle shape, orientation (angle), and complexity (intensity distribution), in addition to coordinates and size among the χ^2-test criteria.

2. While we have optimized and demonstrated this method for challenging image data of particle-to-particle binding assays, we note that this method is equally applicable for assays where particles are not expected to interact. For instance, our method can be applied for rapid cell-based diagnostics (e.g., TB and malaria)[168] or for 2-4 color immunophenotyping assays.[173]

3. This method is particularly appealing as it lends itself to the efforts of cost reduction for cell enumeration technologies (e.g., see Mandy et al.[181] for discussion of affordable CD4+ T-cell enumeration). One affordable option is to sequentially trigger each wavelength of a four-color high power Thorlabs LED source $5k (price includes driver and modulation input) and collect images at a

fixed time offset. Alternatively one can use an emission splitter devices (as we have done so in this study) which can costs $8k (2-color Cairn Optosplit II image splitter and cube) up to $19k (4-color Photometrics Quad-View 2 System).

4. We have demonstrated that we can detect the presence of nucleic acids indirectly by monitoring bead-to-bead binding. We recommend exploring the limit of detection of molecular biomarkers (proteins, RNA and DNA), and evaluating weather this method can achieve a clinically relevant sensitivity required for diagnostic purposes.

116

6 Bibliography

[1]   Farrell, R.E., "RNA methodologies: A laboratory guide for isolation and characterization". 4 ed. **2010**, San Diego, CA: Academic Press, Inc.

[2]   Wellinghausen, N., et al., "Diagnosis of bacteremia in whole-blood samples by use of a commercial universal 16S rRNA gene-based PCR and sequence analysis"*, Journal of clinical microbiology, **2009**, 47 (9), 2759-2765.

[3]   Zhang, Y., et al., "Detection of Streptococcus pneumoniae in whole blood by PCR"*, Journal of clinical microbiology, **1995**, 33 (3), 596-601.

[4]   Marck, C. and H. Grosjean, "tRNomics: Analysis of tRNA genes from 50 genomes of Eukarya, Archaea, and Bacteria reveals anticodon-sparing strategies and domain-specific features"*, Rna-a Publication of the Rna Society, **2002**, 8 (10), 1189-1232.

[5]   Alberts, B., et al., "Molecular biology of the cell 4th edition". **2002**: Garland Science, a Taylor & Francis Group.

[6]   Satterfield, B.C., et al., "Microfluidic Purification and Preconcentration of mRNA by Flow-Through Polymeric Monolith"*, Analytical Chemistry, **2007**, 79 (16), 6230-6235.

[7]   Lowery, A.J., et al., "MicroRNAs as Prognostic Indicators and Therapeutic Targets: Potential Effect on Breast Cancer Management"*, Clinical Cancer Research, **2008**, 14 (2), 360-365.

[8]   Dheda, K., et al., "Validation of housekeeping genes for normalizing RNA expression in real-time PCR"*, Biotechniques, **2004**, 37, 112-119.

[9]   He, L. and G.J. Hannon, "MicroRNAs: small RNAs with a big role in gene regulation"*, Nature Reviews Genetics, **2004**, 5 (7), 522-531.

[10]   Mueller, O., S. Lightfoot, and A. Schroder, "RNA Integrity Number (RIN) Standardization of RNA Quality Control"*, Tech. Rep. 5989-1165EN, Agilent Technologies, Application Note, **2004**.

[11]   Schroeder, A., et al., "The RIN: an RNA integrity number for assigning integrity values to RNA measurements"*, BMC Molecular Biology, **2006**, 7 (1), 3.

[12]   Tsui, N.B.Y., E.K.O. Ng, and Y.M.D. Lo, "Stability of Endogenous and Added RNA in Blood Specimens, Serum, and Plasma"*, Clinical Chemistry, **2002**, 48 (10), 1647-1653.

[13]   Cox, R., H.J. Gould, and K. Kanagalingam, "A study of the alkaline hydrolysis of fractionated reticulocyte ribosomal ribonucleic acid and its relevance to secondary structure"*, Biochemical Journal, **1968**, 106 (3), 733.

[14]   Lipkin, D., P.T. Talbert, and M. Cohn, "The Mechanism of the Alkaline Hydrolysis of Ribonucleic Acids"*, Journal of the American Chemical Society, **1954**, 76 (11), 2871-2872.

[15]   Wang, H., R.A. Ach, and B. Curry, "Direct and sensitive miRNA profiling from low-input total RNA"*, RNA, **2007**, 13 (1), 151-159.

118

[16]   Dunbar, S.A., "Applications of Luminex® xMAP™ technology for rapid, high-throughput multiplexed nucleic acid detection"*, Clinica Chimica Acta*, **2006**, 363 (1–2), 71-82.

[17]   Xu, R.N., et al., "Recent advances in high-throughput quantitative bioanalysis by LC–MS/MS"*, Journal of Pharmaceutical and Biomedical Analysis*, **2007**, 44 (2), 342-355.

[18]   Toner, M. and D. Irimia, "BLOOD-ON-A-CHIP"*, Annual Review of Biomedical Engineering*, **2005**, 7 (1), 77-103.

[19]   Johansson, M.A. and K.-E. Hellenäs, "Matrix effects in immunobiosensor determination of clenbuterol in urine and serum"*, Analyst*, **2004**, 129 (5), 438-442.

[20]   Chambers, E., et al., "Systematic and comprehensive strategy for reducing matrix effects in LC/MS/MS analyses"*, Journal of chromatography. B, Analytical technologies in the biomedical and life sciences*, **2007**, 852 (1-2), 22-34.

[21]   Chiu, M.L., et al., "Matrix Effects—A Challenge Toward Automation of Molecular Analysis"*, JALA*, **2010**, 15 (3), 233-242.

[22]   Lagally, E.T., et al., "Integrated Portable Genetic Analysis Microsystem for Pathogen/Infectious Disease Detection"*, Analytical Chemistry*, **2004**, 76 (11), 3162-3170.

[23]   Peytavi, R., et al., "Microfluidic Device for Rapid (<15 min) Automated

Microarray Hybridization", Clin Chem, **2005**, 51 (10), 1836-1844.

[24]   Grob, R.L., "Sample Preparation Techniques Used for Gas Chromatography",

Retrieved from http://www.restek.com/Technical-Resources/Technical-

Library/Editorial/editorial_A005.

[25]   Mariella, R., "Sample preparation: the weak link in microfluidics-based

biodetection", Biomedical Microdevices, **2008**, 10 (6), 777-784.

[26]   Chomczynski, P. and N. Sacchi, "Single-step method of RNA isolation by acid

guanidinium thiocyanate-phenol-chloroform extraction", Analytical

Biochemistry, **1987**, 162 (1), 156-159.

[27]   Arthur, C.L. and J. Pawliszyn, "Solid phase microextraction with thermal

desorption using fused silica optical fibers", Analytical Chemistry, **1990**, 62 (19),

2145-2148.

[28]   Wen, J., et al., "Purification of Nucleic Acids in Microfluidic Devices",

Analytical Chemistry, **2008**, 80 (17), 6472-6479.

[29]   Uhlen, M., "Magnetic separation of DNA", Nature, **1989**, 340 (6236), 733-734.

[30]   Lee, J.-H., et al., "Comparisons of Three Automated Systems for Genomic DNA

Extraction in a Clinical Diagnostic Laboratory", Yonsei Med J, **2010**, 51 (1), 104-

110.

120

[31]   Breadmore, M.C., et al., "Microchip-Based Purification of DNA from Biological Samples"*, Analytical Chemistry*, **2003**, 75 (8), 1880-1886.

[32]   Legendre, L.A., et al., "A Simple, Valveless Microfluidic Sample Preparation Device for Extraction and Amplification of DNA from Nanoliter-Volume Samples"*, Analytical Chemistry*, **2006**, 78 (5), 1444-1451.

[33]   Root, B.E., et al., "Purification of HIV RNA from Serum Using a Polymer Capture Matrix in a Microfluidic Device"*, Analytical Chemistry*, **2011**, 83 (3), 982-988.

[34]   Witek, M.A., et al., "96-Well Polycarbonate-Based Microfluidic Titer Plate for High-Throughput Purification of DNA and RNA"*, Analytical Chemistry*, **2008**, 80 (9), 3483-3491.

[35]   Bhattacharyya, A. and C.M. Klapperich, "Microfluidics-based extraction of viral RNA from infected mammalian cells for disposable molecular diagnostics"*, Sensors and Actuators B: Chemical*, **2008**, 129 (2), 693-698.

[36]   Jiang, G. and D.J. Harrison, "mRNA isolation in a microfluidic device for eventual integration of cDNA library construction"*, Analyst*, **2000**, 125 (12).

[37]   Hong, J.W., et al., "A nanoliter-scale nucleic acid processor with parallel architecture"*, Nat Biotech*, **2004**, 22 (4), 435-439.

[38]   Hagan, K.A., et al., "Microchip-Based Solid-Phase Purification of RNA from Biological Samples"*, Analytical Chemistry*, **2008**, 80 (22), 8453-8460.

[39]   Hagan, K.A., et al., "Chitosan-Coated Silica as a Solid Phase for RNA
         Purification in a Microfluidic Device", Analytical Chemistry, **2009**, 81 (13),
         5249-5256.

[40]   Garcia-Schwarz, G., et al., "On-chip Isotachophoresis for Separation of Ions and
         Purification of Nucleic Acids", J Vis Exp, **2012** (61), e3890.

[41]   Jung, B., R. Bharadwaj, and J.G. Santiago, "On-Chip Millionfold Sample
         Stacking Using Transient Isotachophoresis", Analytical Chemistry, **2006**, 78 (7),
         2319-2327.

[42]   Khurana, T.K. and J.G. Santiago, "Sample Zone Dynamics in Peak Mode
         Isotachophoresis", Analytical Chemistry, **2008**, 80 (16), 6300-6307.

[43]   Bercovici, M., et al., "Rapid hybridization of nucleic acids using
         isotachophoresis", Proc. Natl. Acad. Sci., **2012**, 109 (28), 11127-11132.

[44]   Manual, W.E., "Worthington Biochemical Corp". Freehold, NJ. Vol. 43. **1972**.

[45]   "Reverse Transcriptase Enzymes", 2013; Available from:
         http://www.invitrogen.com/site/us/en/home/Products-and-
         Services/Applications/PCR/reverse-transcription/reverse-transcriptase-
         enzymes.html.

[46]   Wetmur, J.G. and J. Fresco, "DNA Probes: Applications of the Principles of
         Nucleic Acid Hybridization", Critical Reviews in Biochemistry and Molecular
         Biology, **1991**, 26 (3-4), 227-259.

[47]   Wetmur, J.G. and N. Davidson, "Kinetics of renaturation of DNA", *Journal of Molecular Biology*, **1968**, 31 (3), 349-370.

[48]   Wetmur, J.G., "Hybridization and Renaturation Kinetics of Nucleic Acids", *Annual Review of Biophysics and Bioengineering*, **1976**, 5 (1), 337-361.

[49]   Kestin, J., "Viscosity of Liquid Water in the Range—8 C to 150 C", *J. Phys. Chem. Ref. Data*, **1978**, 7 (3).

[50]   Liu, S., et al., "Optimization of High-Speed DNA Sequencing on Microfabricated Capillary Electrophoresis Channels", *Analytical Chemistry*, **1998**, 71 (3), 566-573.

[51]   Liang, D. and B. Chu, "High speed separation of DNA fragments by capillary electrophoresis in poly(ethylene oxide)-poly(propylene oxide)-poly(ethylene oxide) triblock polymer", *ELECTROPHORESIS*, **1998**, 19 (14), 2447-2453.

[52]   Zhang, J., et al., "Use of Non-Cross-Linked Polyacrylamide for Four-Color DNA Sequencing by Capillary Electrophoresis Separation of Fragments up to 640 Bases in Length in Two Hours", *Analytical Chemistry*, **1995**, 67 (24), 4589-4593.

[53]   Landers, J.P., "Handbook of capillary electrophoresis". 2 ed, ed. J.P. Landers. **2008**, Boca Raton, FL: CRC Press, Taylor and Francis Group, LLC 27-28.

[54]   Grushka, E., R.M. McCormick, and J.J. Kirkland, "Effect of temperature gradients on the efficiency of capillary zone electrophoresis separations", *Analytical Chemistry*, **1989**, 61 (3), 241-246.

[55]   Tang, G., et al., "Joule heating effect on electroosmotic flow and mass species transport in a microcapillary"*, International Journal of Heat and Mass Transfer*, **2004**, 47 (2), 215-227.

[56]   Petersen, N.J., et al., "Effect of Joule heating on efficiency and performance for microchip-based and capillary-based electrophoretic separation systems: A closer look"*, ELECTROPHORESIS, **2004**, 25 (2), 253-269.

[57]   Evenhuis, C.J., et al., "Temperature Profiles and Heat Dissipation in Capillary Electrophoresis"*, Analytical Chemistry, **2006**, 78 (8), 2684-2693.

[58]   Xuan, X., "Joule heating in electrokinetic flow"*, ELECTROPHORESIS, **2007**, 29 (1), 33-43.

[59]   Gaš, B. and E. Kenndler, "Dispersive phenomena in electromigration separation methods"*, ELECTROPHORESIS, **2000**, 21 (18), 3888-3897.

[60]   Štědrý, M., M. Jaroš, and B. Gaš, "Eigenmobilities in background electrolytes for capillary zone electrophoresis: I. System eigenpeaks and resonance in systems with strong electrolytes"*, Journal of Chromatography A, **2002**, 960 (1–2), 187-198.

[61]   Štědrý, M., et al., "Eigenmobilities in background electrolytes for capillary zone electrophoresis: III. Linear theory of electromigration"*, ELECTROPHORESIS, **2004**, 25 (18-19), 3071-3079.

[62]   Gaš, B. and E. Kenndler, "System zones in capillary zone electrophoresis", ELECTROPHORESIS, **2004**, 25 (23-24), 3901-3912.

[63]   Gebauer, P., J.L. Beckers, and P. Boček, "Theory of system zones in capillary zone electrophoresis", ELECTROPHORESIS, **2002**, 23 (12), 1779-1785.

[64]   Jaros, M., et al., "Optimization of background electrolytes for capillary electrophoresis: II. Computer simulation and comparison with experiments", ELECTROPHORESIS, **2002**, 23 (16), 2667-2677.

[65]   Hruška, V., M. Jaroš, and B. Gaš, "Simul 5 – Free dynamic simulator of electrophoresis", ELECTROPHORESIS, **2006**, 27 (5-6), 984-991.

[66]   Bahga, S.S., M. Bercovici, and J.G. Santiago, "Ionic strength effects on electrophoretic focusing and separations", ELECTROPHORESIS, **2010**, 31 (5), 910-919.

[67]   Bercovici, M., S.K. Lele, and J.G. Santiago, "Open source simulation tool for electrophoretic stacking, focusing, and separation", Journal of Chromatography A, **2009**, 1216 (6), 1008-1018.

[68]   Saiki, R.K., et al., "Primer-directed enzymatic amplification of DNA with a thermostable DNA polymerase", Science, **1988**, 239 (4839), 487-487.

[69]   Pickett, M.A., et al., "The plasmids of Chlamydia trachomatis and Chlamydophila pneumoniae (N16): accurate determination of copy number and the paradoxical effect of plasmid-curing agents", Microbiology, **2005**, 151 (3), 893-893.

[70]   Apfalter, P., et al., "Comparison of a new quantitative ompA-based real-time PCR

          TaqMan assay for detection of Chlamydia pneumoniae DNA in respiratory

          specimens with four conventional PCR assays"*, Journal of clinical microbiology,*

          2003, 41 (2), 592-592.

[71]   Weidmann, M., U. Meyer-Konig, and F.T. Hufert, "Rapid detection of herpes

          simplex virus and varicella-zoster virus infections by real-time PCR"*, Journal of

          clinical microbiology,* **2003**, 41 (4), 1565-1565.

[72]   Al-Soud, W.A. and P. Rådström, "Purification and Characterization of PCR-

          Inhibitory Components in Blood Cells"*, Journal of Clinical Microbiology,* **2001**,

          39 (2), 485-493.

[73]   Al-Soud, W.A. and P. Rådström, "Effects of amplification facilitators on

          diagnostic PCR in the presence of blood, feces, and meat"*, Journal of Clinical

          Microbiology,* **2000**, 38 (12), 4463-4470.

[74]   Wagner, A., et al., "Surveys of Gene Families Using Polymerase Chain Reaction:

          PCR Selection and PCR Drift"*, Systematic Biology,* **1994**, 43 (2), 250-261.

[75]   Multer, G.L. and K.A. Boynton, "PCR bias in amplification of androgen receptor

          alleles, a trinucleotide repeat marker used in clonality studies"*, Nucleic Acids

          Research,* **1995**, 23 (8), 1411-1418.

[76]   Markoulatos, P., N. Siafakas, and M. Moncany, "Multiplex polymerase chain

          reaction: A practical approach"*, Journal of Clinical Laboratory Analysis,* **2002**, 16

          (1), 47-51.

126

[77]   Voelkerding, K.V., S.A. Dames, and J.D. Durtschi, "Next-generation sequencing: from basic research to diagnostics", Clinical chemistry, **2009**, 55 (4), 641-641.

[78]   Ozsolak, F., et al., "Amplification-free digital gene expression profiling from minute cell quantities", Nature methods, **2010**, 7 (8), 619-621.

[79]   Metzker, M.L., "Sequencing technologies—the next generation", Nature Reviews Genetics, **2009**, 11 (1), 31-46.

[80]   Liao, J.C., et al., "Use of electrochemical DNA biosensors for rapid molecular identification of uropathogens in clinical urine specimens", Journal of clinical microbiology, **2006**, 44 (2), 561-561.

[81]   Xu, L., et al., "Giant magnetoresistive biochip for DNA detection and HPV genotyping", Biosensors and Bioelectronics, **2008**, 24 (1), 99-103.

[82]   Heller, M.J., "DNA MICROARRAY TECHNOLOGY: Devices, Systems, and Applications", Annual Review of Biomedical Engineering, **2002**, 4 (1), 129-153.

[83]   Templin, M.F., et al., "Protein microarray technology", Trends in Biotechnology, **2002**, 20 (4), 160-166.

[84]   Squires, T.M., R.J. Messinger, and S.R. Manalis, "Making it stick: convection, reaction and diffusion in surface-based biosensors", Nature biotechnology, **2008**, 26 (4), 417-426.

[85]   Minichino, C., "FY07 Engineering Research and Technology Report", **2008**, Lawrence Livermore National Laboratory (LLNL), Livermore, CA.

127

[86]   Nam, J.-M., S.I. Stoeva, and C.A. Mirkin, "Bio-Bar-Code-Based DNA Detection with PCR-like Sensitivity", *Journal of the American Chemical Society*, **2004**, 126 (19), 5932-5933.

[87]   Leslie, D.C., et al., "New Detection Modality for Label-Free Quantification of DNA in Biological Samples via Superparamagnetic Bead Aggregation", *Journal of the American Chemical Society*, **2012**, 134 (12), 5689-5696.

[88]   Rogacs, A., Y. Qu, and J.G. Santiago, "Bacterial RNA Extraction and Purification from Whole Human Blood Using Isotachophoresis", *Analytical Chemistry*, **2012**, 84 (14), 5858-5863.

[89]   Matsuda, K., et al., "Sensitive Quantitative Detection of Commensal Bacteria by rRNA-Targeted Reverse Transcription-PCR", *Applied and Environmental Microbiology*, **2007**, 73 (1), 32-39.

[90]   Fujimori, M., et al., "Efficacy of bacterial ribosomal RNA-targeted reverse transcription-quantitative PCR for detecting neonatal sepsis: a case control study", *BMC pediatrics*, **2010**, 10 (1), 53.

[91]   Arfvidsson, C. and K.G. Wahlund, "Time-minimized determination of ribosome and tRNA levels in bacterial cells using flow field-flow fractionation", *Analytical Biochemistry*, **2003**, 313 (1), 76-85.

[92]   Neidhardt, F.C., "Escherichia coli and Salmonella". Vol. 1. **1996**: ASM Press

[93]   Kim, J., et al., "Microfluidic sample preparation: cell lysis and nucleic acid purification", Integrative Biology, **2009**, 1 (10), 574-586.

[94]   Markham, R. and J. Smith, "The structure of ribonucleic acids. 1. Cyclic nucleotides produced by ribonuclease and by alkaline hydrolysis", Biochemical Journal, **1952**, 52 (4), 552.

[95]   Mahalanabis, M., et al., "Cell lysis and DNA extraction of gram-positive and gram-negative bacteria from whole blood in a disposable microfluidic chip", Lab on a Chip, **2009**, 9 (19), 2811-2817.

[96]   Jung, B., Y. Zhu, and J.G. Santiago, "Detection of 100 aM Fluorophores Using a High-Sensitivity On-Chip CE System and Transient Isotachophoresis", Analytical Chemistry, **2006**, 79 (1), 345-349.

[97]   Bahga, S.S., et al., "High-sensitivity detection using isotachophoresis with variable cross-section geometry", ELECTROPHORESIS, **2011**, 32 (5), 563-572.

[98]   Boček, P., "Analytical isotachophoresis", **1981**, Springer Berlin / Heidelberg. 131-177.

[99]   Schoch, R.B., M. Ronaghi, and J.G. Santiago, "Rapid and selective extraction, isolation, preconcentration, and quantitation of small RNAs from cell lysate using on-chip isotachophoresis", Lab on a Chip, **2009**, 9 (15), 2145-2152.

[100]   Persat, A., et al., "Quantification of Global MicroRNA Abundance by Selective Isotachophoresis", Analytical Chemistry, **2010**, 82 (23), 9631-9635.

[101]   Persat, A. and J.G. Santiago, "MicroRNA Profiling by Simultaneous Selective Isotachophoresis and Hybridization with Molecular Beacons"*, Analytical Chemistry*, **2011**, 83 (6), 2310-2316.

[102]   Persat, A., L.A. Marshall, and J.G. Santiago, "Purification of Nucleic Acids from Whole Blood Using Isotachophoresis"*, Analytical Chemistry*, **2009**, 81 (22), 9507-9511.

[103]   Marshall, L.A., C.M. Han, and J.G. Santiago, "Extraction of DNA from Malaria-Infected Erythrocytes Using Isotachophoresis"*, Analytical Chemistry*, **2011**, 83 (24), 9715-9718.

[104]   Bercovici, M., et al., "Rapid Detection of Urinary Tract Infections Using Isotachophoresis and Molecular Beacons"*, Analytical Chemistry*, **2011**, 83 (11), 4110-4117.

[105]   Heptinstall, J., "Total RNA Isolation from Bacteria:The Nucleic Acid Protocols Handbook", R. Rapley, Editor, **2000**, Humana Press. 47-52.

[106]   Bimboim, H. and J. Doly, "A rapid alkaline extraction procedure for screening recombinant plasmid DNA"*, Nucleic acids research*, **1979**, 7 (6), 1513-1523.

[107]   Freitas, S., et al., "On the stability of plasmid DNA vectors during cell culture and purification"*, Molecular Biotechnology*, **2007**, 36 (2), 151-158.

[108]   Florence, T.M., "Degradation of protein disulphide bonds in dilute alkali"*, Biochemical Journal*, **1980**, 189 (3), 507.

130

[109]   Lu, B.-Y. and J.-Y. Chang, "Rapid and irreversible reduction of protein disulfide bonds", Analytical Biochemistry, **2010**, 405 (1), 67-72.

[110]   Chomczynski, P., "Solubilzation in formamide protects RNA from degradation", Nucleic Acids Research, **1992**, 20 (14), 3791-3792.

[111]   Strauss Jr, J.H. and R.L. Sinsheimer, "Initial kinetics of degradation of MS2 ribonucleic acid by ribonuclease, heat and alkali and the presence of configurational restraints in this ribonucleic acid", Journal of Molecular Biology, **1968**, 34 (3), 453-465.

[112]   Winslow, S.G. and P.A. Henkart, "Polyinosinlc acid as a carrier in the microscale purification of total RNA", Nucleic Acids Research, **1991**, 19 (12), 3251-3253.

[113]   Gallagher, M.L., W.F. Burke Jr, and K. Orzech, "Carrier RNA enhancement of recovery of DNA from dilute solutions", Biochemical and Biophysical Research Communications, **1987**, 144 (1), 271-276.

[114]   Rio, D.C., et al., "Ethanol Precipitation of RNA and the Use of Carriers", Cold Spring Harbor Protocols, **2010**, 2010 (6).

[115]   Shaw, K.J., et al., "The use of carrier RNA to enhance DNA extraction from microfluidic-based silica monoliths", Analytica Chimica Acta, **2009**, 652 (1–2), 231-233.

[116]   Doherty, E.A.S., et al., "Microchannel wall coatings for protein separations by capillary and chip electrophoresis", ELECTROPHORESIS, **2003**, 24 (1-2), 34-54.

[117] McCormick, R.M., "Capillary zone electrophoretic separation of peptides and proteins using low pH buffers in modified silica capillaries"*, Analytical Chemistry*, **1988**, 60 (21), 2322-2328.

[118] Darton, T., et al., "Severity of Meningococcal Disease Associated with Genomic Bacterial Load"*, Clinical Infectious Diseases*, **2009**, 48 (5), 587-594.

[119] Hackett, S.J., et al., "Meningococcal bacterial DNA load at presentation correlates with disease severity"*, Archives of Disease in Childhood*, **2002**, 86 (1), 44-46.

[120] Rogacs, A. and J.G. Santiago, "Temperature Effects on Electrophoresis"*, Analytical Chemistry*, **2013**, 85 (10), 5103-5113.

[121] Kelly, L. and R.J. Nelson, "Capillary Zone Electrophoresis of Organic Acids and Anions"*, Journal of Liquid Chromatography*, **1993**, 16 (9-10), 2103-2112.

[122] Smith, S.C. and M.G. Khaledi, "Optimization of pH for the separation of organic acids in capillary zone electrophoresis"*, Analytical Chemistry*, **1993**, 65 (3), 193-198.

[123] Lin, C.-E., C.-C. Chang, and W.-C. Lin, "Migration behavior and separation of sulfonamides in capillary zone electrophoresis III. Citrate buffer as a background electrolyte"*, Journal of Chromatography A*, **1997**, 768 (1), 105-112.

[124] Rasmussen, H.T. and H.M. McNair, "Influence of buffer concentration, capillary internal diameter and forced convection on resolution in capillary zone electrophoresis"*, Journal of Chromatography A*, **1990**, 516 (1), 223-231.

[125]   Hoffstetter-Kuhn, S., et al., "Influence of borate complexation on the electrophoretic behavior of carbohydrates in capillary electrophoresis"*, Analytical Chemistry,* **1991**, 63 (15), 1541-1547.

[126]   Whang, C.W. and E.S. Yeung, "Temperature programming in capillary zone electrophoresis"*, Analytical Chemistry,* **1992**, 64 (5), 502-506.

[127]   Chang, H.-T. and E.S. Yeung, "Voltage programming in capillary zone electrophoresis"*, Journal of Chromatography A,* **1993**, 632 (1–2), 149-155.

[128]   Nübel, U., et al., "Sequence heterogeneities of genes encoding 16S rRNAs in Paenibacillus polymyxa detected by temperature gradient gel electrophoresis"*, Journal of Bacteriology,* **1996**, 178 (19), 5636-43.

[129]   Rush, R.S., A.S. Cohen, and B.L. Karger, "Influence of column temperature on the electrophoretic behavior of myoglobin and .alpha.-lactalbumin in high-performance capillary electrophoresis"*, Analytical Chemistry,* **1991**, 63 (14), 1346-1350.

[130]   Rochu, D., G. Ducret, and P. Masson, "Measuring conformational stability of proteins using an optimized temperature-controlled capillary electrophoresis approach"*, Journal of Chromatography A,* **1999**, 838 (1–2), 157-165.

[131]   Ross, D. and L.E. Locascio, "Microfluidic Temperature Gradient Focusing"*, Analytical Chemistry,* **2002**, 74 (11), 2556-2564.

[132] Shackman, J.G., et al., "Quantitative temperature gradient focusing performed using background electrolytes at various pH values"*, ELECTROPHORESIS, **2006**, 27 (17), 3420-3427.

[133] Ghosal, S. and Z. Chen, "Nonlinear Waves in Capillary Electrophoresis"*, Bulletin of Mathematical Biology, **2010**, 72 (8), 2047-2066.

[134] Nightingale, E.R., "Phenomenological Theory of Ion Solvation. Effective Radii of Hydrated Ions"*, The Journal of Physical Chemistry, **1959**, 63 (9), 1381-1387.

[135] Evenhuis, C.J., et al., "Reliable electrophoretic mobilities free from Joule heating effects using CE"*, ELECTROPHORESIS, **2007**, 28 (20), 3759-3766.

[136] Okamoto, H., et al., "Theory and computer programs for calculating solution pH, buffer formula, and buffer capacity for multiple component system at a given ionic strength and temperature"*, Pharmaceutical research, **1997**, 14 (3), 299-302.

[137] Anderko, A. and M.M. Lencka, "Computation of electrical conductivity of multicomponent aqueous systems in wide concentration and temperature ranges"*, Industrial & engineering chemistry research, **1997**, 36 (5), 1932-1943.

[138] Clancy, M.J., "The formulation of buffers and media for enzyme histochemistry"*, The Histochemical Journal, **1987**, 19 (1), 27-34.

[139] Beynon, R.J. and J.S. Easterby, "Buffer solutions". **1996**: IRL Press at Oxford University Press Oxford, UK.

[140] Fukada, H. and K. Takahashi, "Enthalpy and heat capacity changes for the proton dissociation of various buffer components in 0.1 M potassium chloride"*, Proteins: Structure, Function, and Bioinformatics, **1998**, 33 (2), 159-166.

[141] Wang, C.-K. and H.-K. Tsao, "Temperature-Insensitive Electrokinetic Behavior in Capillary Zone Electrophoresis"*, The Journal of Physical Chemistry B, **2004**, 108 (45), 17685-17693.

[142] Reijenga, J.C., L.G. Gagliardi, and E. Kenndler, "Temperature dependence of acidity constants, a tool to affect separation selectivity in capillary electrophoresis"*, Journal of Chromatography A, **2007**, 1155 (2), 142-145.

[143] Mandaji, M., et al., "Sample stacking in CZE using dynamic thermal junctions I. Analytes with low dpKa/dT crossing a single thermally induced pH junction in a BGE with high dpH/dT"*, ELECTROPHORESIS, **2009**, 30 (9), 1501-1509.

[144] Milanova, D., et al., "Electrophoretic mobility measurements of fluorescent dyes using on-chip capillary electrophoresis"*, ELECTROPHORESIS, **2011**, 32 (22), 3286-3294.

[145] Diekmann, S., "Temperature and salt dependence of the gel migration anomaly of curved DNA fragments"*, Nucleic Acids Research, **1987**, 15 (1), 247-265.

[146] Kan, C.W. and A.E. Barron, "A DNA sieving matrix with thermally tunable mesh size"*, ELECTROPHORESIS, **2003**, 24 (1-2), 55-62.

[147] Evenhuis, C.J., et al., "Variation of zeta-potential with temperature in fused-silica capillaries used for capillary electrophoresis", ELECTROPHORESIS, **2006**, 27 (3), 672-676.

[148] Onsager, L. and R.M. Fuoss, "Irreversible Processes in Electrolytes. Diffusion, Conductance and Viscous Flow in Arbitrary Mixtures of Strong Electrolytes", The Journal of Physical Chemistry, **1931**, 36 (11), 2689-2778.

[149] Grenthe, I. and H. Wanner, "TDB-2 Guidelines for the Extrapolation to Zero Ionic Strength; minor revisions by Osthols", **2000**, Erik.

[150] Debye, P. and E. Huckel, "The interionic attraction theory of deviations from ideal behavior in solution", Z. Phys, **1923**, 24, 185.

[151] Clarke, E.C.W. and D.N. Glew, "Evaluation of thermodynamic functions from equilibrium constants", Transactions of the Faraday Society, **1966**, 62 (0), 539-547.

[152] Goldberg, R.N., N. Kishore, and R.M. Lennen, "Thermodynamic quantities for the ionization reactions of buffers", Journal of Physical and Chemical Reference Data, **2002**, 31 (2), 231-370.

[153] Walden, P., H. Ulich, and G. Busch, "Leitfähigkeitsmessungen in aceton 1", Z. Phys. Chem, **1926**, 123, 429.

136

[154] Sadek, H., "Walden product, Stokes' law and water stucture: A critical review", Journal of Electroanalytical Chemistry and Interfacial Electrochemistry, **1983**, 144 (1–2), 11-32.

[155] Fernandez-Prini, R. and G. Atkinson, "Examination of the Zwanzig theory of dielectric friction. II", The Journal of Physical Chemistry, **1971**, 75 (2), 239-244.

[156] Jenkins, H.D.B. and Y. Marcus, "Viscosity B-Coefficients of Ions in Solution", Chemical Reviews, **1995**, 95 (8), 2695-2724.

[157] Porras, S.P., M.-L. Riekkola, and E. Kenndler, "The principles of migration and dispersion in capillary zone electrophoresis in nonaqueous solvents", ELECTROPHORESIS, **2003**, 24 (10), 1485-1498.

[158] Robinson, R.A. and R.H. Stokes, "Electrolyte solutions". 2nd Revised ed. **2002**, New York: Dover Publications.

[159] Persat, A., M.E. Suss, and J.G. Santiago, "Basic principles of electrolyte chemistry for microfluidic electrokinetics. Part II: Coupling between ion mobility, electrolysis, and acid-base equilibria", Lab on a Chip, **2009**, 9 (17), 2454-2469.

[160] Persat, A., R.D. Chambers, and J.G. Santiago, "Basic principles of electrolyte chemistry for microfluidic electrokinetics. Part I: Acid–base equilibria and pH buffers", Lab on a Chip, **2009**, 9 (17), 2437-2453.

[161] Christensen, J.J., L.D. Hansen, and R.M. Izatt, "Handbook of proton ionization heats and related thermodynamic quantities". **1976**: Wiley New York.

[162] Wright, M.R., "An introduction to aqueous electrolyte solutions". **2007**: Wiley.

[163] Lewis, G.N., Randall, M., Pitzer, K. S., Brewer, L., "Thermodynamics". 2 ed. **1961**, New York: McGraw-Hill.

[164] Grenthe, I. and A. Plyasunov, "On the use of semiempirical electrolyte theories for the modeling of solution chemical data"*,* Pure and applied chemistry, **1997**, 69 (5), 951-958.

[165] Olofsson, G. and L. Hepler, "Thermodynamics of ionization of water over wide ranges of temperature and pressure"*,* Journal of Solution Chemistry, **1975**, 4 (2), 127-143.

[166] Hirokawa, T., M. Nishino, and Y. Kiso, "Isotachophoretic determination of mobility and pKa by means of computer simulation: II. Evaluation of mo and pKa of 65 anions"*,* Journal of Chromatography A, **1982**, 252, 49-65.

[167] Michov, B.M., "Specifying the equilibrium constants in Tris-borate buffers"*,* ELECTROPHORESIS, **1986**, 7 (3), 150-151.

[168] Shapiro, H.M. and N.G. Perlmutter, "Killer applications: Toward affordable rapid cell-based diagnostics for malaria and tuberculosis"*,* Cytometry Part B: Clinical Cytometry, **2008**, 74 (S1), S152-S164.

[169] Tárnok, A. and A.O. Gerstner, "Clinical applications of laser scanning cytometry"*,* Cytometry, **2002**, 50 (3), 133-143.

[170] Wilson, R., A.R. Cossins, and D.G. Spiller, "Encoded Microcarriers For High-Throughput Multiplexed Detection"*, Angewandte Chemie International Edition,* **2006**, 45 (37), 6104-6117.

[171] Ortiz, M.E. and D. Endy, "Engineered cell-cell communication via DNA messaging"*, Journal of biological engineering,* **2012**, 6 (1), 1-12.

[172] Leslie, D.C., et al., "New Detection Modality for Label-Free Quantification of DNA in Biological Samples via Superparamagnetic Bead Aggregation"*, Journal of the American Chemical Society,* **2012**, 134 (12), 5689-5696.

[173] De Rosa, S.C., J.M. Brenchley, and M. Roederer, "Beyond six colors: a new era in flow cytometry"*, Nature medicine,* **2003**, 9 (1), 112-117.

[174] Lenz, D., et al., "Six and more color immunophenotyping on the slide by laser scanning cytometry (LSC)", in *Biomedical Optics 2003*, **2003**, International Society for Optics and Photonics.

[175] Shapiro, H.M., "Practical flow cytometry". **2005**: Wiley. com.

[176] Kamentsky, L.A. and L.D. Kamentsky, "Microscope-based multiparameter laser scanning cytometer yielding data comparable to flow cytometry data"*, Cytometry,* **1991**, 12 (5), 381-387.

[177] Perfetto, S.P., P.K. Chattopadhyay, and M. Roederer, "Seventeen-colour flow cytometry: unravelling the immune system"*, Nature Reviews Immunology,* **2004**, 4 (8), 648-655.

[178] Quirke, P. and J. Dyson, "Flow cytometry: methodology and applications in pathology", The Journal of pathology, **1986**, 149 (2), 79-87.

[179] Brown, M. and C. Wittwer, "Flow cytometry: principles and clinical applications in hematology", Clinical chemistry, **2000**, 46 (8), 1221-1229.

[180] Darzynkiewicz, Z., et al., "Laser-scanning cytometry: a new instrumentation with many applications", Experimental cell research, **1999**, 249 (1), 1-12.

[181] Mandy, F., et al., "Affordable CD4 T-cell enumeration for resource-limited regions: A status report for 2008", Cytometry Part B: Clinical Cytometry, **2008**, 74 (S1), S27-S39.

[182] Kinosita, K., et al., "Dual-view microscopy with a single camera: real-time imaging of molecular orientations and calcium", The Journal of Cell Biology, **1991**, 115 (1), 67-73.

[183] Chandrasekhar, S., "Stochastic problems in physics and astronomy", Reviews of modern physics, **1943**, 15 (1), 1.

[184] Einstein, A., "On the movement of small particles suspended in stationary liquids required by the molecular-kinetic theory of heat", Annalen der Physik, **1905**, 17 (549-560), 16.

[185] Meinhart, C., S. Wereley, and J. Santiago, "PIV measurements of a microchannel flow", Experiments in Fluids, **1999**, 27 (5), 414-419.

[186] Santiago, J.G., et al., "A particle image velocimetry system for microfluidics"*, Experiments in Fluids, **1998**, 25 (4), 316-319.

[187] Meinhart, C.D., S.T. Wereley, and J.G. Santiago, "PIV measurements of a microchannel flow"*, Experiments in Fluids, **1999**, 27 (5), 414-419.

[188] Wereley, S.T. and C.D. Meinhart, "Recent Advances in Micro-Particle Image Velocimetry"*, Annual Review of Fluid Mechanics, **2010**, 42 (1), 557-576.

[189] Adrian, R.J. and J. Westerweel, "Particle image velocimetry". Vol. 30. **2010**: Cambridge University Press.

[190] Raffel, M., et al., "Particle Image Velocimetry–A Pratical Guide". 2 ed. Particle image velocimetry: a pratical guide. **2007**, Heidelberg: Springer Press.

[191] Meinhart, C.D., S.T. Wereley, and J.G. Santiago, "A PIV algorithm for estimating time-averaged velocity fields"*, Journal of Fluids Engineering, **2000**, 122 (2), 285-289.

[192] Takehara, K. and G.T. Etoh, "A study on particle identification in PTV particle mask correlation method"*, Journal of Visualization, **1999**, 1 (3), 313-323.

[193] Takehara, K., R. Adrian, and T. Etoh, "A new Super-Resolution method by using the KC method"*, Journal of the Visualization Society of Japan, **1999**, 19 (Suppl 1), 319-322.

[194] Takehara, K., et al., "A Kalman tracker for super-resolution PIV"*, Experiments in Fluids, **2000**, 29 (1), S034-S041.

[195] Devasenathipathy, S., J.G. Santiago, and K. Takehara, "Particle Tracking Techniques for Electrokinetic Microchannel Flows"*, Analytical Chemistry*, **2002**, 74 (15), 3704-3713.

[196] Devasenathipathy, S., et al., "Particle imaging techniques for microfabricated fluidic systems"*, Experiments in Fluids*, **2003**, 34 (4), 504-514.

7 Appendix A. ITP compatible lysis methods

Contents of this Appendix are under preparation for publication by Anita Rogacs, Lewis A. Marshall, and Juan G. Santiago in the Journal of Chromatography A. They are reproduced here with modifications.

KEY CONSIDERATIONS

Lysis protocols for DNA and RNA extractions should effectively disrupt cells or tissues, denature proteins and nucleoprotein complexes, and inactivate endogenous nucleases (e.g: DNase and RNase). For organisms that have cell walls in addition to a cell membrane, the use of additional enzymes may be required for complete cell disruption. For example, the cell membrane of gram-positive bacteria consists of many layers or peptidoglycan (polymer consisting of sugars and amino acids), which are notoriously difficult to lyse. The addition of lysozyme has been shown to disrupt the bacterial cell walls very effectively.[1] Similarly, the cell walls of yeast contain chitin and other polysaccharides[2] and require enzymatic digestion using zymolase or lyticase.[3]

Lysis methods compatible with ITP can be categorized into three major groups: thermal, electrical, and chemical (including enzymatic) lysis. The thermal and electrical approaches are often attractive, as they do not introduce PCR inhibiting species which can co-focus with nucleic acids during ITP, nor do they alter ITP dynamics by changing the solution pH or conductivity. However, chemical approaches are very convenient as they can often be performed at room temperature with only addition of chemicals to the sample (requiring no special equipment). We here focus mostly on off-chip lysing

methods performed prior to loading samples into the chip, but mention several on-chip lysing methods.

DETERGENTS

Most mammalian and cultured cells lyse in presence of detergents. Ionic detergents such as sodium dodecyl sulfate (SDS) can also denature proteins by binding to charged side chains and causing local changes in protein conformation. ITP can be made compatible with the anionic SDS (unpublished results), but the use of SDS is often restrictive as it sets a minimum value on the trailing ion effective mobility (SDS has a mobility of about 23 cm2/V/s)[4]. To keep denatured proteins in solution, and prevent their aggregation, we recommend the addition of mild non-ionic detergents such Triton X-100 or Tween 20 to the lysis buffer (usually added at roughly the critical micelle concentration). Non-ionic detergents are well compatible with ITP as they do not migrate under electric field. Also, non-ionic surfactants are compatible with many downstream assays including PCR (e.g.: Triton X-100 is a PCR adjunct below 10% w/v, which is ~103 times the CMC concentration).[5]

DENATURANTS

The denaturing step disrupts nucleoprotein complexes (e.g., disrupts chromatin and releases chromosomal DNA from histone) by unfolding proteins. Examples of chaotropic denaturing reagents include sodium tricholoroacetate, sodium perchlorate, sodium thiocynate, urea, guanadinum thiocynate and guanadinium hydrochloride.[6] Chaotropic-based protein denaturation requires the presence of these reagent at high concentrations (6 M-10 M).[7] These species strongly inhibit PCR, and with the exception

144

of urea, they contain fast anions that can co-focus with NA and even form a plateau zone between LE and TE. The high concentrations of these ions in the lysate require prohibitively long purification times for ITP-based extraction of NA (up to 10 h, unpublished results). Also important, anionic chaotrope species can co-purify with the NA. For applications which have strict requirements of chaotropic-based denaturation, we recommend the use of urea. Urea is a non-ionic reagent, so it does not interfere with ITP dynamics and stays behind (in the initial TE zone) during the purification process. Our group has demonstrated urea compatibility with ITP at high concentrations.[8]

NUCLEASE INACTIVATION

Nuclease inactivation: Effective inactivation of endogenous nucleases (DNase and RNase enzymes) is a key early step in the extraction process. DNases can usually be inactivated by use chelating agents (e.g., ethylenediamine-tetraacetic acid, EDTA),[9] which sequester magnesium ions that are essential for nuclease function. EDTA is a fast, tetravalent anionic species, and as a result, in many ITP separation chemistries, EDTA will overspeed DNA and RNA and the leading electrolyte (chloride). EDTA also inhibits PCR at concentrations above 0.1 mM.[5] One approach to purifying nucleic acid from EDTA may be to initiate ITP into a waste well, and subsequently switch the ITP anode into a separate extraction well. An alternative to EDTA for DNAse activation is to increase temperature (>65 °C) or perform proteinase K digestion at 56 °C. Proteinase K is a PCR inhibitor, but can be excluded easily by working with pH below about 8.5.[10]

Inactivation of ribonuclease (Rnase) is more challenging due to its highly resilient nature and fast catalytic action on RNA. As one salient example, without adequate RNase

control, free RNA is non-amplifiable after 15 s of incubation in plasma or serum.[11] Neither EDTA nor heat will inactivate RNase permanently.[12,13] Other RNase inhibiting agents are therefore required in RNA extraction protocols. RNase inhibitors include ribonucleoside-vanadyl complex[14] and RNasin,[15] as well as other commercially available proprietary reagents (e.g., RNAsecure sold by Ambion, or RNase Out sold by Invitrogen). The ribonucleoside- vanadyl complex will also inhibit downstream reactions such as in vitro translation and reverse transcription, so we do not recommended it.

Addition of reducing agents such as dithiothreitol (DTT) (pKa = 8.3 and 9.5) or 2 beta- mercaptoethanol (2B-ME) (pKa = 9.64) can enhance denaturation of disulfide bond containing proteins and thereby also aid in ribonuclease inactivation.[16] (Rnase activity requires intact disulfide bonds.) However, because they are anions in their active state, they can each co-focus with the NA during ITP. This co-focusing can be avoided by choosing a suitably high mobility trailing ion, or by diluting the extracted RNA suspension to contain no more than 10 mM DTT. Below this concentration, DTT is a PCR adjunct. See detailed discussion on DTT-based RNase inactivation method in Chapter 2.

Chomazinsky and Sacchi,[17] showed that RNA solubilized in pure formamide resist Rnase induced degradation. In practice, formamide is often added to aqueous hybridization buffers to modify the melting temperature of RNA or DNA duplexes. One may also be tempted to add formamide to lysing buffers to inactivate the Rnase enzymes. However, we emphasize here that the RNase inhibition is only effective if solubilization occurs in pure, deionized formamide. In fact, formamide should never be used as an additive in an aqueous lysing or hybridization reaction when Rnase is believed to be

146

present. Our own observations suggest that, when mixed with water, formamide promotes RNA degradation even at extremely high RNA concentrations (see **Fig. A.1**) Others have also reported enhanced Rnase activity in the presence of aqueous formamide.[18]

To study the effect of RNA degradation, we recommend performing size-based separation of RNA. Agilent's 2100 Bioanalyzer uses a lab on a chip approach to perform capillary electrophoresis of fluorescently labeled RNA to determine both RNA concentration and integrity. The on-chip RNA analysis is based on traditional gel electrophoresis principles that enable RNA separation based on size. The RNA electropherograms provides a detailed visual assessment of the quality of the RNA sample. As degradation proceeds (**Fig. A.1**), there is a decrease in the 18S to 28S ribosomal band ratio and an increase in the baseline signal between the two ribosomal peaks and the lower marker.

The RNA Integrity Number (RIN), was developed by Agilent to remove individual interpretation in RNA quality control and allow classification of RNA integrity. Their software computes the RIN by accounting for the entire electrophoretic trace,[19] and assigns a RIN based on a numbering system from 1 to 10, with 1 being the most degraded profile and 10 being the most intact. In **Fig. A.1**. we show various levels of RNA degradation induced by blood and aqueous formamide.
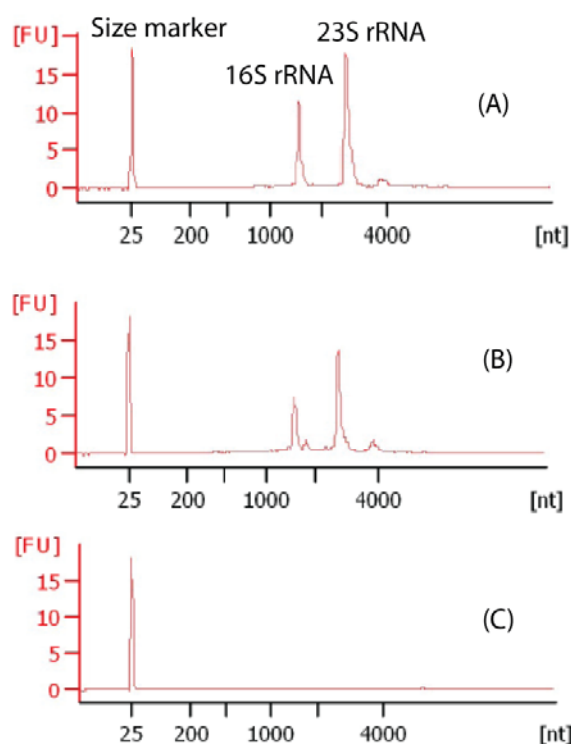
Figure A.1. Effect of formamide on RNA integrity evaluated on Agilent's 2100 Bioanalyzer. We used a commercial SPE-based RNA extraction kit to lyse and purify the RNA content from E.coli cells. We incubated the RNA content from approximately ~107 cells in (A) RNase, DNase free water (Control), (B) water mixed with 20% whole blood (C) and water mixed with 20% whole blood and 57.5% formamide for 2 min. The solution containing RNA suspended in water alone has high integrity (RIN = 10). The RNA incubated in blood for 2 min shows some sign of degradation (RIN = 8.8). The addition of formamide enhances the degradation process. In 2 min, no RNA is detected in solution (RIN = 0.0).

We note here that many detection methods are insensitive to moderate RNA degradation. Successful PCR amplification, for example, does not require the presence of full length, intact sequences of DNA or RNA. Even if the Bioanalyzer shows a significantly altered RNA size distribution, PCR amplification may be unaffected. RNA degradation is a process which involves gradual chopping of RNA sequences into shorter ones. Hence, if

148

> 50% of the sequence region bounded by the PCR probes remains intact during RNA sample preparation, the amplification may remain unaffected by the degradation. Note, that these regions are typically fairly short (~100 nt). In the study presented in Chapter 2, we analyzed RNA integrity using Bioanalyzer, but we have also performed RT-PCR to determine the upper tolerance for RNA degradation. In the study of Chapter 2, RNA degradation which produced less than one cycle increase in the amplification threshold cycle was deemed acceptable.

REFERENCES

[1]   Liao, J.C., et al., "Use of electrochemical DNA biosensors for rapid molecular identification of uropathogens in clinical urine specimens", Journal of Clinical Microbiology, 2006, 44 (2), 561-570.

[2]   Hudler, G.W., "Magical mushrooms, mischievous molds". 1998: Princeton University Press.

[3]   Salazar, O. and J. Asenjo, "Enzymatic lysis of microbial cells", Biotechnology Letters, 2007, 29 (7), 985-994.

[4]   Carchon, H. and E. Eggermont, "Isotachophoretic determination of a relative apparent mobility as an estimate of the electrophoretic mobility of ions", Electrophoresis, 1982, 3 (5), 263-274.

[5]   Kreader, C.A., "Relief of amplification inhibition in PCR with bovine serum albumin or T4 gene 32 protein", Applied and Environmental Microbiology, 1996, 62 (3), 1102-1106.

[6]   Hatefi, Y. and W.G. Hanstein, "Solubilization of Particulate Proteins and Nonelectrolytes by Chaotropic Agents", Proceedings of the National Academy of Sciences of the United States of America, 1969, 62 (4), 1129-1136.

[7]   Greene, R.F. and C.N. Pace, "Urea and guanidine hydrochloride denaturation of ribonuclease, lysozyme, α-chymotrypsin, and β-lactoglobulin", Journal of Biological Chemistry, 1974, 249 (17), 5388-5393.

[8]   Persat, A., et al., "Quantification of Global MicroRNA Abundance by Selective Isotachophoresis", Analytical Chemistry, 2010, 82 (23), 9631-9635.

[9]   Adams, R.L.P., J.T. Knowler, and D.P. Leader, "The biochemistry of the nucleic acids". 1992: Chapman and Hall.

[10]   Persat, A., L.A. Marshall, and J.G. Santiago, "Purification of Nucleic Acids from Whole Blood Using Isotachophoresis", Analytical Chemistry, 2009, 81 (22), 9507-9511.

[11]   Tsui, N.B.Y., E.K.O. Ng, and Y.M.D. Lo, "Stability of Endogenous and Added RNA in Blood Specimens, Serum, and Plasma", Clinical Chemistry, 2002, 48 (10), 1647-1653.

[12]   Farrell, R.E., "RNA methodologies: A laboratory guide for isolation and characterization". 4 ed. 2010, San Diego, CA: Academic Press, Inc.

[13]   Steward, G.F. and A.I. Culley, "Extraction and purification of nucleic acids from viruses", Manual of Aquatic Viral Ecology, 2010, 154-165.

[14]   Berger, S.L. and C.S. Birkenmeier, "Inhibition of intractable, nucleases with ribonucleoside-vanadyl complexes: isolation of messenger ribonucleic acid from resting lymphocytes", Biochemistry, 1979, 18 (23), 5143-5149.

[15]   Blackburn, P., G. Wilson, and S. Moore, "Ribonuclease inhibitor from human placenta. Purification and properties", Journal of Biological Chemistry, 1977, 252 (16), 5904-5910.

[16]   Lu, B.-Y. and J.-Y. Chang, "Rapid and irreversible reduction of protein disulfide bonds", Analytical Biochemistry, 2010, 405 (1), 67-72.

[17]   Chomczynski, P., "Solubilization in formamide protects RNA from degradation", Nucleic Acids Research, 1992, 20 (14), 3791-3792.

[18]   Strauss Jr, J.H. and R.L. Sinsheimer, "Initial kinetics of degradation of MS2 ribonucleic acid by ribonuclease, heat and alkali and the presence of configurational restraints in this ribonucleic acid", Journal of Molecular Biology, 1968, 34 (3), 453-465.

[19]   Mueller, O., S. Lightfoot, and A. Schroeder, "RNA integrity number (RIN)– Standardization of RNA Quality Control", Agilent Application Note, Publication, 2004, 1-8.

8 Appendix B. Particle hybrid analysis

DEGREE OF AGGREGATION

The particle identification and collocation performed by the standard configuration of the PITC algorithm relies on the similarity between particle image patterns only (and is insensitive to the absolute value of particle image intensity). Particle imaging conditions can therefore greatly influence the complexity of particle hybrids detected by the algorithm.

Consider, for example, the case where a particle geometrically projected onto the image plane is smaller than the size of a single pixel. In this case, the geometric projection of an aggregate containing two or more particles of the same color may also span less than a pixel, and its brightness pattern will look identical to that of a single particle image. In this case also, the magnitude of the intensity profile provides the only means to differentiate between their identities.

The PITC algorithm characterizes the fluorescence intensity of each identified particles (or particle hybrids) using Gaussian fitting to the particle images. This particle intensity information can be visualized using a cytometry-like scatter plot (see for example **Fig. B.1**). This intensity particle profile can presumably provide useful information on the number of same color particles participating in a particle aggregate (e.g.: triplets containing two red and one green, or hybrids containing two reds and two greens, etc).

As an example we here show the intensity profile of a bead suspension containing large numbers of same color singlets, doublets and triplets. We prepared the particle

suspension by simply diluting the fluorescent bead stock solution. Since the concentration of beads in the stock solution is high ($\sim 10^{10}$ #/mL), there are many non-specifically bound bead hybrids in the solution. Brief sonication of the diluted beads is always recommended, a process which effectively breaks up these non-specific bonds. To obtain the intensity image profile shown in **Fig. B.1**, we did not sonicate the bead suspension. Visual inspection of the particle intensity distribution shape revealed strong evidence of doublets, triplets and more complex aggregates. We analyzed the images of the bead suspension with PITC and plot the intensity profile for all the beads identified. For this demonstration, we disabled the intensity-based filter in the PMC-PC algorithm phase. As a result, the PITC detected all abundant particle hybrid structures; the three intensity peaks corresponding to singlets, doublets, and triplets.
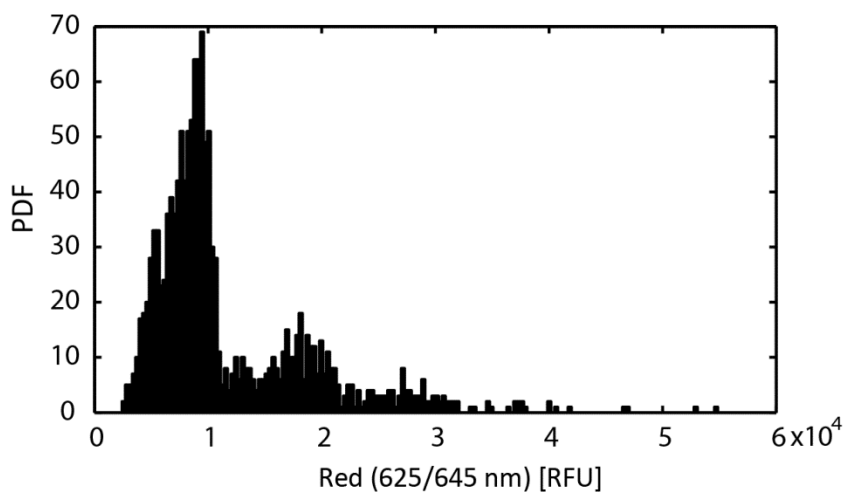

Figure B.1. Fluorescence intensity profile of unsonicated red particles in free solution. The intensity-based thresholds in the PMC-PC phase of PITC were deactivated. The first three peaks correspond to red singlets, doublets and triplets in solution.

We have also implemented intensity-based threshold filters in both phases (PMC-PC and collocation) of the algorithm, thus a user can chose to eliminate undesired same-

color particle hybrids during the PITC analysis. See **Section. 4.2.4** for details on the implementation and recommended settings. Automating the intensity-based particle filtering during the PITC analysis is appropriate for applications where the relevant physical phenomena are revealed only in a subset of particle hybrids (e.g., monitoring communication between two cells requires information for two-color cell doublets only).

BINDING INDUCED SPECTRAL LEAKAGE

To eliminate biases associated with particle intensity variations, intensity-based filters should always be calibrated using measurements performed on the particle image set being analyzed. One source of variation is associated with changes in the illumination power, which can cause statistically significant shift in particle intensities measured between experiments. Another source of variation is associated with spectral leakage of dual-color particle hybrids. For example, in **Figure B.2** we show the PDF of green and red particles unbound (black) and bound via DNA hybridization (green). See **Figure 4.10** for scatter plot of particle (bead) intensities for this experiment.
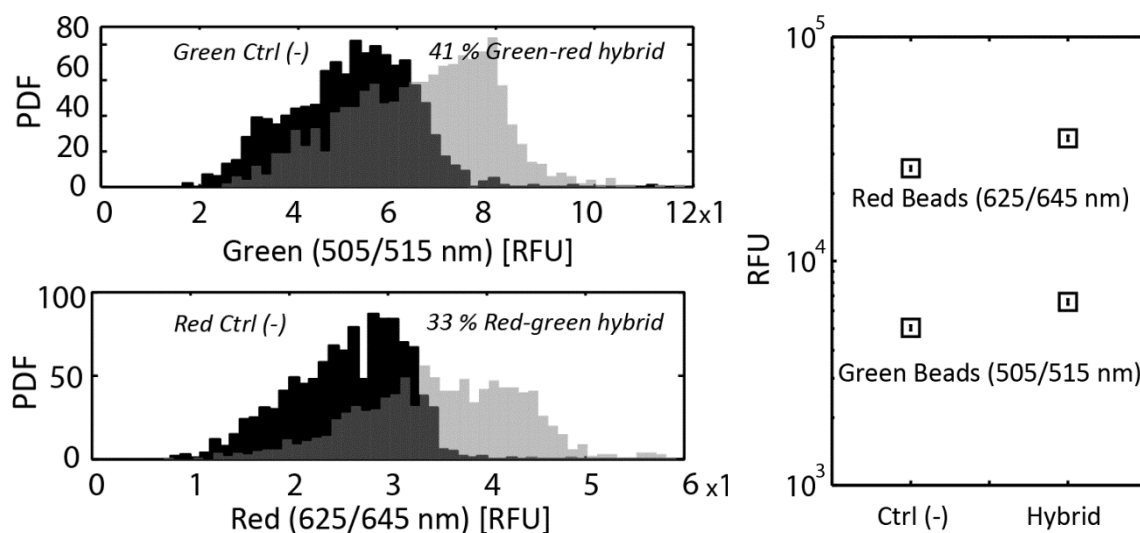
Figure B.2. Binding induced shift in bead fluorescence intensity. Left: Green and red fluorescence intensity for single beads (black) and bead-bead hybrids (gray). Right: The mean of green and red bead intensities for unbound, (Ctrl (-)), and bound (Hybrids) samples. The error bars (indicated inside the markers) represent 99.9% certainty in the mean of bead intensities.

Across several realizations, we saw consistent increase in the emission intensities of the tracked beads (e.g., green) when they were bound to another bead of a different peak fluorescence spectra (e.g, red). Since the fluorescence emission of a dye can occur far from the peak emission wavelength, we hypothesize that the observed increase of emission intensity of each dye in a two-color bead hybrid is associated with the leakage of the off-peak fluorescence emission of the other bead in the hybrid. We hypothesize also that this effect can be decreased by careful selection of color filters.